Process Design and Feasibility Study of Synthetic Crude Production by the Combination of Methane Decomposition, Reverse Water Gas Shift Reaction, and Fischer-Tropsch Synthesis

By

Somaiyeh Mahouri

A Thesis Submitted to

The Faculty of Graduate Studies

of Lakehead University of Thunder Bay

in Partial Fulfillment of the requirements

for the Degree of

Master of Science in Chemical Engineering

Lakehead University

Thunder Bay

Abstract

In this dissertation, the conversion of CO_2 to gas-to liquid (GTL) products was investigated for the production of 30000 bbl per day syncrude. The GTL plant consisted of four main units: hydrogen production by catalytic thermal decomposition of methane in a Cu-Bi molten media, syngas production by the reverse water gas shift (RWGS) reaction using a nickel-based catalyst, syncrude production by the low temperature Fischer-Tropsch (LTFT) synthesis over a cobalt-based catalyst, and an energy recovery unit for electricity generation. The plant was simulated by the coupling of HYSYS and MATLAB to simulate the RWGS and FT reactors and converge their recycle streams. 150 alkanes and 149 alkenes were included in the simulation to accurately estimate the product distribution of the FT reactor. The fixed capital investment of the plant and the manufacturing cost of syncrude were \$1.6 billion and \$137 bbl^{-1}, respectively. It was found that hydrogen production by methane decomposition reduced the manufacturing cost of syncrude by 32% when compared to GTL plants that sourced their hydrogen from water electrolysis. The profitability analysis showed the plant could not be economically viable without selling the produced solid carbon. The breakeven price of the produced solid carbon was estimated to be \$633 $tonne^{-1}$ for a syncrude selling price of \$59.31 bbl^{-1}. The economic performance of the plant was highly favourable at syncrude selling prices higher than \$80 bbl^{-1}. It was determined that the plant was a net emitter of CO_2 at a rate of 19.92 g CO_2 per 1 MJ of syncrude, which was lower than the reported values for different types of natural-gas based GTL plants, but higher than water electrolysis-FT plants.

Acknowledgment

Foremost, I would like to express my deep appreciation to my supervisor Dr. Ebrahim Rezaei. Without his endless support and participation, I would not have been able to complete the thesis. His patience, guidance, and immense knowledge paved the way for me in every stage of this research; even my most profound gratitude is not enough.

Besides my supervisor, I would you like to thank my advisory committee members, Dr. Lionel Catalan and Dr. Ehsan Azar, for providing me with their valuable feedback to complete my thesis. I am also grateful to the graduate coordinator of the Chemical Engineering Department, Dr. Leila Pakzad, for her support and guidance.

I sincerely thank Lakehead University's Faculty of Engineering and Faculty of Graduate Studies for giving me the opportunity to make my dreams become true.

Last but not the least; I would like to thank my mother, Laya, for her prays and love. I am forever indebted to Mariann Frigeri for her endless supports and encouragement. Above all, I would like to give my special thanks to my fiancé for his understanding and continuous support to overcome the difficulties that I faced.

Table of Contents

List of Figures

List of Tables

Nomenclature

A	Surface area of the catalyst ($m^2\ Kg^{-1}$) or tube-cross section area (m^2)
a	Interfacial surface area per unit volume ($m^2\ m^{-3}$)
C	Concentration of species (mol m^{-3})
COM_d	Cost of manufacturing without deprecation ($\$\ yr^{-1}$)
C_{Cat}	Cost of catalyst replacement ($\$\ yr^{-1}$)
C_{GR}	Grassroots cost ($)
C_{RM}	Cost of raw material ($\$\ yr^{-1}$)
C_{UT}	Cost of utility ($\$\ yr^{-1}$)
C_{WT}	Cost of water treatment ($\$\ yr^{-1}$)
C_P	Heat capacity (J $mol^{-1}\ K^{-1}$) or (J $kg^{-1}\ K^{-1}$)
d	Reactor inner diameter (m)
D	Diffusion coefficient ($m^2\ s^{-1}$)
D_{ij}	Effective diffusivity of gas species ($m^2\ s^{-1}$)
DPBP	Discounted payback period (year)
ΔH	Activation energy of FTS (kJ mol^{-1}) or enthalpy change of the steam in the turbine (kJ kg^{-1})
ΔH_r	Heat of the reaction of FTS (kJ mol^{-1})
$\Delta H_{R,n}$	Heat of the reaction of the RWGS reaction (J mol^{-1})
E_a	Activation energy (J mol^{-1})
F	Molar flow rate (mol s^{-1})
FCI	Fixed capital cost ($)
F_{SC}	Correction factor (unitless)

F_{TC}	Tube count constant (unitless)
g	Gravitational acceleration (9.81 m s^{-1})
h	Heat transfer coefficient (W m^{-2} K^{-1})
H	Henry's constant (Pa m^3 mol^{-1})
$h_{wall,o}$	Stagnant heat transfer (W m^{-2} K^{-1})
$h_{wall,g}$	Convective heat transfer (W m^{-2} K^{-1})
IRR	Internal rate of return (unitless)
k	Reaction rate constant (unit dependent on the form of rate law)
K	Equilibrium constant (unit dependent on the frequency factor)
k_o or K_o	Pre-exponential factor (unit dependent on reaction law)
K_C	Equilibrium constant of the RWGS reaction or MDR (unitless)
L	Reactor length (m)
m	Mass flowrate of the steam (kg s^{-1})
M_i	Molecular weight of species (g mol^{-1})
M_n	Molar fraction of produced hydrocarbons (unitless)
$\dot{n}_i$	Molar flow rate of species (mol s^{-1})
N_{OL}	Total number of operators (unitless)
NPW	Net present worth ($)
P	Pressure (Pa, atm, MPa, bar)
P_C	Pitch configuration factor (unitless)
P_T	Tube pitch (m)
R	Universal gas constant (8.314 J mol^{-1} K^{-1}) or radius of the reactor tube (m)
r	Reaction rate (unit dependent on the reaction law)

S_g	BET surface area of the porous particles ($cm^2\ g^{-1}$)
T	Temperature (K)
TCI	Total capital investment ($)
u	Iinterstitial gas velocity ($m\ s^{-1}$)
U	Overall heat transfer coefficient ($W\ m^{-2}\ K^{-1}$)
US	Usage ratio (dimentionless)
V_b	Wax molar volume ($cm^3\ mol^{-1}$)
V_0	Wax close-packed hard sphere volume ($cm^3\ mol^{-1}$)
V°	Volumetric flowrate ($m^3\ s^{-1}$)
WC	Working capital ($)
W_n	Mass fraction of produced hydrocarbons (unitless)
W_s	Shaft power (kW)
x	Efficiency of steam turbine (unitless)
X	Conversion (dimensionless)
y	Molar fraction (unitless)

Greek letters

α	Gas holdup in MDR or Chain growth probability in FTS (dimensionless)
β	External mass transfer coefficient ($m\ s^{-1}$)
ε	Mole fraction of CH_4 in the feed or porosity (dimensionless)
η	Effectiveness factor or efficiency of the steam turbine (unitless)
λ	Thermal conductivity ($W\ m^{-1}\ K^{-1}$)
μ	Dynamic viscosity ($kg\ m^{-1}\ s^{-1}$)
ν	Superficial velocity ($m\ s^{-1}$)

ρ	Density (kg m^{-3})
σ	Molecular diameter (A^o)
τ	Tortuosity (unitless)
υ	Kinematic viscosity (m^2 s^{-1})
φ	Thiele modules (unitless)

Subscripts

Avg	Average
b	Bulk or bed
c	Catalytic
CS	Cross section
dr	Drive
eff	Effective
er	Effective radial
eq	Equilibrium
ext	External
g	Gas
i	Species
in	Inner
IS	Isentropic
knu	Knudsen
l	Liquid
max	Maximum
mol	Molecular

nc	Non-catalytic
p	Catalyst particles
s	Surface of catalyst particles
t	Tube

Superscript

prod	Product
s	Static

Abbreviations

ASF	Anderson-Schulz-Flory
BFD	Block flow diagram
CCS	Carbon capture and sequestration
CCU	Carbon capture and utilization
CW	Cooling water
DMR	Dry methane reforming
EDR	Exchanger design and rating
FT	Fischer-Tropsch
FTS	Fischer-Tropsch synthesis
GHG	Greenhouse gas
GTL	Gas-to-liquid
HTFT	High temperature Fischer-Tropsch
LCA	Life cycle analysis
LMBR	Liquid metal bubble reactor

LTFT	Low temperature Fischer-Tropsch
MDR	Methane decomposition
MEA	Monoethanolamine
PFD	Process flow diagram
PSA	Pressure swing adsorption
P2G	Power to gas
P2L	Power to liquid
ROI	Return on investment
RWGS	Reverse water gas shift
SEOC	Solid oxide electrolysis cell
SMR	Steam methane reforming
WGS	Water gas shift

Chapter 1: Introduction

1.1 Research background and motivation

Climate change has become a global concern in recent years due to the accumulation of greenhouse gases (GHGs) in the atmosphere and their deleterious environmental and health effects [1]. Anthropogenic GHGs such as CO_2, CH_4, N_2O, and fluorinated gases trap heat between the Earth's atmosphere and surface, which results in rising sea levels, unusual weather patterns, and wild fires with catastrophic effects on the plant ecosystems [2,3].

The reduction of GHG emissions to the atmosphere can slow down the rate of climate change, which in turn paves the way for an industrial revolution towards the incorporation of renewable energies and chemicals. Carbon capture and sequestration/utilization (CCS and CCU) are promising approaches to mitigate the negative effects of GHG emissions. Several approaches such as biological, physiochemical, and geological methods have been proposed in recent years to capture, store, and re-use CO_2. The principle of the CCS is based on capturing and storing CO_2 in geological formations and reservoirs. The captured CO_2 is compressed and injected to storage formations such as depleted gas, oil, and saline formations. The cost of CCS is highly affected by the place of storage site, the depth of the storage formation, the number of wells, and process monitoring [4]. On the other hand, the captured CO_2 can be used as feedstock for the production of value-added chemicals. The utilization of the captured CO_2 can reduce the greenhouse effects of CO_2-emmiting industries around the world since its aim is to convert the problematic CO_2 to renewable chemicals. A wide range of products may be manufactured from CO_2, which can be used as intermediate (synthesis gas) or final products (fuels such as dimethyl ether, gasoline, diesel, etc.) [5,6].

The reformation of CO_2 to gas-to-liquid (GTL) products is one of the CCU methods that is suggested for the conversion of CO_2 to fuels. Despite advances made in developing conceptual CO_2 to GTL plants, their economic feasibility is questionable. The economic viability of GTL plants is dependent on the price of raw materials, especially renewable hydrogen. Most of published studies only focus on renewable hydrogen production by water electrolysis and overlook other CO_2-free hydrogen production routes such as thermal decomposition of methane. In this thesis, a coupled CO_2 to GTL plant is developed based on hydrogen production by catalytic copper-bismuth thermal decomposition of methane in a liquid molten bubble reactor, reformation of CO_2 to syngas by the reverse water gas shift reaction using a Ni-based catalyst, and the conversion of syngas to synthetic crude by low temperature Fischer-Tropsch synthesis using a Co-based catalyst. The designed GTL plant is evaluated from economic and environmental perspectives.

1.2 Structure

Chapter 2 presents a literature review on CO_2 to GTL products that has been studied in recent years for direct and indirect CO_2 hydrogenation to synthetic fuels with emphasis on their design aspects as well as economic and environmental performance. Chapter 3 presents the process block flow diagram and methodologies used in this thesis. Chapter 4 explains the details of several units involved in the proposed CO_2 to GTL plant and evaluates the economic and environmental performance of the plant. Chapter 5 includes the conclusions of this thesis and recommendations for future works.

Chapter 2: Literature Review

Chapter 2 reviews simulation studies published in recent years on direct and indirect CO_2 hydrogenation to gas-to-liquid (GTL) products. A brief introduction is given on the Fischer-Tropsch synthesis (FTS) at the beginning of this chapter to provide background information on the FTS. The literature review mainly focuses on the economic and environmental feasibility of proposed processes for the reformation of CO_2 to GTL products. This chapter also presents existing knowledge gaps in the literature and objectives of this thesis.

2.1. A brief introduction on the Fischer-Tropsch synthesis

The history of the FTS dates back to the 20th century when Franz Fischer and Hans Tropsch developed a process to generate hydrocarbons from syngas (mixture of H_2 and CO) in 1925 [7]. FT reactions are highly exothermic that convert syngas to alkanes, alkenes, alcohols, and carbonyls by Eqs. (2-1) to (2-4), respectively, [8]:

$$nCO + (2n+1)H_2 \rightarrow C_nH_{2n+2} + nH_2O \quad (2\text{-}1)$$

$$nCO + (2n)H_2 \rightarrow C_nH_{2n} + nH_2O \quad (2\text{-}2)$$

$$nCO + (2n)H_2 \rightarrow C_nH_{2n+1OH} + (n\text{-}1)H_2O \quad (2\text{-}3)$$

$$nCO + (2n\text{-}1)H_2 \rightarrow C_nH_{2nO} + (n\text{-}1)H_2O \quad (2\text{-}4)$$

FT reactions can be considered as a group of polymerization reactions with initiation, chain growth, and termination as their main steps. Different mechanisms are proposed to describe the kinetics of FT reactions such as carbide, CO-insertion, and hydroxycarbene mechanisms. In the carbide mechanism, the adsorption and dissociation of CO on the surface of FT catalysts with or without hydrogen association produce CH_x species as monomers. By propagation of the produced

monomers, hydrocarbon chains grow to produce alkenes, alkanes, and alcohols. In the CO-insertion mechanism, FT reactions are initiated by hydrogenation of CO followed by the dissociation of CO. Chain propagation occurs by the formation of CH(OH)R fragments and the polymerization is terminated by hydrogenation to form final products. The CO insertion mechanism is one of the widely accepted mechanisms for the production of oxygenates, alkanes, and alkenes. Unlike the CO-insertion mechanism, the hydroxycarbene mechanism starts with the chemisorption of CO on the surface of FT catalysts. The adsorbed CO molecules are consequently hydrogenated to form intermediate hydroxycarbene species, which produce GTL products [8,9].

Transition and noble metals such as cobalt, iron, nickel, and ruthenium are commonly used as FT catalysts. The most preferable transition metals in the FTS are cobalt and iron at the temperature and pressure ranges of 200-300 ºC and 10-60 bar, respectively. Iron-based catalysts are cheap and have activity towards the water gas shift (WGS) reaction when compared with cobalt-based catalysts with no WGS activity [10]. Iron-based catalysts show more selectivity to alkenes and light hydrocarbons, while cobalt-based catalysts produce heavier alkanes in the form of wax. Even though ruthenium has the highest activity in the FTS to produce wax, it has limited applications because of its high price [10,11].

GTL production processes are categorized into low temperature (LT) and high temperature (HT) FTS. The LTFT processes are cobalt-based and operate at 220-250°C to produce wax. On the other hand, the HTFT processes are iron-based with a temperature range of 320-350°C and selectivity towards light hydrocarbons such as gasoline. The liquid hydrocarbons produced by GTL processes are known as synthetic crude or syncrude, which mainly consist of alkenes, alkanes, and oxygenates. The absence of aromatics as well as nitrogen, oxygen, and sulphur

compounds in the syncrude demands FT-specific downstream separation and upgrading units, which are different than those found in conventional crude oil refineries [12].

Typical FT reactors are multi-tubular fixed-bed, slurry bubble column, micro-channel, membrane, and fluidized-bed reactors. In a multi-tubular fixed-bed FT reactor, syngas enters the reactor from the top of a vertical tube bundle. The FTS proceeds inside the tubes, which are filled with catalyst particles. Saturated water enters the bottom of the shell-side of the reactor to remove the heat of FT reactions by producing steam. Although this type of reactor is simple and easy to handle, they have some drawbacks such as high capital costs, high pressure drops, mass transfer limitations in catalysts pores, and the formation of hot spots. A slurry bubble column FT reactor is made of a column filled up with liquid hydrocarbons with syngas introduced at the bottom of the reactor. The diameter of the catalyst particles used in the slurry FT reactors is between 10 and 200 μm, which results in lower mass transfer limitations when compared with fixed-bed reactors. The slurry FT reactors have higher heat transfer rates than fixed-bed reactors, which allows operating FT reactors under isothermal conditions. Despite their advantages, the slurry FT reactors have their own drawbacks such as catalyst attrition and deactivation as well as separation of catalyst particles from GTL products [7,13]. Micro-channel reactors consist of a high number of small channels containing catalysts interleaved with a cooling fluid such as water. It is claimed that micro-channel reactors have efficient heat removal and mass transfer rates with low capital costs and high CO conversions [7,14]. Membrane reactors can also be used for the FTS to improve the product selectivity by the distribution of H_2 and CO streams and creation of an isothermal operating condition. For this purpose, one of the reactants is injected throughout a tubular membrane, while the other is introduced to the catalyst bed located inside the membrane. Membrane reactors can also be utilized to remove the produced water to enhance the conversion

of CO and improve the lifetime of FT catalysts [7,15]. In a fluidized-bed reactor, a gas or liquid passes through catalysts with a speed that is high enough to suspend or fluidize the catalyst particles. Fluidized-bed rectors are mostly suitable for exothermic reactions since the local temperature gradients or hot spots can be avoided by fluidization. Moreover, the fluidization can improve the conversion of reactants by suppressing the formation of redial and axial concentration gradients. This type of reactor has its own drawbacks such as expensive maintenance cost due to the erosion of the reactor interior, separation of entrained catalyst particles, large vessel size to provide enough space for fluidization (high capital cost), and high pressure drop [16]. Among the abovementioned reactors, the membrane reactor is in a development stage with a high potential for future applications in small or medium production capacity plants [7].

The product distribution of the FTS can be described by the Anderson-Schulz-Flory (ASF) model. The ASF model is based on chain growth probability (α), which is the ratio of propagation and termination rates in FT polymerization reactions. α takes value between 0 and 1 with higher α values associated with selectivity towards heavier hydrocarbons (C_{5+}) [17]. The mole (M_n) and mass (W_n) fractions of produced hydrocarbons can be determined as a function of chain growth probability and the number of carbon atoms (n) using Eqs. (2-5) and (2-6), respectively:

$$M_n = \alpha^{n-1}(1-\alpha) \tag{2-5}$$

$$W_n = \alpha^{n-1}(1-\alpha)^2 n \tag{2-6}$$

The chain growth probability can be determined by Eq. (2-7) [18]:

$$\alpha = \left(0.2332 \times \frac{y_{CO}}{y_{CO}+y_{H2}} + 0.6330\right)\left(1 - 0.0039(T-533)\right) \tag{2-7}$$

y_{CO} and y_{H2} are the mole fractions of CO and H_2 in syngas and T is the reactor temperature in K.

The ASF model overestimates methane formation and underestimates the formation of ethylene. It also overestimates the heavy hydrocarbon formations, since α increases with increasing the number of carbon atoms [10,19]. These deviations reduce the accuracy of the ASF model to predict the distribution of GTL products. More detailed kinetic models have been proposed in recent years to improve the accuracy of the AFS model by direct insertion of α in FT reaction rates. Unlike the ASF approach, the detailed kinetic models can distinguish between alkanes and alkenes with the same number of carbon atoms. Moreover, α is not a constant value throughout FT reactors in the kinetic models, which reduces deviations from experimental results [20,21].

The first commercial FT plant was installed in 1935 in Oberhausen, Germany with nine Co-based FT plants producing 600 kt of GTL products per year from coal [7]. There are currently several operational FT plants around the world. Examples are Carthage Hydrocol in the USA with HTFT fluidized-bed reactors (305-345 °C and 2.8-4.5 MPa, with the plant capacity of 5900 bbl day^{-1} of gasoline and 1100 bbl/day of diesel), Sasol 1 in South Africa including ARGE LTFT process (200-230 °C and 2.5-2.7 MPa with the plant capacity of 2750 bbl day^{-1}) and Kellogg HTFT process (290-340 °C and 1.9 MPa with the plant capacity of 2000 bbl day^{-1}), Sasol 2 and 3 in South Africa with HTFT fluidized-bed reactors (330-360 °C and 2.5 MPa with the plant capacity of 120000 bbl day^{-1}), Mossgas HTFT fluidized-bed reactors (330-360 °C and 2.5 MPa with the plant capacity of 33000 bbl day^{-1}) in South Africa, Oryx-GTL in Qatar with two slurry LTFT reactors (230°C and 2.5MPa with the plant capacity of 34000 bbl day^{-1}), Binutlu plant in Malaysia (200-230°C and 30 bar with the capacity of 14700 bbl day^{-1}), and Pearl in Qatar (LTFT fixed-bed reactors with the plant capacity of 140000 bbl day^{-1}) [12,22–24].

2.2. Reformation of CO_2 to gas to liquid products

CO_2 is an inert and stable molecule, which requires external energy to be activated. The reaction of CO_2 with hydrogen is one of the methods suggested for the reformation of CO_2 to value-added chemicals. CO_2 can be hydrogenated to GTL products through indirect and direct chemical routes. The indirect route includes syngas production followed by the FTS, whereas the direct route converts CO_2 to GTL products in one pot without the need for syngas production units. The following sections review reported processes in the literature for direct and indirect CO_2 hydrogenation to GTL products with an emphasis on the economic and environmental performances of such plants.

2.2.1. Indirect CO_2 hydrogenation

The required syngas in the indirect route can be obtained through the dry methane reforming (DMR), reverse water gas shift (RWGS), bi-reforming of methane, and tri-reforming of methane reactions, which are given by Eqs. (2-8) to (2-13):

DMR: $CH_4 + CO_2 \rightleftharpoons 2CO + 2H_2 \quad \Delta H_{298K} = 247 kJ\ mol^{-1}$ (2-8)

RWGS: $CO_2 + H_2 \rightleftharpoons CO + H_2O \quad \Delta H_{298K} = 41 kJ\ mol^{-1}$ (2-9)

Bi-reforming of methane:

$CH_4 + H_2O \rightleftharpoons CO + 3H_2 \quad \Delta H_{298K} = 207 kJ\ mol^{-1}$ (2-10)

$CH_4 + CO_2 \rightleftharpoons 2CO + 2H_2 \quad \Delta H_{298K} = 247 kJ\ mol^{-1}$ (2-10)

Tri-reforming of methane:

$CH_4 + H_2O \rightleftharpoons CO + 3H_2 \quad \Delta H_{298K} = 207 kJ\ mol^{-1}$ (2-11)

$$CH_4 + \frac{1}{2}O_2 \rightarrow 2CO + 4H_2 \quad \Delta H_{298K}=-36kJ\ mol^{-1} \tag{2-12}$$

$$CH_4 + CO_2 \rightleftharpoons 2CO + 2H_2 \quad \Delta H_{298K}=247kJ\ mol^{-1} \tag{2-13}$$

Graciano et al. investigated tri-reforming of a CO_2-rich natural gas to produce syngas for manufacturing of GTL products. [25]. The tri-reformer produced a syngas with an H_2/CO ratio of 1.57 to be fed to a slurry FT reactor operating at 240 ºC and 30 bar with 80% CO conversion. The kinetics of a Co-Re/Al_2O_3 catalyst was used for the simulation of the FT reactor to produce 30 tonnes hr^{-1} of GTL products such as gasoline, kerosene, diesel, and waxes [21]. The GTL products consisted of alkanes and alkenes with the number of carbon atoms ranging from 1 to 30 (C_1 to C_{30}) for alkanes and from 1 to 20 (C_1 to C_{20}) for alkenes. $C_{30}H_{62}$ and $C_{20}H_{40}$ were used as the representatives of alkanes and alkenes with more than 30 and 20 carbon atoms, respectively. The combined tri-reforming-FTS process showed more than 50% CO_2 conversion even with the presence of 30% CO_2 in the natural gas. The economic performance of the plant in the USA and Brazil was evaluated to study the effect of natural gas price on the feasibility of the plant. The American plant with access to cheaper natural gas resulted in a net present value (NPW) of $\$187\times10^6$ after 30 years with a payback period of 7.8 years. On the contrary, the Brazilian plant was not economically viable over 30 years due to the higher price of natural gas, which was roughly twice the American price.

A pilot-scale tri-reforming-FT plant consisting of micro-channel and multi-tubular CO-based FT reactors was studied by Na et al. to produce 1 bbl day^{-1} of GTL products [26]. The tri-reformer, simulated as a kinetic reactor, operated at 900-1000 °C and 25 bar. Three pilot-scale membranes were used to separate and recycle unreacted CO_2 at the outlet of the tri-reformer. The produced syngas had an H_2/CO ratio of 2 with 10% CO_2. In comparison with the multi-tubular fixed-bed

reactor, the micro-channel reactor had a higher overall CO conversion (≈ 83%) and a better temperature control.

A GTL process to produce methanol, ethanol, and GTL fuels from a biogas feed stream rich in CO_2 and CH_4 was modeled and optimized by Hernandez et al [27]. The objective of this study was to find the optimal operating conditions and the compositions of the biogas feed to maximize the profit of the plant. The optimization was done for three H_2/CO ratios of 2.5, 1, and 1.7. Syngas was produced by a tri-reformer, which was simulated based on the kinetic equations of Aboosadi et al. [28]. LTFT and HTFT reactors were used for the manufacturing of liquefied petroleum gas (LPG), gasoline, diesel, and heavy products. The LTFT reactor was a multi-tubular fixed-bed reactor operating at 440-530 K and 30 bar. The wax of the LTFT reactor was sent to a hydrocracking unit operating at 140 bar and temperatures between 570 K and 670 K to produce gasoline and diesel with a wax conversion of 56.7% and a diesel selectivity of 76%. A fluidized-bed reactor was used as the HTFT reactor operating at 590-630 K and 30 bar. The produced hydrocarbons from the HTFT reactor were mixed with the light hydrocarbons from the LTFT reactor and sent to a unit to separate water and then to a distillation column for further purification. It was determined that for the production of the desired GTL fuels, 12×10^6 m^3 y^{-1} biogas with a composition of 75% of CH_4 and 25% of CO_2 was required. The total capital investments (TCI) of the HTFT and LTFT plants were $\$8\times10^6$ and $\$19\times10^6$, respectively. It was determined that the sale price of the GTL products (LPG, gasoline, and diesel) obtained from the LTFT and HTFT plants was higher than their crude oil-based market prices. The LTFT plant showed a better economic performance than the HTFT plant. With applying renewable tax incentives, the cost of diesel production by the LTFT plant was competitive to that of diesel obtained from crude oil refining.

Two GTL processes were developed by Zhang et al. based on bi-reforming of methane and steam methane reforming (SMR) represented by Eqs. (2-10) and (2-11), respectively [29]. The produced syngas in either of the processes had an H_2/CO of 2. Cobalt was used in a micro-channel FT reactor at 235 ºC and 21 bar. The unreached C_1-C_4 gases were separated from C_{5+} at the outlet of the FT reactor and recycled to the FT reactor and the reformers. It was shown that recycling unreacted gases enhanced the energy efficiency of the processes and reduced CO_2 emissions of the plant. The net present value (NPW) of the SMR-FT and bi-reforming-FT plants was $\$105.74\times10^3$ and $\$152.68\times10^3$, respectively. The SMR-FT and bi-reforming plants had an internal rate of return (IRR) of 24.0% and 37.1% and a discounted payback period (DPBP) of 5.9 and 3.5 years, respectively. Although the bi-reforming-FT plant seemed to be more competitive than the SMR-FT plant, the two plants were economically feasible at a plant capacity of 2500 barrel day^{-1}.

The coupling of the RWGS, Eq. (2-9), and FT reactions was simulated by Adelung et al. for the manufacturing of GTL products [30]. Their process consisted of a CO_2 absorption unit to absorb CO_2 from a cement plant, a water electrolysis unit to produce H_2, an RWGS reactor, and an FT reactor as well as product separation and hydro-cracking units. Cobalt was used in the FT reactor, which was simulated as a multi-tubular fixed-bed reactor at 220°C and 25 bar with a chain growth probability of 0.839. Only alkanes were included to simulate the FT reaction. The selected alkanes were C_1H_4 to $C_{30}H_{62}$, $C_{32}H_{66}$ to represent $C_{31}H_{64}$ to $C_{35}H_{72}$, and $C_{36}H_{74}$ to represent alkanes with more than 36 carbon atoms. The RWGS reactor was simulated as a Gibbs reactor to produce syngas. The separated gases at the outlet of the FT reactor were recycled to the RWGS and FT reactors. The purge gases were burnt in a furnace to generate the required heat for the RWGS reaction. The CO_2 in the flue gas of the furnace was separated by monoethanolamine (MEA) to be recycled to the RWGS reactor. It was reported that when the RWGS reactor operated at 725 °C

and 1 bar, a maximum hydrocarbon production of 10.21 tonnes hr^{-1} was achieved with an overall CO_2 conversion of 88%.

Gao et al. performed a comparative analysis on the reformation of CO_2 to syncrude and synthetic natural gas by developing a power to liquid (P2L) plant and a hybrid power to liquid/power to gas (P2L/P2G) plant [31]. The goal of this study was to compare the two plants in terms of energy efficiency, CO_2 consumption, and economic feasibility. Both plants converted the feed CO_2 and hydrogen to syngas through the RWGS reaction. Hydrogen was produced by water electrolysis and the RWGS reactor operated at 800 °C and 30 bar. An Fe-based FT reactor operating at 300 °C and 30 bar was simulated with a conversion reactor based on fractional conversions of CO obtained from experimental data. C_2-C_4 alkenes and alkanes were represented by C_3H_6 and C_3H_8, respectively. C_{5+} hydrocarbons were represented by $C_{12}H_{26}$. The hybrid P2L/P2G plant produced 0.47-0.78×10^6 bbl yr^{-1} of syncrude and 3.66-1.67×10^6 MMBTU yr^{-1} of high calorie natural gas. The P2L plant generated 1.02×10^6 bbl yr^{-1} of syncrude. The project life was assumed to be 20 years with a taxation rate equal to 2% of the plants' fixed capital investment. Two scenarios with low and high syncrude and natural gas prices were considered for economic analysis. \$140 bbl^{-1} and \$19.6 $MMBTU^{-1}$ were assumed in the low-price scenario for syncrude and natural gas, respectively. In the high-price scenario, \$200 bbl^{-1} and \$28 $MMBTU^{-1}$ were assumed for syncrude and natural gas, respectively. The TCI of the P2L and P2L/P2G plants was estimated at \$418×10^6 and \$233-278×10^6, respectively. It was concluded that the P2L/P2G plant was a more competitive design. Sensitivity analysis showed that the hydrogen price had a major influence on the profitability of the plant. The total production cost of syncrude by the P2L plant was \$258.44 bbl^{-1}, which was higher than that of the P2L/P2G plant at \$225.65-239.12 bbl^{-1}.

A P2L plant based on the RWGS and FT reactions was simulated by Konig et al. [32]. The capacity of the plant was 1260 bbl day^{-1} of syncrude (24.9% of diesel, 31.2% of gasoline, and 439% of kerosene). Hydrogen was produced by the electrolysis of water powered by offshore wind as a renewable energy. The RWGS reactor was simulated at 900 °C and 2.5 MPa. A cobalt catalyst was used in the FT reactor operating at 225 °C and 2.5 MPa. Only 32 alkanes were included to simulate the FT reactor, i.e., CH_4 to $C_{30}H_{66}$ as well as $C_{32}H_{66}$ and $C_{36}H_{74}$. The distribution of hydrocarbons was determined by the ASF model with the chain growth probability of 0.85. The single pass and overall conversion of CO in the FT reactor was 40% and 80%, respectively. Although the plant had a high CO_2 conversion of 74%, it was not economically feasible. The cost of renewable energy to produce 100 MW_{LHV} of hydrogen using the offshore wind was \$160 MWh^{-1}. This electricity cost resulted in a syncrude with a production cost of \$460 bbl^{-1}, which was four times higher than the crude oil price in 2013 (\$109 bbl^{-1}). The study indicated that the cost of electrolyzers and the electricity for hydrogen production greatly influenced the manufacturing cost of the GTL products.

The production of 351 tonnes of syncrude per day in a GTL plant with a product mass ratio of 1/182/1.08 of naphtha/jet fuel/diesel was investigated by Zang et al. [33]. The GTL plant involved six main units: H_2 and CO_2 compression, syngas production by the RWGS reaction, GTL production by the FTS, product upgrading by hydrotreating, energy generation by Rankine cycle, and utilities. 223 tonnes day^{-1} of CO_2 was obtained from an ethanol plant. 2387 tonnes day^{-1} of hydrogen were generated by water electrolysis. The RWGS reactor was simulated based on an experimental kinetic model at 600 °C and 24.5 bar [34]. The single pass CO_2 conversion of the reactor was 36%. Cobalt was used in an FT reactor operating at 220 °C and 24.3 bar. The single pass and overall CO conversion of the FT reactor was 52.2% and 80%, respectively. The

simulation was restricted to the production of alkanes from C_1H_4 to $C_{20}H_{44}$ and $C_{30}H_{63}$ (representative of alkanes heavier than $C_{20}H_{44}$). A constant value of 0.9 was assumed for the chain growth probability. The carbon efficiency of the plant, defined as the mass ratio of produced hydrocarbons (naphtha, jet fuel, and diesel) to the input CO_2, was 45.5%. The TCI of the plant was estimated to be $\$379\times10^6$. Economic analysis of the plant showed that H_2 price was the most influential economic factor on the feasibility of the plant. With an H_2 price of \$2 kg^{-1} (produced by water electrolysis), the minimum selling price of mixed FT fuels was reported to be \$5.4-5.9 gal^{-1}, which was more expensive than the price of diesel obtained from crude oil. It was reported that with CO_2 price of \$ 0.0173 kg^{-1}, the hydrogen price should be reduced to \$0.8 kg^{-1} to make the FT fuels economically competitive with conventional fuels.

Liu et al. performed a life cycle analysis (LCA) on a process to convert captured CO_2 from air to produce 9800 bbl day^{-1} of diesel [35]. The process involved the hydrogenation of the captured CO_2 to syngas through the RWGS reaction. The produced syngas was then sent to a Co-based multi-tubular fixed-bed FT reactor operating at 220 °C and 3 MPa with 80% conversion of syngas to diesel. A power law kinetic model was used to simulate the FT reactor. A water electrolyzer powered by renewable energy was applied to produce hydrogen. The LCA showed that 29 g of CO_2 was emitted per 1 MJ of the synthetic fuel combusted. This was equivalent to 0.57 g of CO_2 emissions for 1 g of the captured CO_2 from air. It was concluded that the availability of electricity with carbon intensity less than 139 g CO_2 kWh^{-1} was required to make the plant environmentally more advantageous compared to fossil-fuel based plants. Since the electricity with the low carbon intensity had the major effect on the viability of the plant, it was suggested to construct these types of plants in the regions with abundant and cheap renewable resources such as Argentina and parts of the USA.

Fasihi et al. investigated the economic feasibility of a P2L plant to produce 31170 bbl day^{-1} of liquid hydrocarbons (mostly diesel with the capacity of 21188 bbl day^{-1}) from CO_2 by the combination of the RWGS and LTFT reactions [36]. H_2 was produced by water electrolysis powered by a hybrid solar and wind system. CO_2 was captured from air. It was reported that the cost of diesel production from the hybrid solar-wind system was \$135 bbl^{-1}, which was not competitive with the current market price of diesel. Sale of oxygen as a by-product of the P2L plant and access to cheap renewable energies were suggested to improve the economic performance of the plant.

The production cost of wax from a GTL plant based on the RWGS and FT reactions was investigated by Marchese et al. [37]. H_2 was produced by water electrolysis using various types of renewable energies. The production cost of the wax was €5.05-25 kg^{-1}, €6.3-26.3 kg^{-1}, and €7.4-27.4 kg^{-1} for an interest rate of 0%, 7.5%, and 12.5%, respectively. The lowest wax production cost in each range was associated with H_2 production using the electricity produced from hydropower. On the other hand, the highest wax production cost in each range was related to H_2 production using the electricity obtained from the combination of different renewable energies such as wind, geothermal, and solar. It was concluded that the availability of cheap renewable H_2 is vital for commercial viability of CO_2 to GTL plants. A review paper by Brynolf et al. also indicated that the commercial feasibility of CO_2 reformation to GTL products was highly correlated to the production cost of renewable H_2 [38].

A P2L plant with two processes was analyzed by Marchese et al. for syngas production based on the utilization of 1 ton/h of captured CO_2 from a biogas upgrading unit [39]. In the first process, a RWGS unit was used for syngas production from the hydrogen generated by low-temperature electrolysis. . The RWGS reactor was simulated using a Gibbs reactor at 1073 K and atmospheric

pressure. In the second process, the RWGS reactor was replaced with a solid oxide electrolysis cell (SOEC) to directly produce syngas from H_2O and CO_2 at 1073 K and atmospheric pressure. The reactions in the cathode and anode of the SOEC are given by Eqs. (2-14) to (2-16):

Cathode side:

$$H_2O + 2\ e^- \rightarrow H_2 + O^{2-} \quad (2\text{-}14)$$

$$CO_2 + 2\ e^- \rightarrow CO + O^{2-} \quad (2\text{-}15)$$

Anode side:

$$O^{2-} \rightarrow 0.5\ O_2 + 2\ e^- \quad (2\text{-}16)$$

A Co-based multi-tubular FT reactor was used at 501 K and 25 bar with a single pass CO conversion of 75%. A detailed kinetic model based on the carbide mechanism was used for the Co catalyst [27]. The reaction rates of alkanes and alkenes were considered up to $C_{80}H_{162}$ and $C_{40}H_{80}$, respectively. The comparison between the two proposed plants indicated that the conversion of CO_2 by the RWGS reaction was lower than that of the SOEC due to the thermodynamic limitations of the RWGS reaction. From an environmental point of view, both plants had a high potential for the conversion of CO_2, which was reported to be 81.7% and 79.4% for the RWGS and SEOC plants, respectively. The most energy demanding unit in both plants was CO_2 separation from biogas by MEA. It was concluded that the choice of hydrogen production and CO_2 capturing methods had a direct effect on the energy consumption and hydrocarbon production rate of the plants.

The feasibility of a SEOC for the manufacturing of GTL products was also evaluated by Graves et al. [40]. CO_2 was captured from air and the energy of the SEOC was provided by renewable

sources such as solar, wind, hydro, and geothermal energies as well as nuclear power. An Fe-based FT reactor was used for the production of hydrocarbons. An economic analysis on gasoline production cost indicated that the cost of electricity for the production of synthetic gasoline ($0.53 L^{-1}) must be (2-3 cents) kWh^{-1} to make the produced fuel competitive with the current market price. The economic analysis indicated that the capital cost of the electrolyzer and the cost of renewable electricity were major obstacles in the economic feasibility of the plant.

2.2.2. Direct CO_2 hydrogenation

In contrast to the indirect CO_2 hydrogenation route, there are not many papers published on the feasibility of direct reformation of CO_2 to hydrocarbons. This is mainly related to the lack of catalyst formulations that could directly reform CO_2 to GTL products. However, there are a few articles that have studied GTL plants based on direct CO_2 hydrogenation, especially via the Fe-based FTS.

Zhang et al. simulated a P2L plant and a hybrid P2L/P2G plant for direct hydrogenation of 0.37×10^6 tonnes CO_2 yr^{-1} to GTL products and synthetic natural gas [41]. Captured CO_2 from cement, steel, and power plants were fed to the plants. Hydrogen was produced from water electrolysis powered by renewable resources. An Fe-based FT reactor operating at 300 °C and 25 bar produced C_2-C_4 alkanes, alkenes, and C_{5+} which were represented by C_3H_6, C_3H_8, and $C_{12}H_{26}$, respectively. The project life was assumed to be 20 years with a syncrude sale price of $140 bbl^{-1} and a synthetic natural gas sale price of $19.6 $MMBTU^{-1}$ as a reference scenario in 2030. It was determined that the P2L/P2G could be more economically competitive than the P2L plant. By increasing the plant capacity to 4×10^6 tonnes yr^{-1}, the cost of CO_2 abatement was reduced for both plants. The P2L/P2G plant showed a lower CO_2 abatement cost compared to the P2L plant. The TCI of the P2L plant was $1550.28 (tonne CO_2)$^{-1}$ yr^{-1}, which was higher than that of the P2L/P2G

plant at \$532.90-662.93 (tonne CO_2)$^{-1}$ yr^{-1}. The energy efficiency of the hybrid P2L/P2G plant was 75.9-67.7%, which was also higher than the P2L plant at 49.2%. As a result, the hybrid P2L/P2G plant was more economically favourable when compared with the P2L plant because of its high energy efficiency, lower TCI, and the lower carbon abatement cost.

Do and Kim investigated direct CO_2 conversion to light hydrocarbons such as C_2-C_4 [42]. CO_2 was captured from the flue gas of a coal-fired power plant, with CO_2, O_2, N_2, and H_2O mole percent of 21%, %3, 66%, and11%, respectively. Hydrogen was produced by water electrolysis powered by renewable resources such as wind and solar energies. An Fe-based FT reactor was simulated as a fixed-bed reactor operating at 290-360 °C and 10 bar. Based on the simulation results, the carbon and energy efficiency of the plant was estimated to be 99.2% and 42%, respectively. It was shown that 3.89 kg of CO_2 was consumed for the production of 1 kg of GTL products. The direct and indirect CO_2 emissions of the plant were 0.03 and 2.01 kg CO_2 per 1 kg of GTL products, which showed that the plant was a net consumer of the CO_2. The production cost of 1 kg of C_2-C_4 was \$3.58, which was caused by the high cost of hydrogen production by water electrolysis. It was suggested that reduction of the price of renewable hydrogen was necessary to make the plant economically feasible.

In a review paper, Panzone et al. studied the economic performance of several CO_2 hydrogenation routes to manufacture value-added chemicals including GTL products [43]. It was concluded that fuels produced by P2L plants were not competitive with their current fossil fuel-based market prices. The high price of renewable electricity needed for H_2 production using water electrolysis was mentioned to be one of the main reasons for the infeasibility of P2L plants. However, it was predicted that P2L plants might become feasible in the next 30 years by lowing the production cost of renewable H_2 and investment in the construction of large-scale plants.

From the reviewed literature, it can be said that the synthesis of hydrocarbons by CO_2 hydrogenation either via direct or indirect pathways faces economic challenges to compete with fossil fuels. The production cost of renewable hydrogen and the type of technology applied to produce hydrogen play a vital role in the economic feasibility of CO_2 to GTL plants. Although most of proposed GTL plants have acceptable environmental performance, they struggle to compete with current market prices. Since hydrogen price from water electrolysis is one the bottlenecks of CO_2 to GTL processes, this thesis investigates the feasibility of CO_2-free hydrogen production by thermal decomposition of methane in a CO_2 to syncrude plant. This work evaluates the economic and environmental feasibility of the proposed plant, which consists of methane decomposition, RWGS, and LTFT units to determine whether or not it can be a good candidate to convert CO_2 to GTL products.

2.3. Knowledge gaps and hypothesis

The reviewed articles reveal the following knowledge gaps for the hydrogenation of CO_2 to GTL products:

1. Hydrogen is mostly produced by water electrolysis to be used for the reformation of CO_2 to value-added chemicals. Since the hydrogen production cost affects the economic feasibility of CO_2 to GTL products, alternative hydrogen production methods and technologies should be investigated. Is there another pathway to produce CO_2-free hydrogen, which overcomes the economic hurdle of water electrolysis?
2. FT reactions have an essential role in the distribution of GTL products. The majority of simulations of GTL plants in the literature only consider a limited number of carbon atoms, which would result in inaccurate estimation of GTL products distribution, especially for

heavier hydrocarbons such as wax. What is the minimum number of carbon atoms required for accurate simulation of an FT reactor?

3. The main goal of reported GTL plants is the utilization of CO_2. More detailed analysis is necessary to address the CO_2 emissions of such plants for comparison with conventional plants and other reaction routes for the reformation of CO_2 to value-added chemicals. The published articles mainly focus on economic feasibility of CO_2 to GTL plants while they do not address how to reduce CO_2 emissions of such plants. What can be done to minimize CO_2 emissions of CO_2 to GTL plants while maximizing their CO_2 utilization as a feedstock?

The hypothesis of this thesis is to reduce CO_2 emission of a CO_2 to syncrude plant by production of CO_2-free hydrogen via thermal pyrolysis of methane in order to develop a process concept with favourable economic and environmental performance.

2.3. Thesis Objectives

The objectives of this thesis are to:

1. Apply thermal decomposition of methane in a liquid metal bubble reactor (LMBR) to produce CO_2-free hydrogen.
2. Use the RWGS reaction for the hydrogenation of CO_2 to syngas to be converted to syncrude in a low temperature FT reactor.
3. Accurately simulate the FT reactor with sufficiently high number of carbon atoms.
4. Evaluate the economic and environmental performance of the proposed LMBR-RWGS-FT plant to produce 30,000 bbl day^{-1} of syncrude.

Chapter 3: Process block flow diagram and methodology

This chapter first presents the block flow diagram of a GTL plant based on the combination of thermal decomposition of methane in a liquid metal bubble reactor to produce hydrogen, the RWGS reaction for the reformation of CO_2 to syngas, and the LTFT reaction to produce synthetic crude. The methodology to simulate the process based on coupling MATLAB and HYSYS is presented in Section 3.2. The kinetic and governing differential equations to model the methane decomposition, RWGS, and FT reactors are given in Section 3.3, 3.4, and 3.5, respectively. The utilities are explained in Section 3.6. The validation of the kinetics of the RWGS and FT reactions is provided in Appendices A and B, respectively.

3.1. Process block flow diagram

Fig. 3.1 shows the block flow diagram (BFD) of the GTL plant, which is designed to produce 30000 bbl/day of syncrude. The BFD consisted of six units, i.e., hydrogen production by a methane decomposition reaction (MDR), hydrogen separation by pressure swing absorption (PSA), syngas production by the RWGS reaction, CO_2 separation and recycling by monoethanol amine (MEA), syncrude manufacturing by the LTFT reaction, and electricity generation from steam produced in the plant.

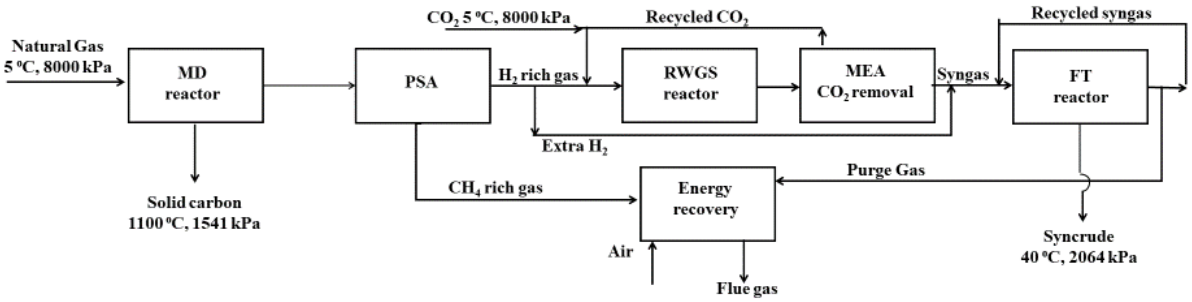

Fig. 3.1. The block flow diagram of the GTL plant

The natural gas feed (5 °C and 8000 kPa) with molar composition of CH_4:0.8871, C_2H_6: 0.0693, C_3H_8: 0.0125, C_4H_{10}:0.0028, C_5H_{12}:0.0005, C_6H_{14}:0.0002, N_2:0.0082 and CO_2:0.0194 is fed to an isothermal MDR to decompose methane to solid carbon and hydrogen. The product gas stream of the MDR is sent to the PSA unit to separate hydrogen from unreacted methane and inert gases. Two high purity hydrogen streams are taken from the PSA unit. The first stream is used in the RWGS reactor to reform CO_2 feed, which is taken from pipeline at 5 ºC and 8000 kPa. The second hydrogen stream is mixed with the syngas produced in the RWGS unit to adjust its H_2/CO ratio to 2.1. The MEA unit separates the unreacted CO_2 from the syngas to be recycled to the RWGS reactor. The syngas with the adjusted H_2/CO ratio is mixed with the recycled stream of the FT unit and introduced to the LTFT reactor for the synthesis of syncrude. The purge gases from the PSA and FT units are burnt in a furnace to provide energy required by the RWGS and MDR reactors, to heat process streams, and to produce steam for electricity generation.

3.2. Simulation

3.2.1. Software

Aspen HYSYS V11, MATLAB R2019b, Aspen Plus V11, and Aspen Exchanger Design and Rating (EDR) V11 are used in this thesis to simulate the GTL plant. MATLAB is used to simulate the FT and RWGS reactors and converge their recycle streams. The ode 23s function is used to integrate the governing differential equations of the FT and RWGS reactors. The dimensions and operating condition of the MDR are also found by MATLAB. Aspen HYSYS is used as the main platform to simulate the process. EDR is used for the design of shell-and-tube heat exchangers. Aspen Plus is applied to accurately calculate the heat demand of the MDR since Aspen HYSYS is not suitable for the calculation of the heat of reaction of the MDR in the presence of solid carbon. The selected fluid packages in Aspen HYSYS are the Peng-Robinson for the MDR, RWGS, and FT units, the Acid Gas-Chemical Solvent for the MEA unit, and the ASME Steam for cooling water (CW) and steam.

3.2.2. Coupling of MATLAB and HYSYS

The connection between HYSYS and MATLAB is activated by an ActiveX server. This server enables HYSYS and MATLAB to exchange data during the connection. The required MATLAB functions for the connection and cooperation between the two types of software are summarized in Table 3.1.

Table 3.1. HYSYS and MATLAB coupling functions

Function Number	Function	Description
1	h = actxserver	To create an ActiveX server
2	hycase = h.Activedocument	To connect MATLAB to active HYSYS file
3	Sol = hyCase.Solver	To connect to the HYSYS solver
4	f = hy.Case.Flowsheet	To connect to the HYSYS flowsheet
5	g = f.Materialstreams	To connect to HYSYS material streams
6	Sol.CanSolve = 1	To activate the HYSYS solver
7	A = g.Item('B').C	To import data from HYSYS to MATLAB
8	g.Item ('B').C = A	To export data from MATLAB to HYSYS

The connection between MATLAB and Aspen HYSYS occurs via functions No. 1-6. to export any data from Aspen HYSYS to MATLAB. Function No. 7 should be used for exporting data from Aspen HSYSY to MATLAB, where A is the name of a variable defined in MATLAB, B is the name of a material stream in Aspen HYSYS, and C is any data (e.g., temperature, pressure, flow rate, etc.) in a material stream to be exported to MATLAB. To import any information from MATLAB to Aspen HYSYS, function No. 8 should be used.

In this thesis, the FT and RWGS packed-bed reactors are simulated in MATLAB since their kinetic equations are in mathematical forms that are different from the default Heterogeneous Catalytic type in Aspen HYSYS. The required data such as the FT and RWGS reactors inlet temperature, pressure, molar flow rate, and composition are exported from Aspen HYSYS to

MATLAB to integrate the material, momentum, and energy balance differential equations of the reactors. The calculated outlet temperature, pressure, and component molar flow rates of the reactors are then sent back to Aspen HYSYS.

The recycle streams of the FT and RWGS reactors are converged in MATLAB. A "while" loop with a tolerance of 0.001% is used in MATLAB to converge the recycle streams of the reactors. The tolerance of the "while" loop is defined by Eq. (3-1):

$$\text{Tolerance } (\%) = \frac{F_{feed,n} - F_{feed,n-1}}{F_{feed,n-1}} \times 100 \quad (3\text{-}1)$$

where $F_{feed,n}$ and $F_{feed,n-1}$ are the inlet molar flow rates of the FT or RWGS reactors in iteration number "n" and "n-1", respectively. It should be noted that the recycle loop of the MEA unit is converged by Aspen HYSYS. Despite using MATLAB to find the dimensions and the operating conditions of the MDR, no connections are made between MATLAB and Aspen HYSYS for the MDR.

3.3. Modelling of the MDR in MATLAB

In this study, hydrogen is produced via catalytic decomposition of methane in an isothermal liquid metal bubble reactor (LMBR) containing molten copper and bismuth ($Cu_{0.45}Bi_{0.55}$). The MDR is a multi-tubular reactor located in a fired heater to provide the heat of the reaction. The mathematical modeling of the MDR is based on the work of Catalan and Rezaei (unpublished) to find the optimum height, inlet pressure, and feed flow rate per tube of the reactor. In this section, only the kinetic equations of the methane decomposition reaction and the differential equations of the model are presented.

3.3.1. Kinetics of catalytic methane decomposition in molten copper-bismuth

The methane decomposition reaction, Eq. (3-2), is an alternative chemical route to water electrolysis for the production of CO_2-free hydrogen. In this method, a catalytic or non-catalytic LMBR is used for the decomposition of methane, which would facilitate the separation of the produced carbon from the top of the reactor.

$$\mathrm{CH_4} \leftrightarrow \mathrm{H_2} + \mathrm{C} \qquad (3-2)$$

The kinetics of catalytic methane decomposition in molten Cu-Bi is given by Catalan and Rezaei [44]:

$$\mathrm{r_{CH_4}} = \mathrm{k}_{nc}\mathrm{C}^{\mathrm{n}}_{\mathrm{CH_4}}\left(1-\frac{\mathrm{C}^2_{\mathrm{H_2}}}{\mathrm{C_{CH_4}K_C}}\right) + a_g\mathrm{k}_c\mathrm{C_{CH_4}}\left(1-\frac{\mathrm{C}^2_{\mathrm{H_2}}}{\mathrm{C_{CH_4}K_C}}\right) \qquad (3-3)$$

where $\mathrm{r_{CH_4}}$(mol $m^{-3}s^{-1}$) is the reaction rate of methane decomposition, k_{nc} ($mol^{(1-n)}$ $m^{-3(1-n)}$ s^{-1}) and k_c (m s^{-1}) are the non-catalytic and catalytic reaction rate constants, respectively, which are calculated by the Arrhenius equations presented by Eqs. (3-4a) and (3-4b), a_g is the interfacial surface area per unit volume of gas (m^2 m^{-3}), $\mathrm{C_{CH_4}}$ and $\mathrm{C_{H_2}}$ (mol m^{-3}) are the concentration of the methane and hydrogen, respectively, and K_C (mol m^{-3}) is the equilibrium constant of the reaction, which is expressed by Eq. (3-5):

$$\mathrm{k}_{nc} = \mathrm{k}_{o,nc}\exp\left(\frac{-\mathrm{E_{a,nc}}}{\mathrm{RT}}\right) \qquad (3-4a)$$

$$\mathrm{k}_c = \mathrm{k}_{o,c}\exp\left(\frac{-\mathrm{E_{a,c}}}{\mathrm{RT}}\right) \qquad (3-4b)$$

$$\mathrm{K_C} = \left(\frac{10^5}{8.314\mathrm{T}}\right)\exp\left(13.2714-\frac{91204.6}{\mathrm{RT}}\right) \qquad (3-5)$$

in which $E_{a,nc}$ and $E_{a,c}$ (J mol^{-1}) are the activation energies of the non-catalytic and catalytic reactions, respectively. T (K) is temperature and R (8.314 J mol^{-1} K^{-1}) is the universal gas constant. $k_{o,nc}$ (s^{-1} $mol^{(1-n)}$ $m^{-3(1-n)}$) and k_{oc} (m s^{-1}) are the pre-exponential constants of the non-catalytic and catalytic reactions, respectively. The required information for the calculation of equilibrium and rate constants is given in Table 3.2.

Table 3.2. Kinetic parameters to be used with Eqs. (3-3) and (3-4)

Non-catalytic parameters		
Parameter	**unit**	**value**
$\mathbf{k_{o,nc}}$	$mol^{(1-n)}$ $m^{-3(1-n)}$ s^{-1}	1.4676×10^{4}
$\mathbf{E_{a,nc}}$	J mol^{-1}	284,948
n	-	1.0809
Catalytic parameters		
$\mathbf{k_{o,c}}$	m s^{-1}	4.32×10^{5}
$\mathbf{E_{a,c}}$	J mol^{-1}	222,000

The material and pressure differential equations of the MDR are given by Eqs. (3-6) and (3-7), respectively:

$$\frac{dX_{CH_4}}{dL} = \frac{\alpha\,\pi D^2}{4}\left\{\frac{a_g\,k_c\left(1-X_{CH_4}\right)}{\left(\dot{n}_{CH_4,b}+\dot{n}_{H_2,b}+\dot{n}_{I,b}\right)\left(1+\varepsilon X_{CH_4}\right)}\left(\frac{P}{RT}\right)\right.$$
$$\left.+\,k_{nc}\left[\frac{\left(1-X_{CH_4}\right)}{\left(\dot{n}_{CH_4,b}+\dot{n}_{H_2,b}+\dot{n}_{I,b}\right)\left(1+\varepsilon X_{CH_4}\right)}\left(\frac{P}{RT}\right)\right]^n\right\}$$
$$\cdot\left\{1-\frac{\dot{n}_{CH_4,b}\left(\theta_{H_2}+2X_{CH_4}\right)^2}{\left(\dot{n}_{CH_4,b}+\dot{n}_{H_2,b}+\dot{n}_{I,b}\right)\left(1+\varepsilon X_{CH_4}\right)\left(1-X_{CH_4}\right)\cdot K_C}\left(\frac{P}{RT}\right)\right\} \qquad (3-6)$$

where dX_{CH_4} (dimensionless) is the change in methane conversion, dL (m) is the change in the length of the reactor, D (m) is the reactor inner diameter, P (Pa) is pressure, T (K) is temperature, θ_{H_2} is the molar ratio of H_2 to CH_4 in the feed, α is the gas holdup (unitless), and ε (unitless) is the mole fraction of CH_4 in the feed. $\dot{n}_{CH_4,b}$, $\dot{n}_{H_2,b}$, and $\dot{n}_{I,b}$ (mol s^{-1}) are the molar flow rate of CH_4, H_2, and inert components at the bottom of the reactor, respectively.

$$\frac{dP}{dL} = -\left[\rho_l(1-\alpha)+\rho_g\alpha\right]g = -\left(\rho_l-\alpha\Delta\rho\right)g \qquad (3-7)$$

dP (Pa) is the pressure change of gas throughout the reactor, ρ_l (kg m^{-3})is the density of the liquid metal, ρ_g (kg m^{-3}) is the density of gas, $\Delta\rho$ (kg m^{-3}) is the density difference between liquid metal and gas, and g (9.81 m s^{-1}) is the gravitational acceleration. The equations to calculate α and a_g as well as the physical properties of the Cu-Bi melt are available in the work of Catalan and Rezaei [44]. It should be noted that complete conversion of C_2 plus hydrocarbons to hydrogen and carbon is assumed in the MDR.

3.4. Modelling of the RWGS reactor

The RWGS reactor is a fixed-bed tubular reactor packed with a Ni-$Al_{12}O_{19}$ catalyst. The RWGS kinetics is based on the experimental work of Unde [45], which are explained in more detail in Sections 3.4.1 and 3.4.2. The following assumptions are made for the modelling of the RWGS reactor in MATLAB:

1. Steady state conditions.

2. No axial mass and heat dispersion in the gas phase.

3. No radial mass transfer (one dimensional).

3. Ideal gas behavior.

4. No external heat transfer resistance for the catalyst particles (the temperature of the catalyst particles is equal to the temperature of the gas phase).

3.4.1. Kinetics of the RWGS reaction

Since the RWGS reaction is a heterogeneous catalytic reaction, the influence of the internal and external mass transfers should be taken into account. The RWGS reaction rate, r_{RWGS} (mol $kg^{-1}s^{-1}$), of the Ni-$Al_{12}O_{19}$ catalyst is determined by Eq. (3-8) [45]:

$$r_{RWGS} = \left(\frac{1}{r_{pore}} + \frac{1}{r_{ext}}\right)^{-1} \qquad (3-8)$$

where r_{pore} (mol $kg^{-1}s^{-1}$) and r_{ext} (mol $kg^{-1}s^{-1}$) denote the reaction rates controlled by internal and external mass transfers, respectively, which are explained in more detail in Sections 3.4.1.1 and 3.4.1.2.

3.4.1.1. Internal mass transfer

The r_{pore} (mol $kg^{-1}s^{-1}$) given by Eq. (3-9) describes the reaction rate that is controlled by the mass transfer inside the catalyst pores:

$$r_{pore} = \eta k_{CO_2}\left(C_{CO_2} - \frac{C_{CO}C_{H_2O}C_{H_2}^{-1}}{K_c}\right) \quad (3-9)$$

in which η (unitless) is the effectiveness factor, C (mol m^{-3}) is the concentration of species (CO, H_2O, CO_2, and H_2), k_{CO_2}(m^3 kg^{-1} s^{-1}) is the reaction rate constant, which is calculated by Eq. (3-10) with k_0 and E_a equal to 17000 m^3 kg^{-1} s^{-1} and 68.5 kJ mol^{-1}, respectively. K_C (unitless) is the equilibrium constant of the RWGS reaction, which is determined by Eqs. (3-11) and (3-12) [45].

$$k_{CO_2} = k_0 \exp\left(\frac{-E_a}{RT}\right) \quad (3-10)$$

$$K_C = \left(\frac{1}{\exp(-0.2353Z^3 + 0.63508Z^2 + 4.1778Z + 0.31688)}\right) \quad (3-11)$$

$$Z = \left(\frac{1000}{T}\right) - 1 \quad (3-12)$$

T in Eqs. (3-10) and (3-12) is in K.

The effectiveness factor is defined as the ratio of the actual reaction rate to the rate of reaction with no internal mass transfer limitations. The effectiveness factor is a function of the Thiele modules φ (unitless) with a value between 0 and 1. The effectiveness factor is calculated by Eq. (3-13) [45].

$$\eta = \frac{1}{\varphi}\left[\frac{1}{\tan(3\varphi)} - \frac{1}{3\varphi}\right] \approx \frac{\tan(\varphi)}{\varphi} \quad (3-13)$$

The Thiele modules is determined by Eq. (3-14) [45]:

$$\varphi = \frac{d_p}{6}\sqrt{\left(\frac{K_C + 1}{K_C}\right)\frac{k_{CO2}\,\rho_p}{D_{CO2,eff}}} \qquad (3-14)$$

where dp (m) is the diameter of the catalyst particles, k_{CO_2} ($m^3\ kg^{-1}\ s^{-1}$) is the reaction rate constant calculated by Eq. (3-10), ρ_P ($kg\ m^{-3}$) is the solid density of the catalyst particles, K_C (unitless) is the equilibrium constant calculated by Eq. (3-11), and $D_{CO_2,eff}$ ($m^2\ s^{-1}$) is the effective diffusion coefficient inside the catalyst pores, which is given by Eq. (3-16):

$$D_{CO_2,eff} = \frac{\varepsilon_P}{\tau_P}\left(\frac{1}{D_{CO_2,mol}} + \frac{1}{D_{CO_2,knu}}\right)^{-1} \qquad (3-16)$$

where ε_P (unitless) is the catalyst porosity, τ_P (unitless) is the tortuosity of the particles, $D_{CO_2,mol}$ ($m^2\ s^{-1}$) is the molecular diffusion coefficient, and $D_{CO_2,knu}$ ($m^2 s^{-1}$) is the Knudsen diffusion coefficient. Depending on the ratio of the pore radius to the mean free path of diffusing species, $D_{CO_2,mol}$ or $D_{CO_2,knu}$ can be dominant to control the mass transfer in the catalyst pores.

The molecular diffusion coefficient is calculated by Eq. (3-17), which is dominant when the ratio of the catalyst pore radius to the mean free patch is higher than 10. In this case, the concentration gradient is the driving force for the diffusion inside the catalyst pores.

$$D_{CO_2,mol} = \frac{1 - y_i}{\sum_{j \neq i} \frac{y_i}{D_{ij}}} \qquad (3-17)$$

yi is the molar fraction of diffusing gases (CO, CO_2, H_2, H_2O, and N_2) and D_{ij} ($m^2\ s^{-1}$) is the effective diffusivity of gas species given by the following equation:

$$D_{ij} = \left(\frac{AT^B}{P}\right)\left(Ln\left(\frac{C}{T}\right)\right)^{-2D} \exp\left(-\frac{E}{T} - \frac{F}{T^2}\right) \times 10^{-4} \qquad (3-18)$$

where T (K) is temperature and P (atm) is pressure. Parameters A to F are included in Table 3.3. [46].

Table 3.3. Diffusivity parameters to be used in Eq. (3-18) [46]

Pair	A	B	C	D	E	F
H_2-CO_2	3.14×10^{-5}	1.75	-	0	11.7	0
CO-CO_2	3.15×10^{-5}	1.57	-	0	113.6	0
N_2-H_2O	3.15×10^{-5}	1.57	-	0	113.6	0
CO_2- H_2O	9.24×10^{-5}	1.5	-	0	307.9	0

When the ratio of the catalyst pore radius to the mean free path is lower than 1, the collision of molecules with the pore wall results in a diffusion coefficient known as the Knudsen diffusion coefficient, $D_{CO_2,knu}$ ($m^2\ s^{-1}$), which is expressed by Eq. (3-19) [47].

$$D_{CO_2,knu} = 19400\frac{\varepsilon_P}{S_g\rho_b}\sqrt{\frac{T}{M_{CO_2}}}\times 10^{-4} \qquad (3-19)$$

in which S_g ($cm^2\ g^{-1}$) is the BET surface area of the porous particles, M_{CO_2} (g mol^{-1}) is the molecular weight of CO_2, ρ_b (g cm^{-3}) is the bulk density of the catalyst, and T (K) is temperature. The characteristics of the Ni-$Al_{12}O_{19}$ catalyst are summarized in Table 3.4 [45].

Table 3.4. Characteristics of the Ni-$Al_{12}O_{19}$ catalyst [45]

Parameter	Unit	Value
BET surface area (S_g)	m^2g^{-1}	3
Porosity of catalyst (ε_P)	-	0.33
Tortuosity of particle (τ_P)	-	1.6
Catalyst particle diameter (d_p)	-	0.006
Particle density (ρ_p)	Kg m^{-3}	1910
Bulk density (ρ_b|)	Kg m^{-3}	1200
Geometry (spherical)	-	-

3.4.1.2. External mass transfer

The external mass transfer or film diffusion affects the reaction rate on the external surface of the catalyst. The external mass transfer resistance is negligible at high gas velocities. The external reaction rate, r_{ext} (mol kg^{-1} s^{-1}), is expressed by Eq. (3-20) [45]:

$$r_{ext} = \beta A_{ext}\left(C_{CO_2} - C_{CO_2,eq}\right) \qquad (3-20)$$

where A_{ext} (m^2 Kg^{-1}) is the external surface area of the catalyst, which is calculated by Eq. (3-21), β (m s^{-1}) is the external mass transfer coefficient, and $C_{CO_2,eq}$ (mol m^{-3}) is the equilibrium concentration of CO_2, which is calculated by Eq. (3-28), explained below.

$$A_{ext} = \frac{6}{d_P \rho_P} \qquad (3-21)$$

The external mass transfer coefficient (β) is a function of the Sherwood number (Sh) given by Eq. (3-22) [45]:

$$\beta = \frac{\mathrm{Sh}\, D_{CO_2,mol}}{d_P} \qquad (3-22)$$

The Sherwood number is expressed by Eqs. (3-23) and (3-24) as a function of the Reynolds (Re) and Schmidt (Sc) numbers. $D_{CO_2,mol}$ is given by Eq. (3-17).

$$\mathrm{Sh} = \left(1 + 1.5(1-\varepsilon_b)\right)\mathrm{Sh}_P \qquad (3-23)$$

$$\mathrm{Sh}_P = 2 + 0.69(\mathrm{Re})^{1/2}(\mathrm{Sc})^{1/3} \qquad (3-24)$$

ε_b is the bed porosity, which is calculated by Eq. (3-25) [9]. The Reynolds and Schmidt numbers are calculated by Eqs. (3-26) and (3-27), respectively.

$$\varepsilon_b = 0.1504 + \frac{0.2024}{\sigma_p} + \frac{1.0814}{(\frac{d_t}{d_p} + 0.1226)^2} \qquad (3-25)$$

where d_t (m) is the diameter of the tube and d_p (m) is the diameter of the particle.

$$\mathrm{Re} = \frac{u d_P}{\upsilon} \qquad (3-26)$$

$$\mathrm{Sc} = \frac{\upsilon}{D_{CO_2,mol}} \qquad (3-27)$$

in which u (m s^{-1}) is the interstitial gas velocity and υ (m^2 s^{-1}) is the kinematic viscosity of the gas mixture.

The CO_2 equilibrium concentration $C_{CO2,eq}$ (mol m^{-3}) is calculated by Eq. (3-28). This equation is derived by combining Eqs. (3-29), (3-30), (3-31) and (3-32), which are related to the atom balance and equilibrium constant (K_P) of the RWGS reaction.

$$(K_P + 1)C_{CO_2,eq}^2 + \left(K_P C_{CO_2,in} - K_P C_{H_2,in} - C_{H_2O,in} - 2C_{CO_2,in} - C_{CO,in}\right)C_{CO2,eq}$$

$$+\left(C_{CO_2,in}\left(C_{CO,in} + C_{H_2O,in}\right) + C_{CO,in}C_{H_2O,in} + C_{CO_2,in}^2\right) = 0 \qquad (3-28)$$

Oxygen balance: $2C_{CO_2,in} + C_{CO,in} + C_{H_2O,in} = 2C_{CO_2,eq} + C_{CO,eq} + C_{H_2O,eq}$ $(3-29)$

Hydrogen balance: $C_{H_2,in} + C_{H_2O,in} = C_{H_2,eq} + C_{H_2O,eq}$ $(3-30)$

Carbon balance: $C_{CO_2,in} + C_{CO,in} = C_{CO_2,eq} + C_{CO,eq}$ $(3-31)$

$$K_P = K_C = \left(\frac{C_{CO}C_{H_2O}}{C_{CO_2}C_{H_2}}\right)_{eq} \qquad (3-32)$$

K_P is equal to K_C, which is expressed by Eq. (3-11) as a function of temperature T in K.

3.4.2. Governing differential equations of the RWGS reactor

The governing equations of the RWGS reactor consist of material, energy, and momentum balances, which are explained in the following sections.

3.4.2.1. Material balance

The material balance differential equation is represented by Eq. (3-33) [48]:

$$\frac{dF_i}{dz} = \pm r_{RWGS}\,\pi\,R_{in}{}^2\,\rho_b \qquad (3-33)$$

where dF_i (mol s^{-1}) is the change in the molar flowrate of species (CO_2, H_2, CO, and CO_2), dz (m) is the change in the length of the reactor, ρ_b (kg m^{-3}) is the bulk density, and R_{in} (m) is the inner

radius of the reactor tube. r_{RWGS} is negative for the reactants and positive for the products. r_{RWGS} is given by Eq. (3-8).

3.4.2.2. Energy balance

The energy balance of the RWGS reactor is expressed by the following equation under adiabatic conditions (validation) [48]:

$$\frac{dT}{dz} = \frac{-\sum(\Delta H_R, n)\ \rho_b r_{RWGS}}{\sum F_i C_{Pi,g}} \qquad (3-34)$$

where T (K) is the temperature of the gas phase, $C_{Pi,g}$ (J mol^{-1} K^{-1}) is the heat capacity of the species in the gas mixture, and $\Delta H_{R,n}$ (J mol^{-1}) is the heat of the RWGS reaction, which can be determined based on the equations given by Dzuryk and Rezaei [48].

3.4.2.3. Momentum balance

The pressure drop along the length of the reactor is expressed by Eq. (3-35), which is known as the Ergun equation [48]:

$$\frac{dP}{dz} = \frac{150\ \mu_g(1-\varepsilon_b)^2 v_g}{\varepsilon_b^3 d_p^2} + \frac{1.75(1-\varepsilon)\rho_g v_g^2}{\varepsilon_b^3 d_P} \qquad (3-35)$$

where dP (Pa) is the change in total pressure, d_P (m) is the diameter of the particles, μ_g (kg m^{-1} s^{-1}) is the dynamic viscosity of gas mixture, v_g (m s^{-1}) is the superficial velocity, ρ_g (kg m^{-3}) is the density of the gas mixture, and ε_b (unitless) is the bed porosity.

The details of the calculations of the physical properties (viscosity, heat capacity, and thermal conductivity) of the gas mixtures in the RWGS reactor are available in a work by Dzuryk and Rezaei [48]. The validation of the simulation of the kinetics of Ni-$Al_{12}O_{19}$ catalyst under adiabatic

conditions is presented in Appendix B. It should be noted that the RWGS reactor is simulated as an isothermal reactor in the GTL plant.

3.5. Modelling of the FT reactor

The FT reactor is an isothermal packed-bed multi-tubular reactor, which is packed with a Co-Re/Al_2O_3 catalyst. The reactor is cooled by steam production from boiler feed water. The following assumptions are made for the modelling of the FT reactor in MATLAB:

1. Steady state conditions.

2. Pseudo homogeneous (negligible liquid production in the reactor).

3. No radial mass (one-dimensional).

4. No axial mass and heat dispersion.

5. No external mass transfer limitations.

6. Ideal gas behavior.

7. No external heat transfer resistance for the catalyst particles (the temperature of the catalyst particles is equal to the temperature of the gas phase).

8. n-octane is used for the estimation of the physical properties (heat capacity, thermal conductivity, and viscosity) of C_{5+} hydrocarbons.

9. The heat of FTS reaction is -157 kJ/mol at T=200 ºC [48].

10. Inclusion of 150 normal paraffins (CH_4 to $C_{150}H_{304}$) and 149 alpha olefins (C_2H_4 to $C_{150}H_{302}$) to simulate the formation of FT hydrocarbons.

The justification of the selection of the number of alkane and alkene carbon atoms will be provided in Chapter 4. The alkane and alkene molecules with the number of carbon atoms in the range of C_1-C_{10} and C_2-C_{10} are directly selected in Aspen HYSYS. To expedite the convergence of the FT MATLAB code, alkanes and alkenes with the number of carbon atoms greater than 10 are grouped into 7 cuts, i.e., C_{11}-C_{15}, C_{16}-C_{20}, C_{21}-C_{25}, C_{26}-C_{30}, C_{31}-C_{35}, C_{36}-C_{40}, and C_{40+}. C_{11}-C_{15}, C_{16}-C_{20}, C_{21}-C_{25}, and C_{26}-C_{30} alkanes and alkenes are represented by $C_{13}H_{28}$, $C_{18}H_{38}$, $C_{23}H_{48}$, $C_{28}H_{58}$ (normal alkanes) in Aspen HYSYS. Since the database of Aspen HYSYS does not include all the required hydrocarbons with the number of carbon atoms greater than 30, three hypothetical normal alkanes are defined as $C_{33}H_{68}$, $C_{38}H_{78}$, and $C_{65}H_{132}$ for the representation of C_{31}-C_{35}, C_{36}-C_{40}, and C_{40+}, respectively. The molecular structures of the hypothetical alkanes are defined in Aspen HYSYS Hypotheticals Manager using the UNIFAC Structure Builder. The density and molecular weight of the hypothetical alkanes are manually entered using the data reported in [49]. The reason of choosing $C_{13}H_{28}$, $C_{18}H_{38}$, $C_{23}H_{48}$, $C_{28}H_{58,}$ $C_{33}H_{68}$, $C_{38}H_{78}$, and $C_{65}H_{132}$ as the representatives of the cuts is related to the product distribution of the FT reactor, which will be discussed in Chapter 4. As it will be explained in the next chapter, the molecular weight of $C_{13}H_{28}$, $C_{18}H_{38}$, $C_{23}H_{48}$, $C_{28}H_{58,}$ $C_{33}H_{68}$, $C_{38}H_{78}$, and $C_{65}H_{132}$ is close to the average molecular weight of each cut, which warrants their use as the representative of C_{11}-C_{15}, C_{16}-C_{20}, C_{21}-C_{25}, C_{26}-C_{30}, C_{31}-C_{35}, C_{36}-C_{40}, and C_{40+} cuts, respectively.

3.5.2. Kinetics of the FT reaction

The kinetics of a Re-Co/Al_2O_3 catalyst is used to simulate the LTFT reactor. The kinetic equations are based on a detailed CO-insertion mechanism to produce normal paraffins and alpha olefines. Although this mechanism is able to explain the production of oxygenates such as alcohols

and aldehydes, only the production of alkanes and alkenes are considered due to the low amount of produced oxygenates by the Re-Co/Al_2O_3 catalyst [9].

The detailed kinetic model has advantages compared to the ASF model. It can fit the experimental results better than the ASF model since the chain growth probability (α) is not considered as a constant value throughout the reactor. In addition, unlike the ASF model, the detailed kinetic model can distinguish between alkanes and alkenes with the same number of carbon atoms. In the detailed kinetic model used in this thesis, a distinct chain growth probability is defined as a function of pressure, temperature, and fraction of vacant sites (S) for each hydrocarbon molecule (n), which are given by Eqs. (3-36) to (3-39).

$$\alpha_1 = \frac{k_3 K_1 P_{CO}[S]}{k_3 K_1 P_{CO} + k_{7M}\sqrt{K_2 P_{H_2}}} \quad n = 1 \qquad (3-36)$$

$$\alpha_2 = \frac{k_3 K_1 P_{CO}[S]}{k_3 K_1 P_{CO} + k_{8,E} e^{c.2} + [S] k_{7M}\sqrt{K_2 P_{H_2}}} \quad n = 2 \qquad (3-37)$$

$$\alpha_n = \frac{k_3 K_1 P_{CO}[S]}{k_3 K_1 P_{CO} + k_{8,E} e^{c.n} + [S] k_{7M}\sqrt{K_2 P_{H_2}}} \quad n \geq 3 \qquad (3-38)$$

$$S = \frac{1}{\left\{1 + K_1 P_{CO} + \sqrt{K_2 P_{H_2}} + \left(\frac{1}{K_6 K_4 K_5 K_2^2}\frac{P_{H_2O}}{P_{H_2}} + \sqrt{K_2 P_{H_2}}\right).\left(\alpha_1 + \alpha_1\alpha_2 + \alpha_1\alpha_2 \sum_{i=3}^{n}\prod_{j=3}^{i}\alpha_j\right)\right\}} \qquad (3-39)$$

The function fsolve is used in MTLAB to simultaneously solve Eqs. (3-36) to (3-39) to find the values of S and α_n for any given number of carbon atoms.

The reaction rates used in the simulation of the LTFT reactor are presented by Eqs. (3-40) to (3-46).

Carbon monoxide consumption rate is expressed by [50]:

$$-r_{CO} = \frac{k_{CO} P_{CO} P_{H_2}}{(1 + a P_{CO})^2} \qquad (3-40)$$

$$k_{CO} = 1.52 \times 10^{8} e^{\frac{72.69\times10^{3}}{8.314\times T}} \qquad a = 0.645 e^{\frac{10.77\times10^{3}}{8.314\times T}} \qquad (3-41)$$

The rate of water formation is equal to the consumption rate of CO, i.e, $r_{H_2O} = r_{CO}$.

The rate of methane formation (r_{CH_4}) is given by Eqs. (3-42) and (3-43) [9,51]:

$$r_{CH_4} = \frac{k_{CH_4} P_{CO}^{-0.99} P_{H_2}^{1.28}}{(1 + 0.58 \frac{P_{H_2O}}{P_{H_2}})} \qquad (3-42)$$

$$k_{CH_4} = 1.57 \times 10^{12} e^{\frac{139.98\times10^{3}}{8.314\times T}} \qquad (3-43)$$

The rate of alkanes formation (except CH_4) is given by [9]:

$$r_{C_nH_{2n+2}} = k_7 K_2^{0.5} P_{H_2}^{0.5} \alpha_1 \alpha_2 \prod_{i=3}^{n} \alpha_i [S]^2 \qquad n > 1 \qquad (3-44)$$

The rate of the formation of ethylene and other alkenes is given by Eqs. (3-45) and (3- 46), respectively [9]:

$$r_{C_2H_4} = k_{8E} e^{c.2} \alpha_1 \alpha_2 [S] \qquad (3-45)$$

$$r_{C_nH_{2n}} = k_8 e^{c.n} \alpha_1 \alpha_2 \prod_{i=3}^{n} \alpha_i [S] \qquad n > 2 \qquad (3-46)$$

In all reaction rates, r is the reaction rate (mol kg_{cat}^{-1} s^{-1}), P_{CO} (MPa) is the partial pressure of CO, P_{H_2} (MPa) is the partial pressure of H_2, P_{H_2O} (MPa) is the partial pressure of H_2O, T is temperature in K, K_i (unit depends on the frequency factor) is the equilibrium constant given by Eq. (3-47), k_i (unit depends on the frequency factor) is reaction rate constant given by Eq. (3-48), and c (dimensionless) in Eqs. (3-45) and (3-46) is calculated by Eq. (4-49). The required data related to the activation energy E, pre-exponential factor k_o or K_o, and ΔH in Eqs. (3-36) to (3-46) are presented in Table 3.5.

$$k_i = k_{o,i} \exp\left(\frac{-E_i}{RT}\right) \quad i = 3, 7, 8, 7, 7M, 8, \text{and } 8E \qquad (3-47)$$

$$K_i = K_{o,i} \exp\left(\frac{-\Delta H_i}{RT}\right) \quad i = 1, 2, 4, 5, \text{and } 6 \qquad (3-48)$$

$$c = \frac{-\Delta E}{RT} \qquad (3-49)$$

Table 3.5. Kinetic parameters of the Re-Co/Al_2O_3 catalyst [52]

Eq. No.	Parameter	Value	Unit	Parameter	Value	Unit
(3-47)	$\mathbf{K_{o,1}}$	6.59×10^{-5}	Mpa^{-1}	$\mathbf{\Delta H_1}$	-48.9	kJ mol^{-1}
(3-47)	$\mathbf{K_{o,2}}$	1.64×10^{-4}	MPa^{-1}	$\mathbf{\Delta H_2}$	-9.4	kJ mol^{-1}
(3-46)	$\mathbf{k_{o,3}}$	4.14×10^{8}	mol g_{cat}^{-1} h^{-1}	$\mathbf{E_3}$	92.8	kJ mol^{-1}
(3-47)	$\mathbf{K_{o,4}}$	3.59×10^{5}	-	$\mathbf{\Delta H_4}$	16.2	kJ mol^{-1}
(3-47)	$\mathbf{K_{o,5}}$	9.81×10^{-2}	-	$\mathbf{\Delta H_5}$	11.9	kJ mol^{-1}
(3-47)	$\mathbf{K_{o,6}}$	1.59×10^{6}	MPa	$\mathbf{\Delta H_6}$	14.5	kJ mol^{-1}
(3-46)	$\mathbf{k_{o,7}}$	4.53×10^{7}	mol g_{cat}^{-1} h^{-1}	$\mathbf{E_7}$	75.5	kJ mol^{-1}
(3-46)	$\mathbf{k_{o,8}}$	4.11×10^{8}	mol g_{cat}^{-1} h^{-1}	$\mathbf{E_8}$	100.4	kJ mol^{-1}
(3-46)	$\mathbf{k_{o,7M}}$	7.35×10^{7}	mol g_{cat}^{-1} h^{-1}	$\mathbf{E_{7M}}$	65.4	kJ mol^{-1}
(3-46)	$\mathbf{k_{o,8E}}$	4.60×10^{7}	mol g_{cat}^{-1} h^{-1}	$\mathbf{E_{8E}}$	103.2	kJ mol^{-1}
(3-48)	**ΔE**	1.1	kJ $mol^{-1}CH_2^{-1}$			

As mentioned earlier, C_{11}-C_{15}, C_{16}-C_{20}, C_{21}-C_{25}, C_{26}-C_{30}, C_{31}-C_{35}, C_{36}-C_{40}, and C_{40+} are represented by $C_{13}H_{28}$, $C_{18}H_{38}$, $C_{23}H_{48}$, $C_{28}H_{58}$, $C_{33}H_{68}$, $C_{38}H_{78}$, and $C_{65}H_{132}$, respectively. The production rate of these representative hydrocarbons is given by the following equations:

$$r_{C_{13}H_{28}} = \sum_{11}^{15} \left(r_{C_nH_{2n+2}} + r_{C_nH_{2n}}\right) \qquad (3-50)$$

$$r_{C_{18}H_{38}} = \sum_{16}^{20} (r_{C_nH_{2n+2}} + r_{C_nH_{2n}}) \quad (3-51)$$

$$r_{C_{23}H_{48}} = \sum_{21}^{25} (r_{C_nH_{2n+2}} + r_{C_nH_{2n}}) \quad (3-52)$$

$$r_{C_{28}H_{58}} = \sum_{26}^{30} (r_{C_nH_{2n+2}} + r_{C_nH_{2n}}) \quad (3-53)$$

$$r_{C_{33}H_{68}} = \sum_{31}^{35} (r_{C_nH_{2n+2}} + r_{C_nH_{2n}}) \quad (3-54)$$

$$r_{C_{38}H_{78}} = \sum_{36}^{40} (r_{C_nH_{2n+2}} + r_{C_nH_{2n}}) \quad (3-55)$$

$$r_{C_{65}H_{132}} = \sum_{41}^{150} (r_{C_nH_{2n+2}} + r_{C_nH_{2n}}) \quad (3-56)$$

Finally, the hydrogen consumption rate can be determined based on the consumption rate of CO and H_2 using Eqs. (3-57) to (3-60) [53]:

$$r_{H_2} = UR \times r_{CO} \quad (3-57)$$

$$UR = \frac{(-r_{H_2})^{prod}}{(-r_{CO})^{prod}} \quad (3-58)$$

$$(r_{CO})^{prod} = r_{CH_4} + \sum_{2}^{150} n \times (r_{C_nH_{2n+2}} + r_{C_nH_{2n}}) \quad (3-59)$$

$$(r_{H_2})^{prod} = 3 \times r_{CH_4} + \sum_{2}^{150} [(2n+1) \times r_{C_nH_{2n+2}} + 2n \times r_{C_nH_{2n}}] \quad (3-60)$$

UR is the usage ratio of H_2 to CO. $(r_{H_2})^{prod}$ and $(r_{CO})^{prod}$ are the rate of consumption of H_2 and CO, respectively, which are calculated from the production rate of hydrocarbons.

3.5.3. Governing differential equations of the FT reactor

The material, energy, and momentum balance differential equations of the FT reactor are provided in Sections 3.5.3.1 to 3.5.3.3.

3.5.3.1. Material balance

The material balance differential equation is expressed by Eq. (3-61) [9].

$$\frac{dF_i}{dz} = \pm A_{cs}\eta\rho_b r_i \qquad (3-61)$$

where dF_i (mol s^{-1}) is the change in molar flow rate of reactants (CO, H_2) and products (alkanes, alkenes, and water), dz (m) is the change in the length of the reactor, A_{CS} (m^2) is the tube-cross section area, η (unitless) is the catalyst effectiveness factor, ρ_b(kg m^{-3}) is the catalyst bulk density, and r_i (mol kg^{-1} s^{-1}) is the rate of disappearance or formation of components. r_i is negative for the reactants and positive for the products.

The catalyst effectiveness factor, calculated by Eqs. (3-62) and (3-63), indicates the intraparticle mass transfer resistance due to the presence of the liquid phase (heavy hydrocarbons or wax) in the catalyst pores. Based on the investigation by Mandic et al. [53], there is a linear relationship between the effectiveness factor (η) and the natural logarithm of the Thiele modulus, i.e., ln(φ). This relationship holds when the diameter of the catalyst particle is higher than 1 mm.

$$\eta = 0.9939 - 0.469.\ln(\varphi) \qquad (3-62)$$

$$\varphi = \frac{d_p}{6}\sqrt{\frac{\rho_P.(-r_{CO})}{D_{e,CO}.C_{CO,s}}} \qquad (3-63)$$

$C_{CO,s}$ (mol m^{-3}) is the concentration of CO in the liquid phase on the surface of the catalyst and can be calculated by the Henry's law expressed by Eq. (3-64), r_{CO} ($mol\ kg_{cat}^{-1}\ s^{-1}$) is the rate of CO disappearance at the catalyst surface, $D_{e,CO}$ ($m^2\ s^{-1}$) is the effective intraparticle diffusivity of CO in the liquid phase given by Eq. (3-68), ρ_p (kg m^{-3}) is the density of catalyst particles, and d_p (m) is the diameter of catalyst particles. The characteristics of the Re-Co/Al_2O_3 catalyst are given in Table 3.6.

$$C_{CO,s} = P_{CO}\frac{C_{wax}}{H_{CO}} \qquad (3-64)$$

where P_{CO} (Pa) is the partial pressure of CO and H_{CO} (Pa m^3 mol^{-1}) is the Henry's constant determined by Eqs (3-65) and (3-66) [53,54].

$$H_{CO} = \frac{\exp\left(H_{CO,0} - 28\Delta H_{CO}\right)}{10^5}, \qquad \Delta H_{CO} = 0.0173238 \qquad (3-65)$$

$$H_{CO,0} = 5.79833 + \frac{19.5937}{T} + 0.152199\ln T + 1.89733\times 10^{-6}T^2 + \frac{E2031.63}{T^2} \qquad (3-66)$$

C_{wax} (mol m^{-3}) is the concentration of wax, which can be calculated by Eq. (3-67) based on the density and molecular weight of the liquid phase. n-octacosane ($C_{28}H_{58}$) is used in this work as the representative of heavy hydrocarbons in the catalyst pores for the calculation of C_{wax}.

$$C_{wax} = \frac{\rho_{wax}}{M_{wax}} \qquad (3-67)$$

$$D_{e,CO} = D_{wax,CO}\frac{\varepsilon_p}{\tau_p} \qquad (3-68)$$

The values of the catalyst particle porosity ε_p (unitless) and tortuosity τ_b (unitless) are given in Table 3.6. $D_{wax,\,CO}$ ($m^2\ s^{-1}$) is the diffusivity coefficient of CO in the wax, which is determined by the Akgerman's correlation [52]:

$$D_{wax,CO} = \frac{94.5 \times 10^{-9}\sqrt{T}}{M_{CO}^{0.239} M_{wax}^{0.781} (\sigma_{CO}\sigma_{wax})^{1.134}} (V_b - bV_0) \qquad (3-69)$$

$$b = 1.206 + 0.0632\left(\frac{\sigma_{CO}}{\sigma_{wax}}\right) \qquad (3-70)$$

in which M_{CO} is the molecular weight of CO (28.01 g mol^{-1}), M_{wax} is the molecular weight of wax which is assumed to be 394.77 g mol^{-1} (the molecular weight of n-octacosane), σ_{CO} and σ_{wax} are the molecular diameter of CO and wax, which equal to 3.72 A° and 9.76 A°, respectively. V_b and V_0 ($cm^3\ mol^{-1}$) are the wax molar volume and wax close-packed hard sphere volume, which are given by Eqs. (3-71) and (3-72), respectively [52].

$$V_b = \frac{M_{wax}}{\rho_{wax}} \qquad (3-71)$$

$$V_0 = \frac{6.022 \times 10^{23} (\sigma_{wax} \times 10^{-8})^3}{\sqrt{2}} \qquad (3-72)$$

Table 3.6. Characteristics of the Re-Co/Al_2O_3 catalyst [52]

Parameter	Unit	Value
Porosity of catalyst (ε_P)	-	0.5
Tortuosity of particle (τ_P)	-	2
Catalyst particle diameter (d_P)	m	0.002
Catalyst particle density (ρ_P)	kg m^{-3}	1200
Geometry (spherical)	-	-

3.5.3.2. Energy balance

The energy balance differential equation of the FT reactor is expressed by Eq. (3-73):

$$\nu_g \rho_g c_{p,g} \frac{dT}{dz} = (-\Delta H_r)\eta\rho_b(-r_{CO}) - \frac{4U}{d_t}(T - T_{wall}) \qquad (3-73)$$

in which dT (K) is the change in the temperature, ν_g (m s^{-1}) is the superficial gas velocity, ρ_g (kg m^{-3}) is the density of gas mixture, c_p (J kg^{-1} K^{-1}) is the heat capacity of gas mixture, ΔH_r (kJ mol^{-1}) is the reaction heat, which is equal to -157 (kJ mol CO^{-1}) at 200 °C [52], U (W m^{-2} K^{-1}) is the overall heat transfer coefficient, d_t (m) is the tube diameter, and T_{wall} (K) is the reactor wall temperature fixed at 200 °C, and ρ_b (kg m^{-3}) is the catalyst bulk density, which is calculated based on Eqs. (3-25) and (3-74).

$$\rho_b = (1 - \varepsilon_b)\rho_p \qquad (3-74)$$

The overall heat transfer coefficient (U) is given by Eq. (3-75) [52]:

$$\frac{1}{U} = \frac{1}{h_{wall}} + \frac{d_t}{8\lambda_{er}} \quad (3-75)$$

h_{wall} (W m^{-2} K^{-1}) and λ_{er} (W m^{-1} K^{-1}) are the radial heat transfer coefficient at the wall and effective radial thermal conductivity, respectively. The radial heat transfer coefficient in a two-phase packed-bed reactor is dependent on liquid and gas flow rates. Under the FTS condition with low liquid flow rates ($0 < Re_l < 2$), h_{wall} is dominated by the gas velocity and is given by [52]:

$$h_{wall} = h_{wall,o} + h_{wall,g} \quad (3-76)$$

in which $h_{wall,o}$ (W m^{-2} K^{-1}) and $h_{wall,g}$ (W m^{-2} K^{-1}) are the stagnant and convective contributions, respectively, which are expressed by Eqs. (3-77) and (3-78) [52]:

$$h_{wall,g} = \frac{\lambda_g}{d_p} 0.0835 Re_g^{0.91} \quad (3-77)$$

$$h_{wall,o} = \frac{\lambda_g}{d_p}\left(2\varepsilon_b + \frac{1-\varepsilon_b}{\frac{\lambda_g}{\lambda_s}\varepsilon_w + \phi_w}\right) \quad (3-78)$$

where ε_w is equals to1/3 and ϕ_w is calculated by Eq (3-79) for spherical particles. λ_g (W m^{-1} K^{-1}) is the gas phase thermal conductivity, d_p (m) is the diameter of the catalyst particles, ε_b (unitless) is the bed porosity, and λ_s is the thermal conductivity of the catalyst particles with a value of 12.4 W m^{-1} K^{-1}, i.e., the thermal conductivity of alumina [52].

$$\phi_w = 0.00240\left(\frac{d_t}{d_p}\right)^{1.58} \quad (3-79)$$

where d_t (m) is the diameter of the tube.

The effective radial thermal conductivity (λ_{er}) is expressed by [52]:

$$\lambda_{er} = \lambda_{er}^{s} + \lambda_{er}^{g} + \lambda_{er}^{l} \quad (3-80)$$

λ_{er}^{s} is the static heat transfer by conduction and diffusion in the packed-bed reactor. λ_{er}^{g} and λ_{er}^{l} are the contributions of the gas and liquid phases, respectively. Since the heat transfer rate by diffusion is much lower than that of the conduction, λ_{er}^{s} is estimated based on the thermal conductivity of the liquid phase by:

$$\lambda_{er}^{s} = 1.5\lambda_{l} \quad (3-81)$$

λ_{er}^{g} and λ_{er}^{l} are functions of the Reynolds and Prantl numbers and are expressed by the following equations [52]:

$$\lambda_{er}^{g} + \lambda_{er}^{l} = (\alpha\beta)_{g}\lambda_{g}Re_{g}Pr_{g} + (\alpha\beta)_{l}\lambda_{l}Re_{l}Pr_{l} \quad (3-82)$$

$$(\alpha\beta)_{l} = a_{gl}\left(1 + b_{gl}.\,Re_{g}\right) \quad (3-83)$$

$$(\alpha\beta)_{g} = 9.6 \times 10^{3}.\,d_{p}^{2} - 92.3.\,d_{p} + 0.51 \quad (3-84)$$

$$a_{gl} = 5 \times 10^{3}.\,d_{p}^{2} - 43.2.\,d_{p} + 0.25 \quad (3-85)$$

$$b_{gl} = 2.1 \times 10^{3}.\,d_{p}^{2} - 18.6.\,d_{p} + 0.05 \quad (3-86)$$

$$Re_{g} = \frac{\rho_{g}u_{s,g}d_{p}}{\mu_{g}} \quad (3-87)$$

$$Re_{l} = \frac{\rho_{l}u_{s,l}d_{p}}{\mu_{l}} \quad (3-88)$$

$$Pr_{l} = \frac{C_{p,l}\mu_{l}}{\lambda_{l}} \quad (3-89)$$

$$Pr_{g} = \frac{C_{p,g}\mu_{g}}{\lambda_{g}} \quad (3-90)$$

$$u_{s,g} = \frac{F_g M_{g,ave}}{\rho_g A_{CS}} \quad (3-91)$$

$$u_{s,l} = \frac{F_l M_l}{\rho_l A_{CS}} \quad (3-92)$$

where $M_{g,ave}$ (g mol^{-1}) is the average molecular weight of the gas phase, $C_{p,g}$ (J kg^{-1} K^{-1}) is the heat capacity of gas phase, μ_g (Pa s) is the gas mixture viscosity, ρ_g (kg m^{-3}) is the gas mixture density, λ_g (W m^{-1} K^{-1}) is the thermal conductivity of the gas mixture, F_g (mol s^{-1}) is the molar flowrate of the gas phase, M_l (g mol^{-1}) is the molecular weight of the liquid phase, $C_{p,l}$ (J kg^{-1} K^{-1}) is the heat capacity of liquid phase, μ_l (Pa s) is the liquid viscosity, λ_l (W m^{-1} K^{-1}) is the thermal conductivity of the liquid, and F_l (mol s^{-1}) is the molar flowrate of liquid phase, which is assumed to be 1% of the molar flow rate of the gas mixture in the reactor [53]. It should be noted that $C_{20}H_{42}$ is used in the above equations to estimate the viscosity (μ_l), density (ρ_l), heat capacity ($C_{p,l}$), and thermal conductivity (λ_l) of the liquid phase. Correlations given in the NIST database of Aspen Plus are used to estimate the physical properties of $C_{20}H_{42}$.

3.5.3.3. Momentum balance

The momentum balance equation is based on the Ergun equation, given by Eq. (3-34) in the RWGS section.

The equations to calculate physical properties of gas mixtures (average molecular weight, thermal conductivity, viscosity, density, and heat capacity) in the FT reactor are available in a PhD thesis by Todic and a study by Dzuryk and Rezaei [9,48]. The validation of the kinetics of the Re-Co/Al_2O_3 catalyst is presented in Appendix A.

3.6. Utilities

3.6.1. Steam

Since the FTS is a highly exothermic reaction, the generated heat should be removed to avoid any temperature runaway. In this work, medium pressure steam at 200 °C and 1555 kPa is generated in the FT reactor, which is used to provide steam requirements of the plant and produce electricity. No other levels of steam are produced in the plant.

3.6.2. Cooling water

The cooling water CW at 30 °C and 200 kPa is used for cooling purposes. The outlet temperature of the cooling water is kept at 40 °C.

3.6.3. Compressor polytropic efficiency

The polytropic efficiency of compressors is determined by Eq. (3-93) [56]:

$$\eta_P = 0.017 \ln V^{\circ} + 0.7 \qquad (3-93)$$

in which η_P is the polytropic efficiency, and V° ($m^3\ s^{-1}$) is the inlet volumetric flowrate of gas.

3.6.4. Turbine and gas expander efficiencies

3.6.4.1. Steam turbines

The efficiency of steam turbines is calculated by Eq. (3-94) [56]:

$$\eta_{ST,max} = \frac{1}{a}\left(1 - \frac{b}{m_{max}\Delta H_{IS}}\right) \qquad (3-94)$$

in which $\eta_{ST,max}$ is the efficiency of the steam turbine at maximum load, a and b are the modelling coefficients, m_{max} (kg s^{-1}) is the mass flowrate of the steam at maximum load, ΔH_{IS} (kJ kg^{-1}) is the enthalpy change of the steam when the turbine works with an isentropic efficiency of 100%. ΔH_{IS} is calculated in Aspen HYSYS by simulating steam turbines with 100% isentropic efficiency.

The values of a and b are calculated by Eqs. (3-95) and (3-96), respectively.

$$a = a_1 + a_2 P_{in} + a_3 P_{out} \quad (3-95)$$

$$b = b_1 + b_2 P_{in} + b_3 P_{out} \quad (3-96)$$

where P_{in} (bar) and P_{out} (bar) are the inlet and outlet pressures of steam, respectively. The coefficients of Eqs. (3-95) and (3-96) are given in Table 3.7. The pressure of steam at the outlet of the turbines is kept at 40 kPa with a vapor fraction of 0.91.

Table 3.7 Coefficients of steam turbines to be used in Eq. (3-95) and (3-96)

Steam Turbine Modeling Coefficients	Back-Pressure Turbine
a_1	1.88
a_2	-2.96×10^{-4}
a_3	4.65×10^{-3}
b_1	449.98
b_2	5.6702
b_3	-11.505

3.6.4.2. Gas expanders

To calculate the efficiency of the gas expanders, Eq. (3-97) is applied [57]:

$$x_{dr}(\%) = 75 + 11.5\log(W_s) - 1.5(\log(W_s))^2 \qquad (3-97)$$

where x_{dr} is the drive efficiency and W_s (kW) is the shaft power. The following trial and error procedure is used to determine the isentropic efficiency of gas expanders. First, the shaft power of a gas expander working with 75% isentropic efficiency is obtained in Aspen HYSYS. Then the shaft power is used in Eq. (3-97) to calculate a new drive efficiency, which is then input in Aspen HYSYS as the new value of the isentropic efficiency of the gas expander to obtain a new shaft power to be used in Eq. (3-97). The process is repeated until the isentropic efficiency of the gas expander converges.

3.6.5. Furnace, pump, electric drive efficiencies

In this thesis, the purge gases of the FT synthesis loop are burnt in a furnace, which is simulated as a conversion reactor to completely convert its fuel (hydrocarbons, H_2, and CO) to CO_2 and water vapour in the presence of 3% excess air. It is assumed that the thermal efficiency of the furnace is 95%. The efficiency of pumps is assumed to be 75% (the default adiabatic efficiency in HYSYS). The drive efficiency (conversion of electricity to shaft power for compressors and pumps and conversion of shaft power to electricity for turbines) of the compressors, turbines, and pumps is assumed to be 97% with a mechanical efficiency of 100%.

Chapter 4: Process description and economic and environmental evaluation of the gas-to-liquid plant

This chapter first presents the process flow diagram (PFD) of the GTL plant including hydrogen production by the MDR, syngas production by the RWGS reaction, syncrude manufacturing by the FTS, and energy recovery unit in Sections 4.1.1 to 4.1.4. The performance of the MDR, RWGS, and FT unit is explained in more details in Sections 4.2, 4.3, and 4.4, respectively. The energy balance of the plant including the steam, electricity, and thermal energy is explained in Section 4.5. The economic and environmental analysis of the plant are presented in Section 4.6.

4.1. Process flow diagram

The GTL plant consists of four main units: (1) hydrogen production by the MDR, (2) syngas production by the RWGS reaction, (3) syncrude manufacturing by the FTS, and (4) steam loop and energy recovery for electricity generation. The process flow diagram of each unit is explained in detail in Sections 4.1.1 to 4.1.4. In the process flow diagrams, streams associated with steam or condensed steam, furnace flue gas, furnace combustion air, produced solid carbon, cooling water, produced process water, syncrude, and the plant purge gases are denoted by S, Fg, A, SC, CW, W, Syn, and P, respectively. All stream specifications including the flow rate, temperature, pressure, and composition of streams are reported in Appendix D. The specifications of the shell-and-tube heat exchangers (except those involving the produced solid carbon and the furnace flue gas) are given in Appendix E.

4.1.1. Hydrogen production by the MDR

As shown in Fig. 4.1, the feed natural gas with a mass flow rate of 4.280×10^5 kg h^{-1} (MW=18.17) at 5 °C and 8000 kPa is first depressurized by a gas expander (EX-1) to 1928 kPa. The depressurized natural gas is then preheated to 800 ºC by two heat exchangers (E-1 and E-2) before entering the MDR, which is an isothermal reactor at 1100 ºC with inlet and outlet pressures of 1900 and 1844 kPa, respectively. E-1 heats up the natural gas from -74 ºC to -3 ºC by cooling a gas stream (stream 53 in Fig. 4.3) of a three-phase separator in the FT unit (V-5 in Fig. 4.3). E-2 is a feed-to-effluent heat exchanger, which increases the natural gas temperature from -3 ºC to 800 ºC by cooling the H_2-rich gas product stream (H_2:0.8921, CH_4:0.0933, and N_2: 0.0043) of the MDR from 1100 ºC to 367 ºC. The H_2-rich stream is further cooled down to 48 ºC by exchanging heat with stream 58 (the recycle stream of the FT reactor in Fig. 4.3) in E-3 and then compressed by a compressor (COM-1) to 3390 kPa. The compressed H_2-rich stream is then cooled down to 40 ºC by CW before it enters a pressure swing adsorption (PSA) unit at 3381 kPa for H_2 separation. The unreacted methane and nitrogen are separated from hydrogen and leave the PSA unit at 39 °C and 101 kPa (stream P-1). The PSA purge stream is then compressed to 120 kPa by a compressor (COM-2) to be burnt in a furnace (F-1), shown in Fig 4.1, to produce heat. The purified hydrogen at 40 °C and 3361 kPa with the mole faction of H_2: 0.9997 and N_2: 0.0003 is split in two streams. The first split of the purified H_2 stream of the PSA unit (stream 13(a)) is mixed with depressurized feed CO_2 with a mass flow rate of 5.390×10^5 kg h^{-1} at -1 ºC and 3361 kPa (stream 15). The mixed H_2/CO_2 stream (stream 16 at -51 ºC and 3361 kPa) is heated in E-5 to 30 ºC by stream 52(a) from V-5 in the FT unit (Fig. 4.3). The mixed H_2 and CO_2 stream has an H_2/CO_2 ratio of 3, which enters the RWGS unit for syngas production shown Fig. 4.2. The second split of the purified H_2 stream of the PSA unit (stream 13(b)) is mixed with the produced syngas of the RWGS unit (Fig. 4.2) to

adjust its H_2/CO ratio to 2.1 to be used as the feed in the FT unit. The produced carbon of the MDR at 1100 ºC and 1844 kPa with a mass flow rate of 2.549×10^5 kg h^{-1} (stream SC-1) is used in several Solex heat exchangers to heat various process streams and to produce steam for electricity generation [60].

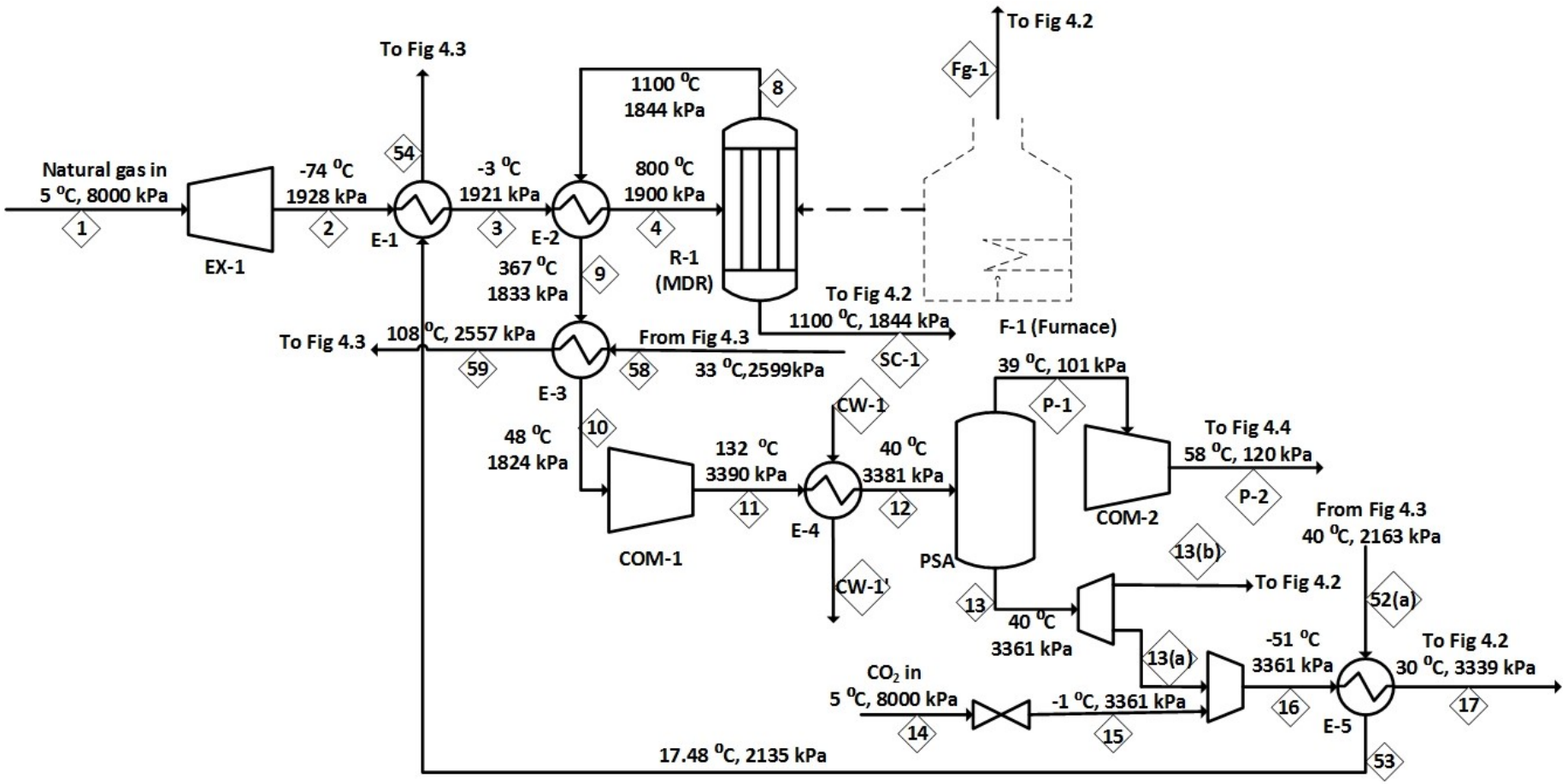

Fig. 4.1. Process flow diagram of hydrogen production by the MDR

4.1.2. Syngas production by the RWGS reaction

The PFD of the RWGS unit is shown in Fig. 4.2. The H_2 and CO_2 mixed stream from the MDR unit at 30 ºC and 3339 kPa (stream No. 17 in Figs. 4.1 and 4.2) is heated to 156 ºC by the produced solid carbon (stream SC-1) in E-13 and then mixed with the recycle stream of the RWGS reactor (stream 43 with CO_2:0.9266, H_2O: 0.0488, H_2: 0.0171, CO: 0.0074), which is already compressed in a compression train (COM-3 to COM-5) to 3319 kPa at 156 ºC. The resulting mixed stream (stream 19) enters the feed-to-effluent heat exchanger (E-8) of the RWGS to increase its temperature to 870 ºC. The heated stream (steam 20) is then directed to the furnace (F-1) to increase its temperature to 1023 ºC before entering the RWGS reactor at 3303 kPa. The RWGS reactor is an isothermal multi-tubular reactor heated by the furnace (F-1). The product stream of the reactor (stream 21) leaves the reactor at 1023 °C and 3242 kPa with mole fraction of H_2: 0.4791, CO: 0.23, H_2O: 0.2302, CO_2: 0.0605, and N_2:0.0002. The RWGS reactor product stream is first cooled down in E-8 to 285 ºC and then in E-9 to 154 ºC by heating up stream 59 from 108 °C to 163 °C (the recycle stream of the FT reactor in Fig. 4.3). The temperature of the RWGS outlet gas stream is further reduced in E-11 to 145 ºC by heating up the syngas (stream 27) exiting a monoethanolamine (MEA) absorption column (T-1). The product stream is finally cooled to 51 ºC to be introduced to a flash tank (V-3) to separate its condensed water (stream W-3). The gas stream of V-3 (stream 26) with a high CO_2 content (7.8 mol%) enters the bottom of the MEA absorption column at 3200 kPa to separate the CO_2 content of the syngas by MEA. The syngas with a composition of H_2: 0.6684, CO: 0.3208, H_2O:0.0043, CO_2: 0.0062, and N_2: 0.0003 leaves the top of the MEA absorption column at 3000 kPa and 50 ºC with an H_2/CO ratio of 2.08. The bottom stream of the MEA absorption column (rich MEA) at 62 ºC and 3200 kPa is preheated in E-16 to 96 ºC and then throttled to 200 kPa to be introduced to a full reflux distillation column (MEA regenerator) for the regeneration of MEA by desorbing CO_2. The feed tray of the MEA regenerator

is tray No. 1 (from the top of the column). The overhead stream of the MEA regenerator (stream 31) is compressed by the RWGS reactor's recycle compression train and recycled back to the reactor. The bottom stream (lean MEA) of the MEA regenerator (stream 32), leaves the column at 113 ºC and 210 kPa. It is cooled down to 81 ºC in E-16 before mixing with the make-up water. The pressure of the lean MEA stream is then increased by a pump (P-1) to 3025 kPa and its temperature is reduced to 50 ºC by CW in E-17 before entering the top of MEA absorption column for CO_2 absorption. The produced syngas stream of the MEA absorption column (stream 27) is heated in E-11 and E-14 to 200 ºC by exchanging heat with the outlet of the RWGS reactor (stream 23) and produced solid carbon (stream SC-2), respectively. Its pressure is then reduced from 2973 kPa to 2500 kPa using a valve. The syngas at 200 ºC and 2500 with an H_2/CO of 2.08 is mixed with the second split of the purified H_2 stream of the PSA unit (stream 13(d)), which is already heated to 200 ºC by exchanging heat with the produce carbon (stream SC-3) in E-15. The resulting syngas (stream ToFT) has an H_2/CO ratio of 2.1, which is mixed with the recycle stream of the FT reactor for the synthesis of syncrude.

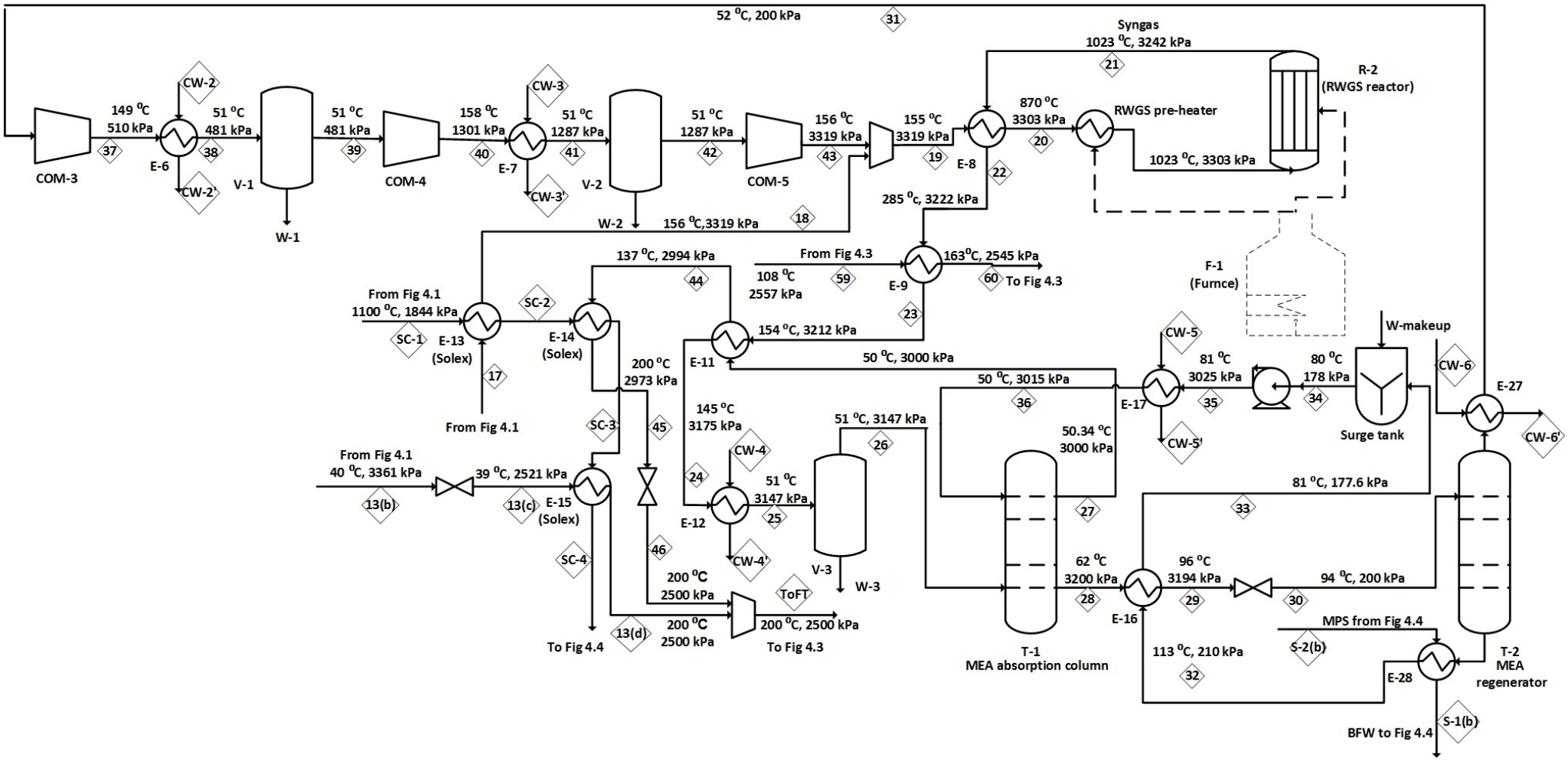

Fig. 4.2. Process flow diagram of syngas production by the RWGS reaction

4.1.3. Syncrude manufacturing by the FTS

The PFD of the FT unit is shown in Fig. 4.3. The syngas from the RWGS unit with an H_2/CO ratio of 2.1 (stream ToFT in Figs. 4.2 and 4.3) is mixed with recycled stream of the FT synthesis loop (stream 61 with an H_2/CO ratio of 1.95) to enter the FT reactor at 200 °C and 2500 kPa with an H_2/CO ratio of 2 (stream 47). The temperature of the FT reactor is maintained close to 200 ºC by producing steam in its shell at 200 °C and 1555 kPa. The produced steam is used to provide the reboiler duty of the MEA regenerator column in Fig. 4.2 and produce electricity in Fig. 4.4. The product stream of the FT reactor (stream 48) at 203 ºC and 2222 kPa is sent to a high temperature two-phase separator (V-4) to separate the FT reactor wax (stream 49(b)), which mainly consists of C_{16} plus. The gases from V-4 are cooled in E-18 and E-19 to 40 ºC by exchanging heat with the furnace combustion air (stream A-1) and CW, respectively. The cooled stream (stream 51) enters a three-phase separator (V-5) and heavy hydrocarbons (stream 52(b) having C_9 to C_{23} hydrocarbons) are separated from water (steam W-4) and light gaseous hydrocarbons and syngas (stream 52(a)). The gas stream from V-5 is cooled to 5 ºC in E-5 and E-1 by exchanging heat with the mixed H_2 and feed CO_2 stream (stream 16 in Fig. 4.1) and expanded feed natural gas (stream 2 in Fig. 4.1), respectively. The cooled stream at 5 ºC and 2095 kPa (stream 54) is sent to a second three-phase separator (V-6) to separate condensed hydrocarbons (stream 55(b) having C_3 to C_8 hydrocarbons) from water (stream W-5) and remaining light hydrocarbons and syngas (stream 55(a)). The condensed hydrocarbons of V-5 and V-6 (streams 52(b) and 55(b)) are mixed with the reactor wax (stream 49(b)) to produce 30000 bbl/day of syncrude with a mass flow rate of 1.598×10^5 kg h^{-1} (MW=246.9) at 149 ºC and 2095 kPa (stream Syn-1). The syncrude is cooled down to 40 ºC in E-20 by heating up the recycle stream of the FT synthesis loop (stream 57). 99% of the gas stream of V-6 (stream 55(a)) is recycled back to the FT reactor as stream 56. The

recycled stream is first pressurized to 2651 kPa by a compressor (COM-6) and then heated to 33 ºC in E-20 by exchanging heat with the produced syncrude. The FT recycle stream at 33 ºC (stream 58) is further heated up to 200 ºC in E-3, E-9, and E-10 by exchanging heat with product gas stream of the MDR (stream 9 in Fig. 4.1), product gas stream of the RWGS reactor (stream 22 in Fig. 4.2), and flue gas (stream Fg-1 in Fig. 4.3), respectively. The FT recycle stream at 200 ºC and 2545 kPa (stream No. 61) mixes with the syngas coming from the RWGS unit (stream ToFT). The purge of the FT synthesis loop (stream P-3) is depressurized to 120 kPa and mixes with the purge of the PSA unit (stream P-2) to be burnt as fuel in the furnace (F-1). A blower (COM-7) supplies the combustion air of the furnace, which is first pre-heated to 137 ºC (stream A-2) in E-18 and then enters the furnace at 120 kPa and 195 ºC (stream A-3). The furnace provides the duty of the RWGS pre-heater, RWGS reactor, and MDR. The flue gas of the furnace (stream Fg-1) is used to heat up process streams and produce steam for electricity generation as explained in the next section.

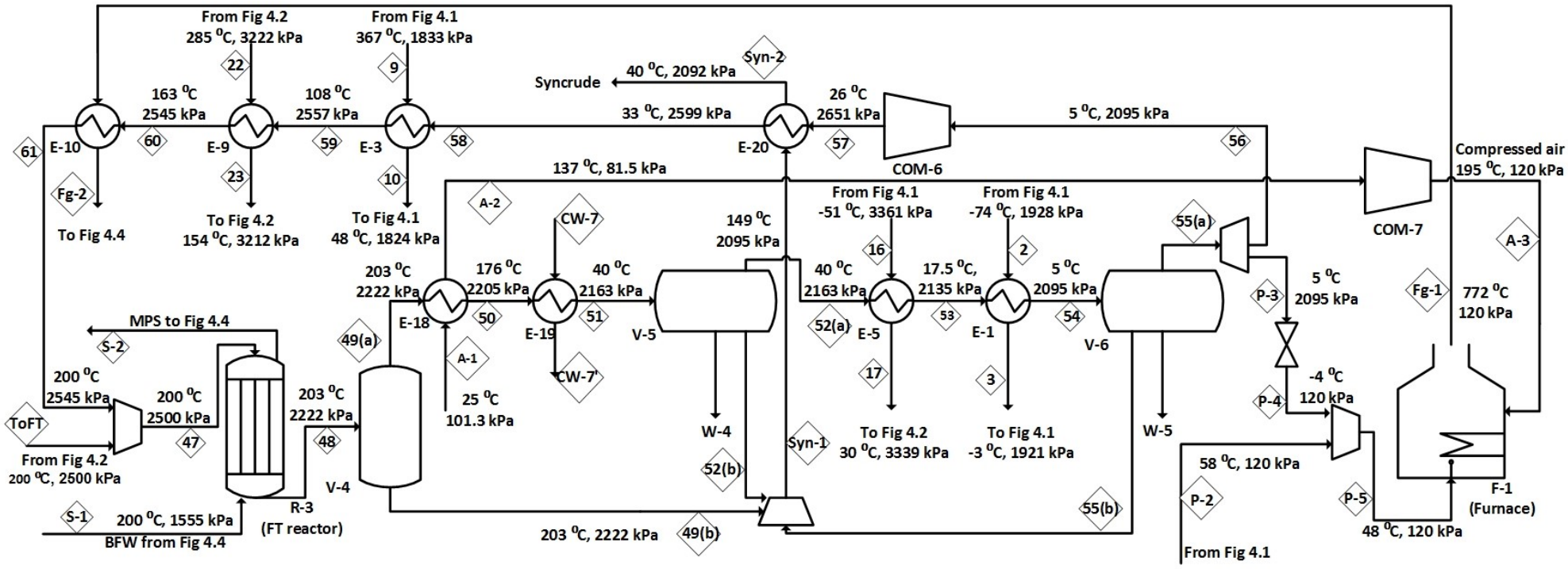

Fig. 4.3. Process flow diagram of syncrude manufacturing by the FTS

4.1.4. Steam loop and energy recovery for electivity generation

The produced energy either in the form of heat or steam in the GTL plant is recovered to produce electricity as presented by Fig. 4.4. The produced saturated steam of the FT reactor at 200 ºC and 1555 kPa (stream S-2) is split into two streams, i.e., S-2(a) and S-2(b) in Fig. 4.4. Stream S-2(b) is used in the reboiler of the MEA regenerator in Fig. 4.2, which is returned to the reactor as saturated water at 1555 kPa (stream S-1(b)). Stream S-2(a) is superheated to 270 ºC in E-21 by exchanging heat with the flue gas (stream Fg-2) coming from E-10 in Fig. 4.3. The superheated steam is mixed with a second stream of superheated steam at 270 ºC and 1555 kPa (stream S-11), which is produced by recovering heat from the flue gas in E-26. The mixed superheated steam (stream S-4) enter a steam turbine (EX-2) to generate electricity. The outlet of the steam turbine at 76 ºC and 40 kPa (stream S-5) enters a condenser (E-22) to fully condense the remaining steam. The condensate (stream S-6) enters a pump to increase its pressure to 1555 kPa. The pressurized water is split into two streams, i.e., streams S-8 and S-10. The first split (stream S-10) goes to E-26 for the production of superheated steam. The second split (stream S-8) is heated to 121 °C by the produced carbon (SC-4) in E-23. It is then saturated by flue gas to 200 ºC in E-24 to be recycled back to the FT reactor. It should be noted that the produced carbon (SC-5) leaving E-23 is further cooled down from 86 ºC to 40 ºC by CW in E-25 to exit the plant.

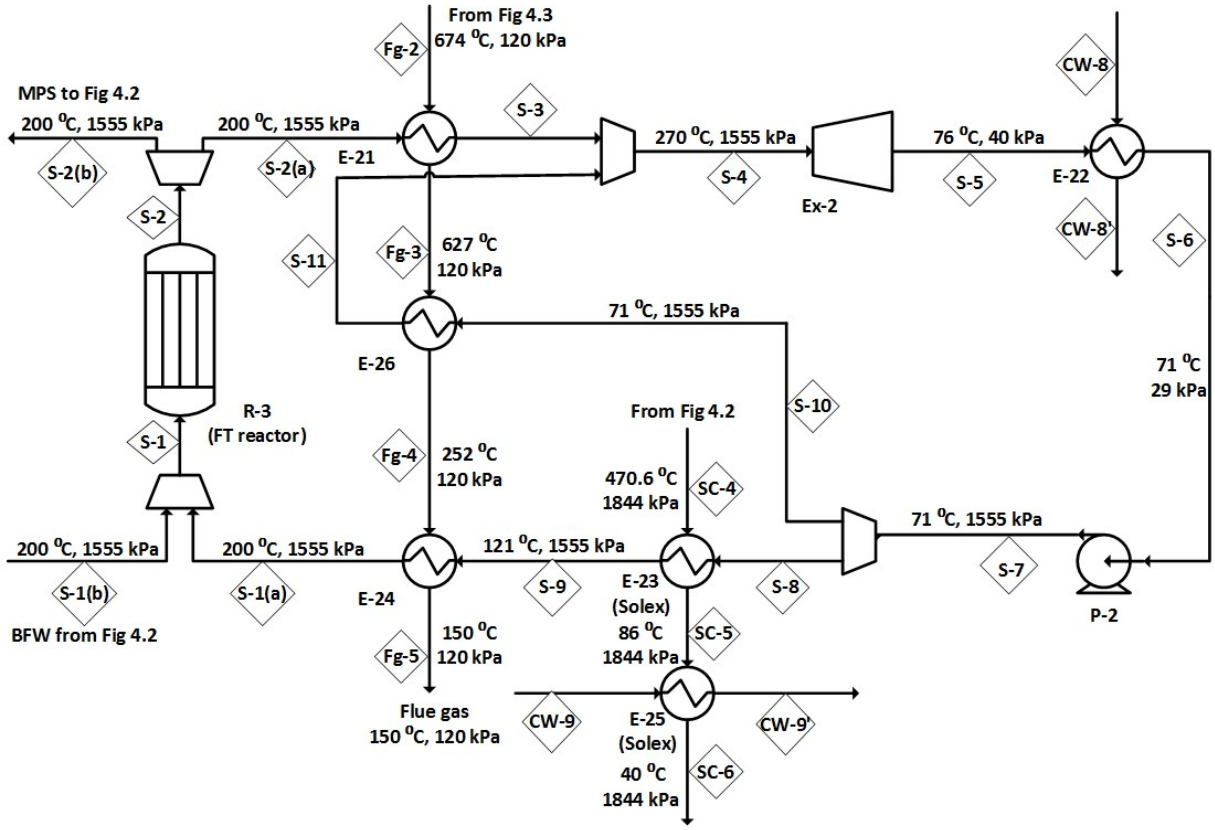

Fig. 4.4. Process flow diagram of the energy recovery unit

4.2. Performance of the CH_4 decomposition unit

4.2.1. Methane decomposition reactor

The hydrogen is produced by catalytic decomposition of methane in a Cu-Bi (45 and 55 mol%) molten media. NaBr is used at the top of the reactor to prevent the entrainment of the catalyst by the produced solid carbon. The MDR is a multi-tubular reactor, which is heated by the furnace. The duty and CH_4 conversion of the MDR are 737.6 MW and 80%, respectively. The reactor contains 73333 tubes with diameter of 0.1 m and the length of 0.76 m. The profiles of pressure, gas hold-up, and methane conversion along the reactor height are presented in Figs. 4 (A), (B),

and (C), respectively. It can be seen in Fig. 4 (A) that the pressure of the reactor drops linearly from 1900 kPa at the bottom of the reactor to 1844 kPa at the top of the reactor. On the other hand, Fig. 4 (B) shows that the reactor gas hold-up increases from 0.1206 to 0.1333 as the height of the reactor increases. The same increasing trend is also observed for CH_4 conversion as shown in Fig. 4 (C). It is worth mentioning that the conversion of the MDR is limited to 80% to avoid an excessive reactor volume.

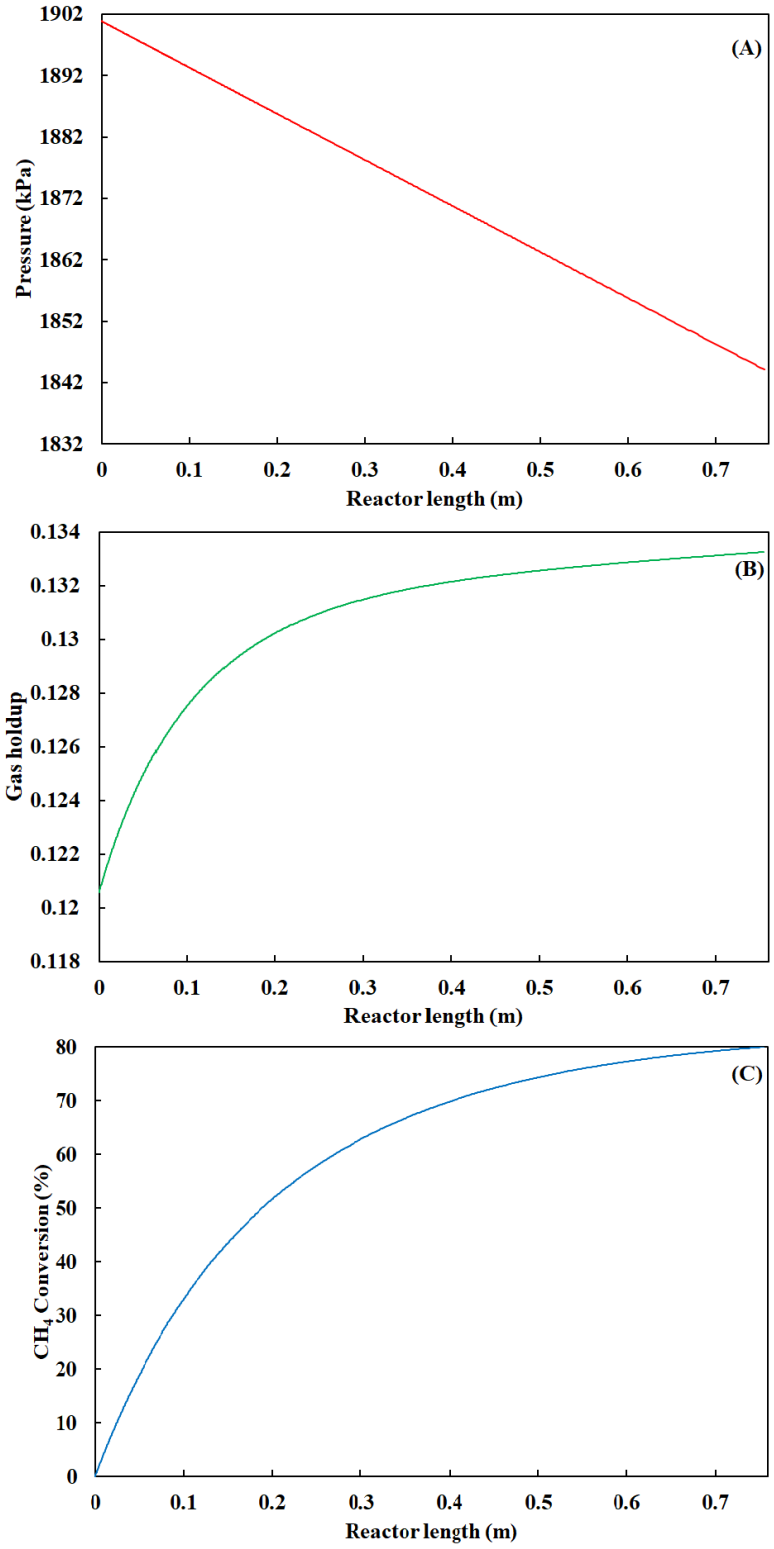

Fig. 4.5. The profiles of (A) pressure, (B) gas hold-up, and (C) CH_4 conversion of the MDR.

4.2.2. Hydrogen purification by pressure swing adsorption

Since the produced hydrogen by the MDR contains methane and inert compounds (N_2 and CO_2), the outlet gas stream of the MDR is sent to the PSA unit to increase the purity of hydrogen. The PSA unit operates based on the difference between the affinities of the gaseous compounds to be adsorbed on the surface of adsorbents. The impurities (CH_4 and CO_2) are adsorbed onto the surface of solid adsorbents at 3381 kPa. After the adsorption beds become saturated, their pressure is dropped to 101 kPa to desorb the adsorbed species. The hydrogen purity and recovery of the PSA unit is 99.97% and 93%, respectively, which are achievable by using 12 adsorption columns [58]. A pressure drop of 20 kPa is assumed on the H_2-rich stream leaving the PSA columns.

4.3. Performance of the RWGS unit

4.3.1. RWGS reactor

The isothermal RWGS reactor has 2210 tubes with the diameter and length of 0.1 and 0.5 m, respectively. The feed gas with the mole fraction of H_2:0.7085, CO_2:0.29, H_2O:0.0007, N_2: 0.0002, and CO: 0.0004 enters the reactor at 1023 °C and 3303 bar. This feed composition ensures an H_2/CO ratio of 2 at the outlet of the reactor. The duty of the RWGS reactor is 140 MW, which is obtained from an isothermal equilibrium reactor in Aspen HYSYS. The reactor's atom balances on C, H, O, and N are presented in Table 4.1. It is seen that the maximum error on atom balances is 1.72×10^{-2}%, which indicates the accuracy of converging the recycle stream of the RWGS in MATLAB. The total inlet and outlet mass flow rates to the reactor are 744221 (from Aspen HYSYS to MATLAB) and 744109 kg h^{-1} (from MATLAB to Aspen HYSYS), respectively, which also confirms the accuracy of the simulation of the RWGS reactor in MATLAB (a percent error of 0.015%).

Table 4.1. Atom balances at the inlet and outlet of the RWGS reactor

Atom	Inlet (kmol h^{-1}) [a]	Outlet (kmol h^{-1}) [b]	Error (%)
C	15198.36	15195.74	1.719×10^{-2}
H	74205.73	74205.67	8.057×10^{-5}
O	30409.47	30404.21	1.73×10^{-2}
N	24.48	24.48	0

[a] from Aspen HYSYS to MATALB, [b] from MATLAB to Aspen HYSYS

The pressure, CO_2 conversion, and molar flow rate profiles of the reactor are depicted in Figs. 4.6 (A), (B), and (C), respectively. Fig. 4.6 (A) shows a pressure drop of 67 kPa across the length of the reactor. The molar flow rates of the reactants (H_2 and CO_2) and products (CO, H_2O) along the reactor length are shown in Fig. 4.6 (B) for one of the reactor tubes. The molar flowrate profiles of the CO and H_2O overlap each other due to the fact that by the conversion of 1 mol of H_2 or CO_2, 1 mol of CO and H_2O are produced. As can be seen in Fig. 4.6 (B), the reactor approaches equilibrium at 0.25 m from the reactor entrance. Fig. 4.6 (C) presents the single pass CO_2 conversion of the reactor tubes, which reaches to an equilibrium conversion of 79.13% at 1023 ºC.

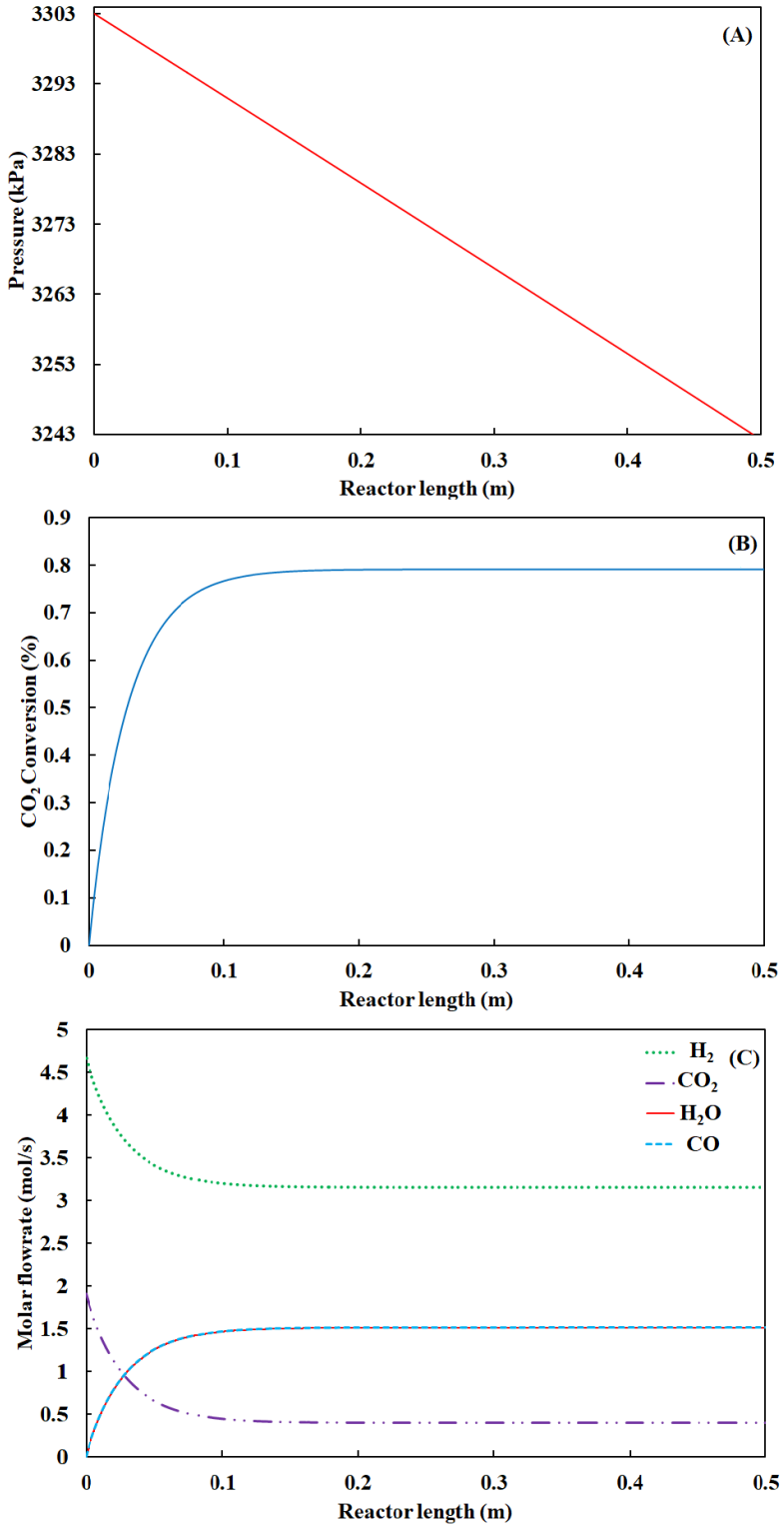

Fig. 4.6. The profiles of (A) pressure, (B) single pass CO_2 conversion, and (C) molar flow rates of the RWGS reactor for one reactor tube.

4.3.2. CO_2 separation and recycling by monoethanolamine

The MEA absorption column has 22 trays with a tray efficiency of 8 % [59]. The MEA regenerator has 10 trays with 25% efficiency [59]. The reflux ratio and reboiler duty of the regenerator are 0.584 and 180 MW, respectively. The required MPS for the MEA regenerator reboiler is supplied by a portion of the MPS produced in the FT reactor. The energy consumption of the MEA reboiler is 5.036 GJ/tonne CO_2. The application of CO_2 separation and recycling by MEA results in an overall CO_2 conversion of 98.1% in the RWGS unit, which is calculated based on the molar flow rate of the feed CO_2 to the plant (1.225×10^4 kmol h^{-1}) and the molar flow rate of CO_2 in the produced syngas (233 kmol h^{-1}), i.e., stream ToFT in Figs. 4.2.

4.4. Performance of the FT unit

4.4.1. Selection of the number of carbons

Although a syncrude consists of a significant amount of alkanes and alkenes with high number of carbon atoms (heavy hydrocarbons), most of the simulations published in the literature are limited to maximum number of carbon atoms up to 30. This limitation mainly stems from Aspen HYSYS database, which does not include heavier hydrocarbons. Based on the literature reviewed in Chapter 2, two approaches are generally taken to simulate FT reactors and to determine their product distribution: (1) defining FT products based on the available number of hydrocarbons in the software or (2) lumping heavy hydrocarbons (e.g. C5 plus) into one representative hydrocarbon (e.g. octane) to be used in the software. An accurate analysis cannot be achieved from these approaches due to the fact the real number of alkanes and alkanes in FT products are greater than the chosen hydrocarbons reported in the literature. As a result, these two approaches fail to

accurately calculate the production rate of heavy hydrocarbons and to estimate the produced syncrude physical properties such as density and viscosity.

Since the LTFT mainly produces wax or heavy hydrocarbons, one of the objectives of this thesis is to accurately model the FT reactor with a sufficiently high number of carbon atoms. To do this, the FT reactor is simulated in MATLAB to overcome the above-mentioned obstacles in Aspen HYSYS. To determine the sufficient number of alkanes and alkenes, the effect of the number of carbon atoms on the product distribution of the FT reactor is studied for alkanes and alkenes with maximum number of carbon atoms of n = 50, 100, 150, and 200. The analysis is performed for one reactor tube under the operating conditions of the FT reactor, i.e., T = 200 ºC, P = 2500 kPa, $H_2/CO = 2$, and a single tube feed flow rate of 0.544 mol s^{-1}. Figs. 4.7 (A) to (D) present the mole fractions of alkanes and alkenes (except CH_4) for the maximum number of carbon atoms from 50 to 200. The general observed trend is that by increasing the number of carbon atoms, the mole fractions of alkanes and alkenes drop. The majority of alkenes are formed when n is between 2 and 50. It is observed in Fig. 4.7 (A) that when the maximum number of carbon atoms is 50, the mole fraction of $C_{50}H_{100}$ alkene approaches zero. However, the mole fraction of $C_{50}H_{102}$ alkane is 4.3724×10^{-5}, which suggests more alkanes should be included in the simulation. By increasing n to 100 in Fig. 4.7 (B), the mole fraction of alkenes remains close to zero. On the other hand, the mole fraction of $C_{100}H_{202}$ drops to 3.9425×10^{-6}. By further increasing the maximum number of carbon atoms to 150, Fig. 4.7 (C), the mole fraction of $C_{150}H_{302}$ is equal to 4.6688×10^{-7}. Figure 4.7 (D) shows that when hydrocarbons with the number of carbon atoms between 150 and 200 are included in the simulation, their mole fractions become extremely small, which can be excluded from the simulation. In this work, the maximum number of alkanes and alkenes is limited to

hydrocarbons with the number of carbon atoms of 150 and 149, respectively, to ensure that the produced syncrude is represented by a sufficient number of alkanes and alkenes.

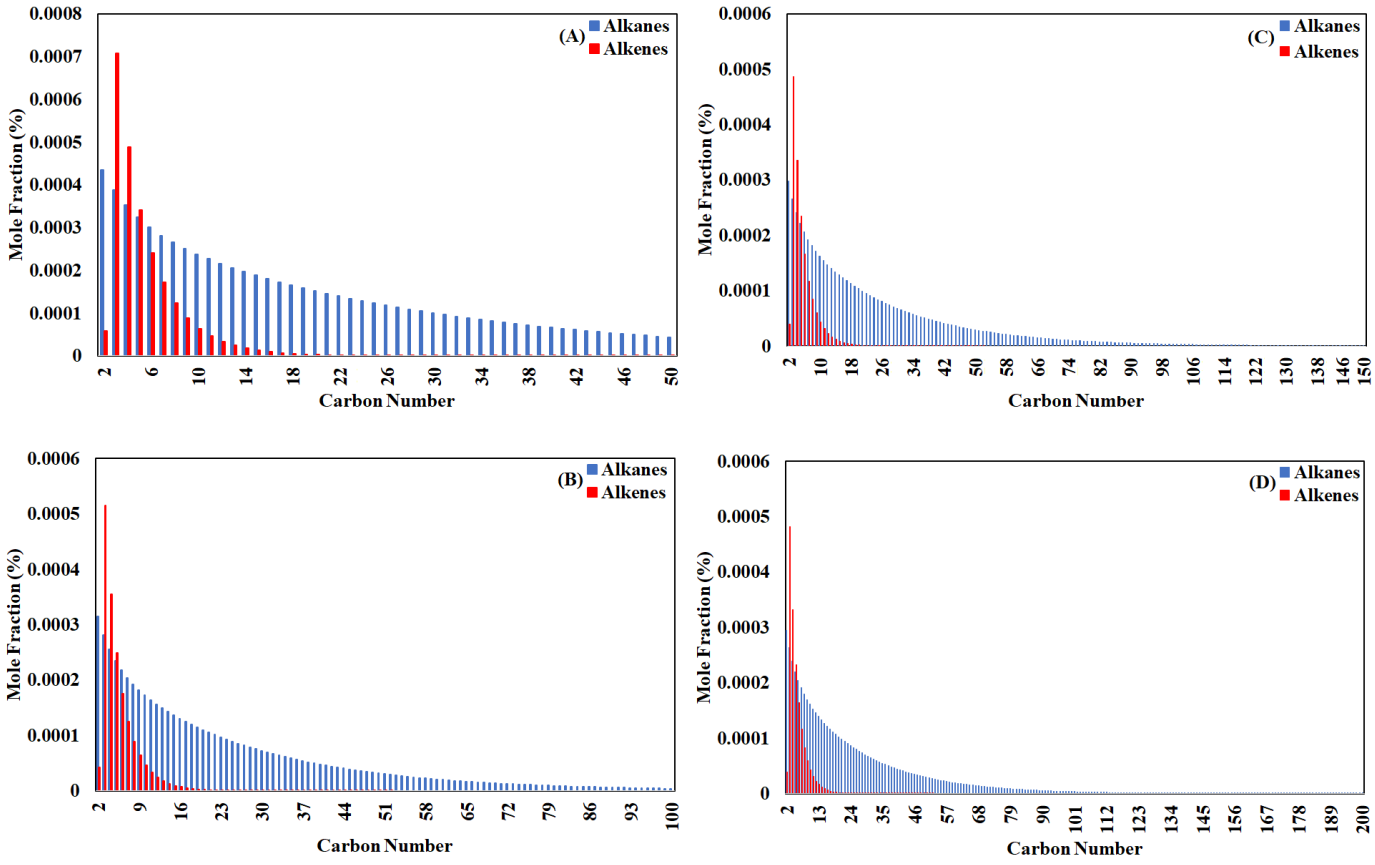

Fig. 4.7. Effect of maximum number of carbon atoms on the product distribution of the FT reactor, (A) n=50, (B) n=100, (C) n=150, and (D) n=200.

4.4.2. Selection of and the representative hydrocarbons for grouped hydrocarbons

As mentioned in Chapter 3, to accelerate the convergence of the simulation of the FT reactor in MATLAB, normal alkanes $C_{13}H_{28}$, $C_{18}H_{38}$, $C_{23}H_{48}$, $C_{28}H_{58}$, $C_{33}H_{68}$, $C_{38}H_{78}$, and $C_{65}H_{132}$ are used

as the representative of alkanes and alkenes with the number of carbon atoms higher than 10, which are grouped into 7 cuts: C_{11}-C_{15}, C_{16}-C_{20}, C_{21}-C_{25}, C_{26}-C_{30}, C_{31}-C_{35}, C_{36}-C_{40}, and C_{40+} (C_{40} to C_{150}). The representative molecules are selected based on the average molecular weight of alkanes and alkenes in each cut, which is calculated by Eq. (4-1):

$$M_{avg} = \sum_{1}^{i} \left(y_{alkane,i} \times M_{alkane,i} + y_{alkene,i} \times M_{alkene,i} \right) \qquad (4-1)$$

in which M_{avg} (g mol^{-1}) is the average molecular weight of a cut, $y_{alkane,i}$ is the mole fraction of the alkanes in the cut, $y_{alkene,i}$ is the mole fraction of the alkenes in the cut, $M_{alkane,i}$ (g mol^{-1}) is the molecular weight of the alkanes in the cut, and $M_{alkene,i}$ (g mol^{-1}) is the molecular weight of the alkenes in the cut. The results of the averaging of the molecular weight of the cuts as well as the molecular weight of the representative molecules for each cut are included in Table 4.2. It is seen that the molecular weight of the representative alkanes is close to the average molecular weight of each cut, which justifies the selection of the representative molecules.

Table 4.2. The average molecular weight of each cut and the molecular weight of the selected representative alkanes.

Cut(alkanes and alkenes)	**Average M of cut (g mol^{-1})**	**Representative alkane**	**Representative alkane M (g mol^{-1})**
C_{11}-C_{15}	182	$C_{13}H_{28}$	184
C_{16}-C_{20}	253	$C_{18}H_{38}$	254
C_{21}-C_{25}	323	$C_{23}H_{48}$	324
C_{26}-C_{30}	393	$C_{28}H_{58}$	394
C_{31}-C_{35}	463	$C_{33}H_{68}$	464
C_{35}-C_{40}	533	$C_{38}H_{78}$	534
C_{40+}	909	$C_{65}H_{132}$	912

4.4.3. FT reactor

Since a high volumetric flow rate of syngas is required for the manufacturing of 30000 bbl/day of syncrude, 14 parallel FT reactors with a diameter of 6.1 m are used in the FT unit. Each reactor contains 6660 tubes with a length and diameter of 10.1 m and 0.0508 m, respectively. The single pass CO_2 conversion in each reactor is 36.1 % to avoid temperature run away in the FT reactors. The overall CO conversion of the FT unit is 98.3 % with 99% recycle ratio, which is the ratio of recycled stream (stream 56) to stream 55(a). The diameter of the LTFT reactor is calculated by Eq. (4.2) [56].

$$D_S = \left(\frac{N_T * 4 * F_{TC} F_{SC} p_C p_T^2}{\pi}\right)^{0.5} \qquad (4-2)$$

where N_T (unitless) is the number of tubes, P_C (unitless) is the pitch configuration factor, which is equal to 0.866 for a triangular pitch, F_{TC} (unitless) is the tube count constant, which is assumed to be 1.08 for one tube pass, F_{SC} (unitless) is a correction factor which equals to 1.15 for floating head heat exchangers, P_T (m) is the tube pitch, which is assumed to be $1.25d_o$, and d_o (m) is the outside diameter of the tubes.

The atom balances of the FT reactor on C, H, O, and N are given in Table 4.3. A maximum absolute percent error of 0.26% is observed on C balance, which confirms the accuracy of the simulation of the FT reactor as well as the convergence of the recycle stream of the FT reactor in MATLAB. The total inlet and outlet mass flow rates of the FT reactor are 3334366 (from Aspen HYSYS to MATALB) and 3339021 (from MATLAB to Aspen HSYYS) kg h^{-1} with an absolute percent error of 0.14%.

Table 4.3. Atom balance of the FT reactor

Atom	Inlet (kmol h^{-1}) [a]	Outlet (kmol h^{-1}) [b]	Error (%)
C	142977.49	143353.77	-0.2632
H	437883.07	438612.08	-0.1665
O	71657.46	71630.48	0.038
N	1042.17	1040.53	0.157

[a] from Aspen HYSYS to MATALB, [b] from MATLAB to Aspen HYSYS

Figs. 4.8 (A) and (B) present the temperature and pressure profiles of the FT reactor. As seen in Fig. 4.8 (A), the reactor temperature increases at the entrance of the reactor and reaches a maximum of 204.4 ºC at 1 m due to the produced heat by the FT reactions. However, the temperature decreases to 203.2 ºC at the outlet of the reactor by transferring the generated heat from the tubes to the cooling fluid in the shell, i.e., the boiling water at 200 ºC and 1555 kPa. Fig. 4.8 (B) shows that the pressure drop of the reactor is 278 kPa, which is slightly above 10% of the inlet pressure of the reactor at 2500 kPa.

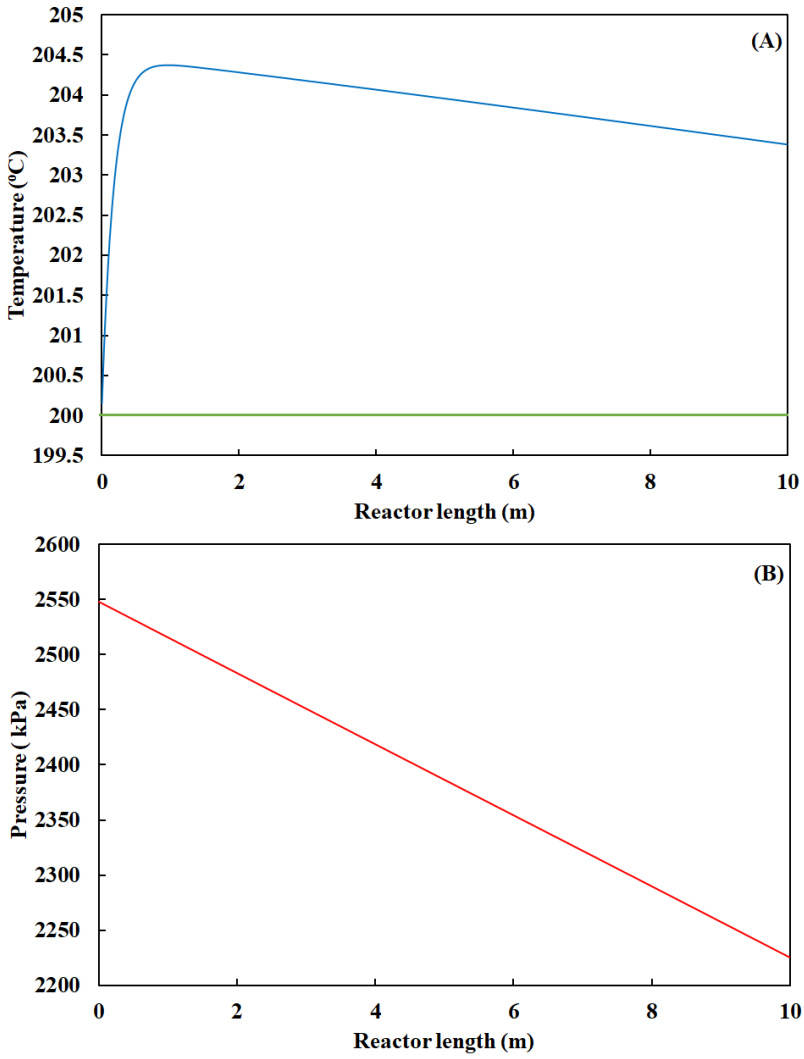

Fig.4.8. Profiles of (A) temperature and (B) pressure of the FT reactor.

4.5. Energy balance of the plant

The steam, electricity, and heat balances of the GTL plant are presented in Tables 4.4 to 4.6. As shown in Table 4.4, the plant produces an excess MPS of 6.2 $\times 10^5$ kg hr^{-1}, which is used for electricity generation as explained above in Section 4.1.4. The electricity balance of the plant is given in Table 4.5. The total electricity consumption of the compressors and pumps is equal to

108.84 MW. The total produced electricity generation by the feed natural gas expander (EX-1) and the steam turbine (EX-2) amounts to 147.8 MW, which leaves an excess electricity of 38.93 MW, which is sold to add to the revenue of the plant. It should be noted that 12.97 MW of the excess electricity is generated by the expansion of the feed natural gas in EX-1. The remaining 25.96 MW is originated from burning the purge gas in the furnace. It would have been possible to reduce the excess electricity associated with burning the purge gas to zero by increasing the recycle ratio of the FT synthesis loop to values greater than 99%. However, the 99% recycle ratio is chosen in this work to avoid excessive MATALB run time to converge the FT recycle loop. As reported in Table 4.6, the total heat demand of the MDR and RWGS reactor is equal to 931.38 MW, which is provided by the radiation section of the furnace. The duty of the radiation section of the furnace is calculated at 980 MW using a 95% furnace efficiency. The thermal energy of the furnace flue gas is recovered in E-10 (64.32 MW) to heat a process stream (stream 60 in Fig. 4.3), in E-21 (30.67 MW) to superheat the balance of the FT reactor MPS (stream S-2(a) in Fig. 4.4), in E-26 (231.8 MW) to produce superheated steam from BFW (stream S-10 in Fig. 4.4) and, in E-24 (59.28 MW) to saturate the return BFW from EX-2 (stream S-9 in Fig. 4.4).

Table 4.4. Medium pressure steam balance of the GTL plant

Equipment	**Required MPS (kg hr $^{-1}$)**	**Equipment**	**Produced MPS (kg hr^{-1})**
MEA regenerator reboiler	3.35×10^5	FT reactor	9.55×10^5
Excess MPS = 6.20×10^5 kg hr^{-1} (used for electricity generation)			

Table 4.5. Electricity balance of the GTL plant

Equipment	Required electricity (MW)	Equipment	Produced electricity (MW)
COM-1 (PSA feed compressor)	32.12	EX-1 (feed natural gas expander)	12.97
COM-2 (PSA purge blower)	1.38	EX-2 (steam turbine)	134.83
COM-3 (RWGS reactor recycle compressor)	3.50	Total	147.8
COM-4 (RWGS reactor recycle compressor)	3.72		
COM-5 (RWGS reactor recycle compressor)	3.44		
COM-6 (FT reactor recycle compressor)	30.20		
COM-7 (Combustion air blower)	28.68		
P-1 (Lean MEA pump)	5.29		
P-2 (BFW pump in the steam loop)	0.54		
Total	108.87		
Excess electricity = 38.93 MW (to be sold)			

Table 4.6. Heat balance of the GTL plant

Equipment	Required heat (MW)	Equipment	produced heat (MW)
MDR	737.59	Furnace (radiation zone)	980 [a]
RWGS (pre-heater and reactor)	193.79		
Total	931.38		

[a] calculated as the total heat demand of the MDR and the RWGS reactor (931.8 MW) divided by the furnace efficiency (0.95).

4.6. Economic and environmental evaluation of the GTL plant

4.6.1. Economic assessment

The economic analysis of the GTL plant is performed based on the estimation of the plant grassroots cost (C_{Gr}) and the cost of manufacturing without deprecation (COM_d) to determine the net present worth (NPW) of the plant. The grassroots cost (C_{GR}) is determined by CAPCOST 2017 using a Chemical Engineering Plant Cost Index of 608 in 2019. The details of the estimation of the plant C_{Gr} by CAPCOST are available in Appendix F. The dimensions of the two- and three phase separators are calculated based on the equations provided in Appendix C. The diameter of the MEA absorption and regenerator columns are obtained by Aspen HYSYS. A tray spacing of 1 m is assumed for the estimation of the height of the columns. Parallel two- and three-phase separators as well as parallel columns are used in the plant to avoid excessive diameters for the separators, MEA absorption column, and MEA regenerator. The number and dimensions of the separators and columns are available in Appendix F. The cost of the PSA unit is estimated based on the economic data reported by Luberti using the 0.6 rule [58]. The costing of heat exchangers

involving solid carbon is based on the cost of the Solex heat exchanger using the 0.6 rule [60]. The selection of the materials of construction of different pieces of equipment is based on the guidelines provided by Rezaei and Catalan [55]. Table 4.7 summarizes the economic data that are used to evaluate the profitability of the GTL plant.

Table 4.7. Economic data

Parameter	Value	Reference
RWGS synthesis catalyst (initial fill)	\$22954 m^{-3}	[55]
RWGS synthesis catalyst (replacement)	\$7169 m^{-3} yr^{-1}	[55]
FT synthesis catalyst (initial fill)	\$33.07 kg^{-1}	[61]
FT synthesis catalyst (replacement)	\$ 13228 m^{-3} yr^{-1} (life time of 3 years)	[61]
MDR catalyst (initial fill of Bi)	\$11.02 kg^{-1}	[62]
MDR catalyst (initial fill of Cu)	\$ 6.01 kg^{-1}	[63]
NaBr makeup	\$3.450 kg^{-1}	[64]
Cooling water (CW)	\$0.0157 m^{-3}	[57]
Electricity	\$0.0674 kWh^{-1}	[57
Natural gas (2019)	\$0.0939 std m^{-3}	[55]
CO_2 (2019)	\$70 $tonne^{-1}$	[55]
Syncrude (2019) Based on Edmonton syncrude	\$59.31 bbl^{-1}	[65]
Plant operating hours	8240 hr yr^{-1}	
Chemical engineering plant cost index (2019)	608	
Interest rate	20%	
Taxation rate	26%	
MACRS recovery period	5 years	
Plant life for economic analysis	15 years	
Land	\$4 MM	
Construction period	2 years	
Salvage value	0	
Working capital (WC)	15% of total capital investment	
Total capital cost	C_{GR} + WC	

As shown in Appendix F, the total C_{GR} (fixed capital investment) of the plant is $\$1645.3\times10^6$. The breakdown of the bare module cost of the equipment is shown in Fig. 4.9. The most expensive equipment in the GTL plant is the FT (24.36%) and MD (24.73%) reactors which is followed by the compressors (15.14%), heat exchangers (8.89%), expanders (6.87%), PSA (5.32%), columns (5.09%), RWGS reactor (5.08%), 2 and 3 phase separators (4.05%), and pumps (0.48%).

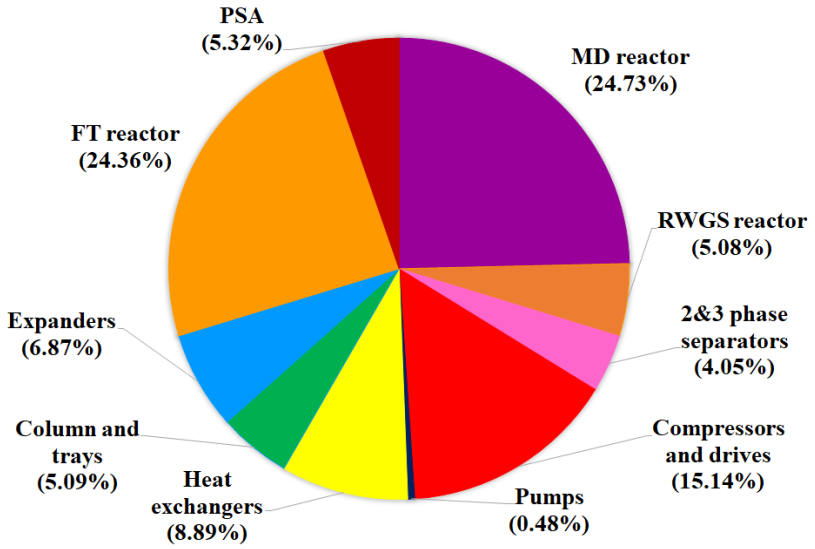

Fig 4.9. Breakdown of the total bare module cost of the equipment in the GTL plant.

The COM_d of the plant is calculated by Eq. (4.3) [57]:

$$COM_d = 0.180FCI + 2.76C_{OL} + 1.23(C_{UT} + C_{WT} + C_{RM}) + C_{NaBr} + C_{cat} \qquad (4-3)$$

in which FCI ($) is the fixed capital cost of the plant, which is equal to the plant's C_{GR} estimated by CAPCOST, C_{OL} ($ yr^{-1}) is the annual cost of operating labour, C_{UT} ($ yr^{-1}) is the annual cost of utilities, C_{WT} ($ yr^{-1}) is the annual cost of waste treatment, which is assumed zero in this thesis,

C_{RM} ($ yr^{-1}) is the annual cost of raw materials, C_{NaBr} is the annual cost of make-up NaBr, and C_{cat} is the annual replacement cost of the catalysts in the MDR and RWGS reactors.

The cost of operating labour is calculated using Eq. (4.4) [57]:

$$N_{OL} = \left(6.29 + 31.7P^2 + 0.23N_{np}\right)^{0.5} \qquad (4-4)$$

where N_{OL} is the total number of operators, P is the number of particular processing steps (solid carbon heat exchangers), and N_{np} is the number of non-particular processing steps including compression, heating, cooling, mixing, and reaction. Assuming 49 working weeks in a year, three employees per shift with 8 working hours (24 working hours per day), 365 operating days per year, and the wage of $32.17 per hour, the annual C_{OL} of the plant is estimated at $\$8.70\times10^6$ per year.

The annual cost of raw materials, utility, catalyst replacement, and make-up NaBr are presented in Table 4.8. The mass flow rate of the make-up NaBr is 2% of the mass flow rate of the produced solid carbon by the MDR [67]. The annual cost of raw materials includes the purchase cost of natural gas and CO_2, which are equal to $\$431.06\times10^6$ and $\$310.90\times10^6$, respectively. The annual cost of utilities (cooling water) is $\$14.37\times10^6$. The total annual cost of the RWGS and FT reactors' catalyst replacement cost and NaBr make-up is $\$161.25\times10^6$.

Table 4.8. The annual cost of raw materials, utilities, make-up NaBr, and the CH_4 decomposition and RWGS reactors' catalyst replacement cost.

Cost of raw materials (C_{RW})	**$Millions per year**
Natural gas	431.06
CO_2	310.90
Total cost	741.96
Cost of utility (C_{UT})	**$Millions per year**
Cooling water (CW)	14.37
Catalyst replacement and make-up NaBr	**$Millions per year**
NaBr	144.92
RWGS catalyst	0.039
FT catalyst	16.3
Total cost	161.25

Table 4.9 summarizes the C_{Gr}, C_{OL}, C_{UT}, C_{RM}, and COM_d of the plant as well as the revenue from selling the syncrude and excess electricity (excluding the sale of solid carbon). Since the GTL plant is a net consumer of CO_2 (without considering the upstream emissions of the feed natural gas and CO_2), the CO_2 tax of the plant is zero. The COM_d of the plant is equal to 1411.71×10^6 yr^{-1} with a total revenue of $\$632.47\times10^6$ yr^{-1}.

Table 4.9. Summary of the cost of manufacturing without depreciation and revenue

Cost of manufacturing without depreciation	**$Millions per year**
Cost of operating labor (C_{OL})	8.70
Cost of raw materials (C_{RM})	741.96
Cost of utility (C_{UT})	14.37
Catalyst replacement and NaBr makeup	161.25
COM_d	1411.71
Revenue (without selling of solid carbon)	**$Millions per year**
Electricity	21.62
Syncrude	610.85
Total	632.47

The profitability analysis of the plant is performed by finding a selling price for carbon that results in an NPW = 0, i.e., the breakeven price of carbon. As shown in Fig. 4.10, the plan breaks even after 15 years if the produced carbon is sold at $633 per tonne, which is slightly above the average value of the selling price of carbon reported in the literature [68]

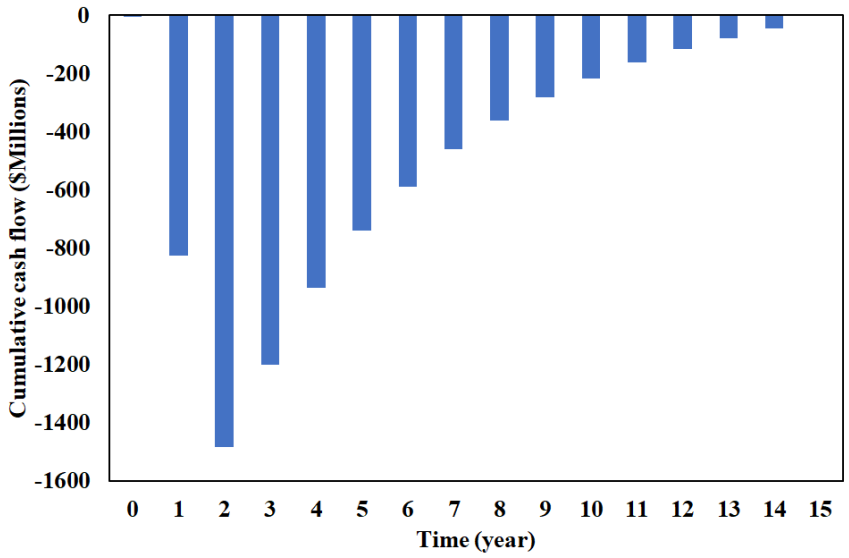

Fig. 4.10. Cumulative discounted after-tax cash flow diagram for the plant with carbon sale price of $0.633 kg^{-1}.

Based on the economic analysis, the manufacturing cost of syncrude produced by the GTL plant is $137.06 bbl^{-1}. The production cost of syncrude is compared with the values reported by Zhang et al. for a P2L and a combined P2L/P2G plants in Table 4.10 [31,41]. The P2L and P2L/P2G plants include the hydrogen production by water electrolysis, syngas production by the RWGS reaction, and the HTFT for syncrude production. The comparison between the production cost of syncrude from those reported by Zhang et al. and the GTL plant in this thesis indicates that H_2

production by CH_4 decomposition reduces the manufacturing cost of syncrude at least by 32.4%. It should be noted that for the economic feasibility of the P2L and combined P2L/P2G plants, Zhnag et al. have assumed a high syncrude selling price at \$140 bbl^{-1} in 2030. However, the present GTL plant becomes feasible with a syncrude selling price of \$59.31 per bbl, which is almost one third of what is assumed by Zhang et al. Even though syncrude production by sourcing hydrogen from CH_4 decomposition is a competitive process to those plants that utilize H_2 from water electrolysis for the reformation of CO_2 to GTL products, the economic feasibility of the plant in this work depends on the quality of the produced carbon and the market capacity to sell the produced carbon.

Table 4.10 Comparison of the manufacturing cost of syncrude from this work and those reported in the literature.

Plant	H_2 production method	Production cost of syncrude (\$ bbl^{-1})	Reference
P2L	Water electrolysis	219.97	[41]
P2L/P2G	Water electrolysis	202.58-210.56	[41]
P2L	Water electrolysis	258.44	[31]
P2L/P2G	Water electrolysis	225.65-239.12	[31]
This work	CH_4 decomposition	137.06	-

Figs. 4.11 (A) and (B) show the results of two sensitivity analyses that are performed on the plant NPW and breakeven price of carbon, respectively. Fig. 4.11 (A) presents the variation of the plant NPW when the cost of raw materials (natural gas and CO_2) and selling price of syncrude are changed while the selling price of carbon is kept constant at \$633 per tonne. The price of natural

gas has more influence on the NPW compared to the price of CO_2. As expected, increasing the price of syncrude from its base value at \$59.31 bbl^{-1} increases the NPW of the plant. Increasing the prices of CO_2 and CH_4 from their base values makes the plant unprofitable at a carbon selling price of \$635 per tonne.

Fig. 4.11 (B) shows that the breakeven price of carbon increases by increasing the prices of CO_2 and CH_4. It is also observed that the carbon breakeven price is more sensitive to the variation in natural gas price than that of the CO_2 price. By increasing the selling price of syncrude to \$88.96 per bbl, (50% increase from its base value at \$59.31 per bbl), the breakeven price of carbon drops to \$490 per tonne. Further increase of syncrude selling price to \$118 per bbl (100% increase from its base value) results in a carbon breakeven price of \$347 per tonne (data not shown). When the price of syncrude increases to above \$80 bbl^{-1}, the breakeven price of carbon drops to less than \$500 per tonne, which makes the plant economically more favourable.

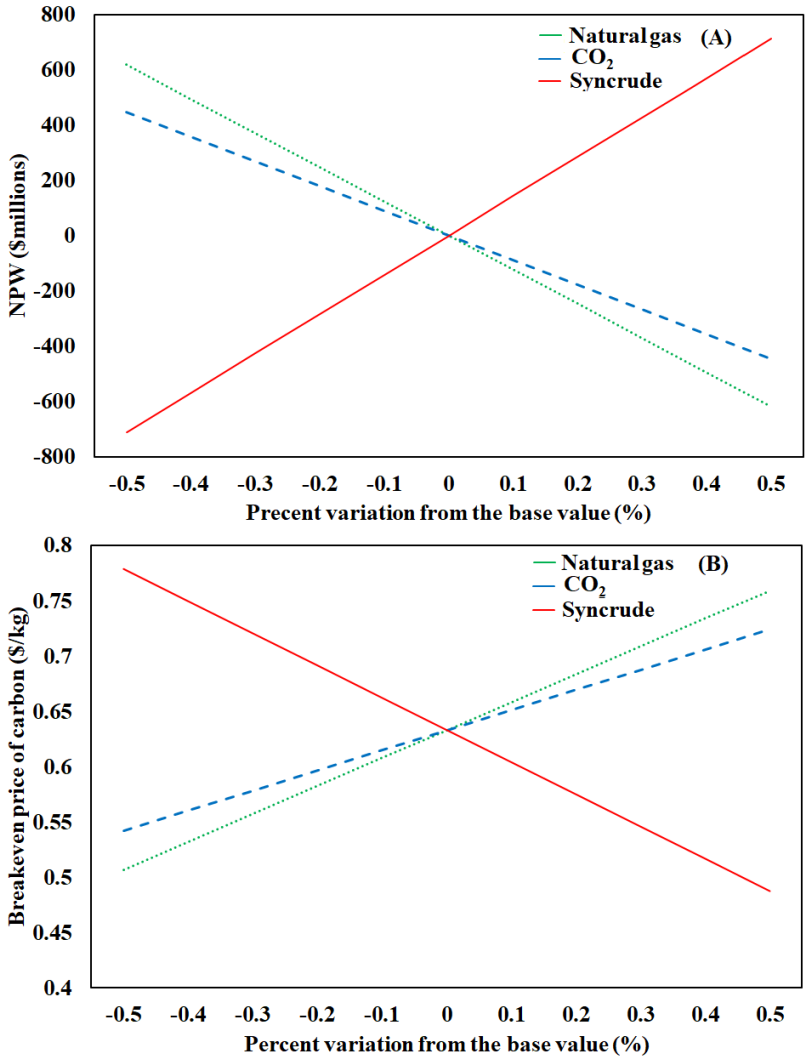

Fig. 4.11. Sensitivity analysis of the GTL plant, (A) variation of NPW by changing the cost of raw materials and selling price of syncrude at carbon selling price of $633 per tonne and (B) variation of the breakeven price of carbon by changing the cost of raw materials and selling price of syncrude.

Fig.4.12 (A) shows the sensitivity analysis on the return on investment (ROI) of the plant by changing the selling price of syncrude and solid carbon as well as the costs of the raw materials. It is seen that the ROI of the plant is 16.2% at the base values of syncrude, solid carbon, CO_2, and natural gas at, \$59 bbl^{-1}, \$0.633 kg^{-1}, \$0.0939 std m^{-3}, and \$70 $tonne^{-1}$, respectively. The sensitivity analysis indicates that the selling price of syncrude and carbon have more effect on the ROI compared to the cost of raw materials. Among the raw materials, the cost of natural gas shows a higher influence compared to the cost of CO_2 (based on the slop of the lines). By 50% increase in the selling price of syncrude from the base value, the ROI reaches to 28%. On the other hand, 50% increase in the selling price of carbon results in the ROI of 42%. To make the present plant profitable (ROI ≥20%) at the breakeven price of solid carbon (\$ 0.633 kg^{-1}), the selling price of syncrude is required to be more than \$ 71.17 bbl^{-1}.

Since any change in the selling price of syncrude and solid carbon shows more influence on the ROI of the plant than the cost of raw materials, a second sensitivity analysis is conducted on the selling price of syncrude and solid carbon by keeping the cost of CO_2 and natural gas feed constant at \$0.0939 std m^{-3}, and \$70 $tonne^{-1}$, respectively. The results are plotted in Fig. 4.12 (B) for four selling prices of solid carbon at \$ 0.95 kg^{-1}, \$ 0.82 kg^{-1}, \$ 0.63 kg^{-1}, and \$ 0.44 kg^{-1} while changing the selling price of the syncrude from \$30 bbl^{-1} to \$90 bbl^{-1}. Fig. 4.12 (B) shows that high selling price of syncrude and solid carbon at \$90 bbl^{-1} and \$0.95 kg^{-1}, respectively, increases the ROI to 53.70%. Decreasing the selling price of syncrude to \$30 bbl^{-1} at a fixed carbon selling price of \$0.95 kg, decreases the ROI to 30%. Fig. 4.12 (B) also indicates that when the solid carbon and syncrude are sold with the selling price of \$ 0.82 kg^{-1} and \$ 30 bbl^{-1}, respectively, the ROI reaches to 20%. However, by decreasing the selling price of carbon and syncrude below the values of \$0.63 kg^{-1} and \$77 bbl^{-1}, respectively, the ROI of the plant drops to less than % 20. The ROI of the plant

is less than 20% for any selling price of syncrude when the selling price of solid carbon is fixed at \$0.44 kg^{-1}.

The ROI of the present plant is also calculated based on the selling price of syncrude (\$ 70 bbl^{-1}) and the cost of the natural gas ranging from \$ 0 $MMBTU^{-1}$ to \$ 4 $MMBTU^{-1}$ from the work of Zhang et al. [29]. It is reported that by increasing the cost of natural gas from \$ 0 $MMBTU^{-1}$ to \$ 4 $MMBTU^{-1}$, the ROI of the SMR-FT and bi-reforming-FT plants drop from 24 % to 8 % and 37 % to 18.5 %, respectively. However, the ROI of the present plant for the natural gas with selling price of 0, 1, 2, 3, and 4 \$ $MMBTU^{-1}$ is calculated to be 40.7%, 33.1, 25.4%, 17.8%, and 10.2%, respectively. Therefore, under the same economic parameters, the present plant is more profitable than the SMR-FT plant. The present plant is also more profitable than the bi-reforming-FT plant at low natural gas prices. Natural prices less than \$ 2.91 $MMBTU^{-1}$ (\$ 0.1027 std m^{-3}) can make the plant in this work more profitable than the bi-reforming-FT plant.

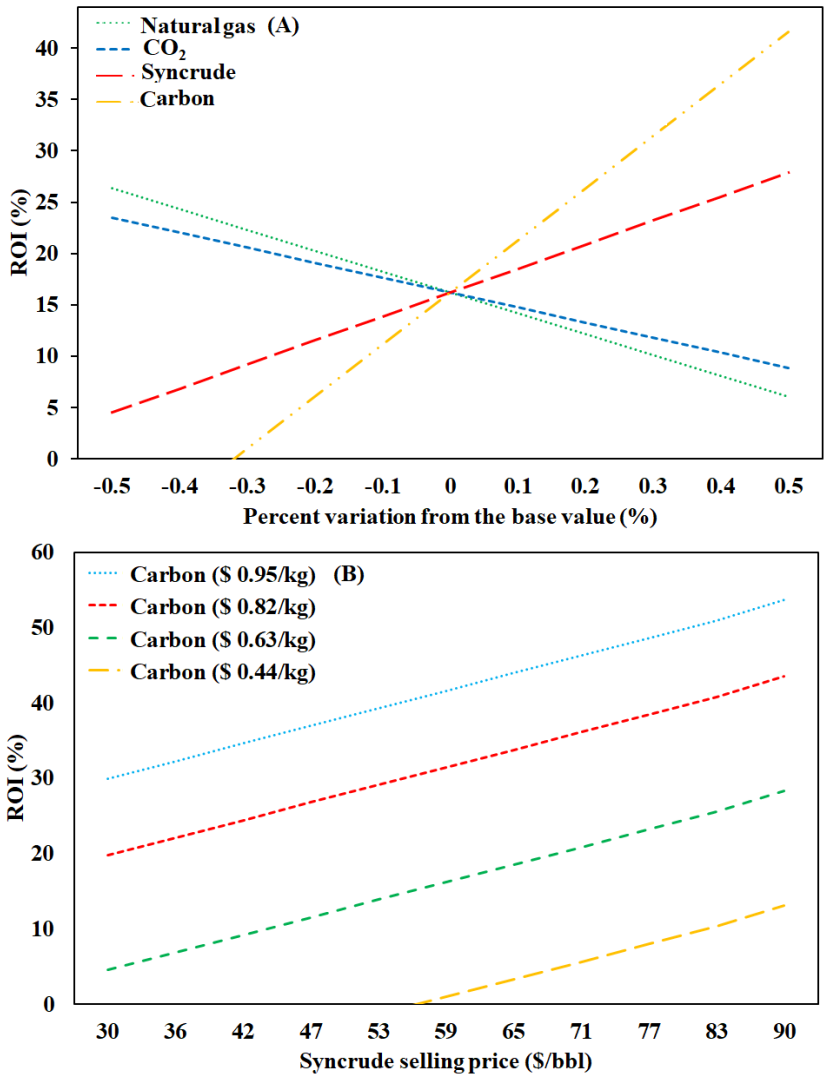

Fig. 4.12. Sensitivity analysis of the GTL plant, (A) variation of ROI percentage by changing the cost of raw materials and selling price of syncrude and carbon (B) variation of the ROI percentage by changing the selling price of syncrude for four different selling prices of carbon

4.6.2. CO_2 emissions of the GTL plant

The total CO_2 fed to the GTL plant is equal to 5.59×10^5 kg h^{-1}, which is the sum of the CO_2 feed flow rate at 5.39×10^5 kg h^{-1} and the CO_2 content of the feed natural gas at 0.2×10^5 kg h^{-1}. The plant emits CO_2 to the atmosphere from the furnace flue gas at a flow rate of 2.62×10^5 kg h^{-1}. This shows that the GTL plant is a net consumer of CO_2 at a rate of 2.97×10^5 kg h^{-1}. However, the upstream emissions for processing the feed natural gas and CO_2 must be taken into account to provide a complete picture for the CO_2 emissions of the plant. It is assumed that 0.768 and 0.20 kg CO_2 are emitted to process 1 kg of natural gas and CO_2, respectively [55,69]. The upstream CO_2 emissions of the feed natural gas (4.28×10^5 kg h^{-1}) and CO_2 (5.39×10^5 kg h^{-1}) are 3.29×10^5 kg h^{-1} and 1.08×10^5 kg h^{-1}, respectively. This results in net CO_2 emissions of 1.4×10^5 kg h^{-1}. Considering the mass flow rate of syncrude at 1.6×10^5 kg h^{-1}, 0.87 kg of CO_2 is emitted for the production of 1 kg of syncrude, which is equivalent to 4.7 kg of CO_2 to produce 1 bbl of syncrude. The summary of the CO_2 balance of the plant is given in Table 4.11. By considering the low heating value (LHV) of the produced syncrude from Aspen HYSYS simulation (43.67 MJ kg^{-1}), which is in the range of 40-44 MJ kg^{-1} reported in the literature [70], the present plant emits 19.92 g CO_2 per 1 MJ of syncrude. It should be noted that in order to estimate the LHV of the syncrude, $C_{30}H_{62}$ is used instead of the hypothetical $C_{33}H_{68}$, $C_{38}H_{78}$, and $C_{65}H_{132}$ components since Aspen HYSYS does not provide the LHV of these hypothetical components.

Table 4.11 CO_2 balance of the GTL plant

CO_2 fed to the plant (kg h^{-1})	539016
CO_2 in the natural gas (kg h^{-1})	20117
CO_2 in flue gas (kg h^{-1})	262217
Net CO_2 emissions without upstream feed natural and CO_2 emissions	-296916
Upstream CO_2 emissions of the feed natural gas (kg h^{-1})	328730
Upstream CO_2 emissions of the feed CO_2 (kg h^{-1})	107803
Net CO_2 emissions with upstream feed natural and CO_2 emissions (kg h^{-1})	139617
Syncrude production (kg h^{-1})	159799
CO_2 emission (kg CO_2/ kg syncrude)	0.87

Table 4.12 compares the net CO_2 emissions of the current plant with those of GTL plants reported in the literate. It should be noted that the CO_2 emissions reported in Table 4.12 include the upstream CO_2 emissions associated with natural gas, CO_2, and oxygen feed (where applicable). The GTL plants that produce syngas via steam reforming emit more CO_2 (115-180 g CO_2 per 1 MJ of syncrude) compared to the other types of plants, which is mostly related to the upstream CO_2 emissions related to natural gas extraction and processing. Applying an MEA unit to capture CO_2 from flue gas reduces the CO_2 emissions of the SMR-FT plant to 92 g MJ^{-1}. However, the net CO_2 emissions of the SMR-FT plants with and without an MEA unit are still higher than the present plant at 19.92 g CO_2 MJ^{-1}. The GTL plants based on bi-reforming of methane (without CO_2 capture) and autothermal reforming (ATR) of methane (with CO_2 capture) result in CO_2 emissions of 51-63 19.92 g CO_2 MJ^{-1} and 64 g CO_2 MJ^{-1}, respectively, which are lower than those of the SMR-based plants and higher than the CO_2 emissions of the GTL plant presented in this work. Although the present plant emits less CO_2 compared to the bi-reforming-FT (without CO_2 capture) and ATR-FT plants, its net CO_2 emission is higher than those of the water electrolysis-FT plants.

It should be noted that the present plant and water electrolysis based plants are a net consumer of CO_2 without considering upstream CO_2 emissions. However, due to the high CO_2 emissions associated with the natural gas extraction and processing, the present plant becomes a net emitter of CO_2 with lowest CO_2 emissions among GTL plants that use natural gas as their feed.

Table 4.12 Net CO_2 emission of the GTL plants

GTL plant	Net CO_2 emission (g MJ^{-1})	Reference
SMR-FT (without CO_2 capture)	115-180	[29]
Bi-reforming-FT (without CO_2 capture)	51-63	[29]
ATR-FT (with CO_2 capture)	64	[72]
SMR-FT(with CO_2 capture)	92	[72]
Water electrolysis-RWGS-FT (P2L)	-40	[31]
Water electrolysis-FT (P2L)	-30	[41]
This work	19.92	-

Chapter 5: Conclusions and recommendations

5.1. Conclusions

This chapter summarizes the results of the simulation of the GTL plant and its economic and environmental analyses. The recommendations for future work are also provided in this chapter. In this dissertation, the reformation of CO_2 to produce 30000 bbl per day of syncrude is simulated and investigated from economic and environmental perspectives. Chapter 3 includes the methodologies that are applied to simulate the CH_4 decomposition, RWGS, and LTFT reactors. The simulation of the RWGS and FT rectors are performed in MATLAB due to the complexity of their reaction kinetics, which cannot be defined in Aspen HYSYS. The reactors are simulated in MATLAB by importing the component molar flow rate, temperature, and pressure of their feed streams from Aspen HYSYS. The material, energy, and momentum balance differential equations of the RWGS and FT reactors are integrated in MATLAB to find the outlet component molar flow rate, temperature, and pressure of the reactors. The MATLAB simulation results are then exported to Aspen HYSYS to simulate the rest of the plant. The recycle loops of the RWGS and FT reactors are also simulated in MATALB. Even though, the inlet and outlet pressures of the MDR as well as its height are determined in MATLAB, no connection is made between MATLAB and Aspen HYSYS for the simulation of the MDR.

The process flow diagram and performance of the hydrogen production, RWGS, FT, and electricity generation units as well as the economic and environmental evaluations of the GTL plant are presented in Chapter 4. Hydrogen is produced via catalytic decomposition of CH_4 in the MDR containing the Cu-Bi molten catalyst (45 mol%-55mol%) at 1100 ^oC and 19 bar. The CH_4

conversion and duty of the MDR is 80% and 737.6 MW, respectively. The PSA unit produces 37170 kmol h^{-1} of hydrogen with the purity of 99.97%.

The syngas production is performed in an isothermal RWGS fixed-bed reactor using the Ni-$Al_{12}O_{19}$ catalyst at 1023 °C and 33 bar [45]. The MEA unit is utilized to separate unreacted CO_2 for recycling to the RWGS reactor. The energy consumption of the reboiler of the MEA regenerator column is 5.036 GJ per tonne of recycled CO_2. The RWGS unit produces 37420 kmol h^{-1} of syngas (H_2/CO_2 = 2.08) with an overall CO_2 conversion of 98.1%.

The LTFT reactor is an isothermal fixed-bed reactor at 200 ºC and 25 bar, which is modelled and simulated based on the detailed kinetic model of the Co-Re/Al_2O_3 catalyst [9,52]. 150 alkanes and 149 alkenes are considered to accurately predict the product distribution of the FT reactor. 14 parallel FT reactors are used to produce the syncrude with the LHV of 43.67 MJ kg^{-1}. The single pass CO conversion of the FT reactor is 36.1% to avoid any temperature runaway. The produced saturated MPS of the FT reactor at 200 ºC is used to provide the heat demand of the reboiler of the MEA regenerator column and to produce electricity. The recycle ratio of the FT synthesis loop at 99% makes it possible to achieve an overall CO conversion of 98.3% in the FT unit.

The available thermal energy in the furnace flue gas and produced solid carbon is recovered to produce superheated MPS at 270 ºC and 1555 kPa for electricity generation. The GTL plant is a net producer of electricity with the surplus of 38.93 MW, which is sold to generate revenue.

The economics of the plant is assessed in Chapter 4, which includes the estimation of the FCI and COM_d of the plant as well as its profitability and sensitivity analyses. The FCI and COM_d of the plant are $1645.30 and $1411.71 per year, respectively. The economic analysis indicates that the cost of raw materials ($741.96 $\times 10^6$ yr^{-1}) is a major contributor to COM_d. It is found that the

plant is not profitable if the produced solid carbon is not sold. The breakeven price of the produced solid carbon is estimated at \$0.633 kg^{-1} for a syncrude selling price of \$59.31 bbl^{-1} with natural gas and CO_2 costs at \$0.0939 std m^{-3} and \$70 ton^{-1}, respectively. The production cost of the plant's syncrude is estimated at \$137.06 bbl^{-1}, which is lower than the reported values by Zhang et al. to reform CO_2 to syncrude using hydrogen sourced from water electrolysis [31,42]. This reveals that the cost of hydrogen production has a vital role in the economic feasibility of CO_2 to GTL products. The CO_2-free hydrogen production by methane decomposition results in a less expensive syncrude when compared to those of processes that use water electrolysis to produce hydrogen from renewable electricity. The sensitivity analyses are performed to study the effect of the raw material costs and syncrude selling price on the NPW of the plant and breakeven price of the carbon. The NPW of the plant and breakeven price of the carbon is more sensitive to the selling price of syncrude than the raw materials. The economics of the GTL plants becomes more favourable at syncrude selling prices greater than \$80 bbl^{-1}. The ROI sensitivity analysis indicates that the selling price of carbon and syncrude has more effect on the profitability of the plant than the cost of raw materials. The comparison between the ROI of the present plant with SMR-FT and bi-reforming-FT plants indicates that under the same economic parameters, the present plant is more profitable than the SMR-FT and bi-reforming-FT plants especially when the cost of natural gas is less than \$ 2.91 $MMBTU^{-1}$.

The environmental performance of the plant is also evaluated in Chapter 4. Without considering upstream CO_2 emissions related to the supply chain of feed natural gas and CO_2, the GTL plant is the net consumer of CO_2. However, by considering the upstream CO_2 emission of the raw materials, the GTL plant emits 0.87 kg CO_2 per 1 kg of the produced syncrude or 19.92 gr CO_2 per 1 MJ of the produced syncrude. The present plant emits more CO_2 compared to water

electrolysis-FT plants. However, it shows the lowest CO_2 emissions when compared to natural gas-based GTL plants with and without carbon capture.

5.2. Recommendations

To improve the economics of the GTL plant, it is recommended to add atmospheric and vacuum distillation towers as well as a hydrocracker to fractionate the produced syncrude to value-added petroleum products such as liquefied petroleum gas, gasoline, and diesel. A thorough analysis of the required steam and hydrogen by the distillation towers and hydrocracker will be needed to update the CO_2 emissions of the plant when the syncrude is fractionated to other petroleum products.

In this thesis, the LTFT is used for the manufacturing of syncrude. It is also possible to explore replacing the LTFT reactor with an HTFT reactor to study the economic and environmental performance of the plant when syncrude is produced by high temperature FTS. HTFT Fe-based catalysts produce lighter hydrocarbons than LTFT catalysts, which might favour the economics of the plant. The HTFT catalysts also have water gas shift activity, which would allow feeding the FT reactor with syngas containing CO_2. This could potentially remove the need for the MEA unit or reduce the recycling demand of the RWGS reactor by separating less CO_2 in the MEA unit, which would eliminate or reduce the reboiler duty of the MEA regenerator column.

It is also recommended to explore CO_2 to GTL plants that include both LTFT and HTFT reactors to enhance the product diversity and to improve the economics of the plants.

References

[1] Greenhouse effects. https://doi.org/https://www.nrdc.org/stories/greenhouse-effect-101.

[2] F. Marocco Stuardi, F. MacPherson, J. Leclaire, Integrated CO_2 capture and utilization: A priority research direction, Curr. Opin. Green Sustain. Chem. 16 (2019) 71–76. https://doi.org/10.1016/j.cogsc.2019.02.003.

[3] D. Kweku, O. Bismark, A. Maxwell, K. Desmond, K. Danso, E. Oti-Mensah, A. Quachie, B. Adormaa, Greenhouse Effect: Greenhouse Gases and Their Impact on Global Warming, J. Sci. Res. Reports. 17 (2018) 1–9. https://doi.org/10.9734/jsrr/2017/39630.

[4] B. Metz, O. Davidson, H. De Coninck, M. Loos, L. Mayer, IPCC Special Report on Carbon Dioxide Capture and Storage, Cambrige University press, 1 st edition, 2005.

[5] N. Thonemann, M. Pizzol, Consequential life cycle assessment of carbon capture and utilization technologies within the chemical industry, Energy Environ. Sci. 12 (2019) 2253–2263. https://doi.org/10.1039/c9ee00914k.

[6] H. Mikulčić, I.R. Skov, D.F. Dominković, S.R. Wan Alwi, Z.A. Manan, R. Tan, N. Duić, S.N. Hidayah Mohamad, X. Wang, Flexible Carbon Capture and Utilization technologies in future energy systems and the utilization pathways of captured CO_2, Renew. Sustain. Energy Rev. 114 (2019). https://doi.org/10.1016/j.rser.2019.109338.

[7] R. Guettel, U. Kunz, T. Turek, Reactors for Fischer-Tropsch synthesis, Chem. Eng. Technol. 31 (2008) 746–754. https://doi.org/10.1002/ceat.200800023.

[8] H. Mahmoudi, M. Mahmoudi, O. Doustdar, H. Jahangiri, A. Tsolakis, S. Gu, M. LechWyszynski, A review of Fischer Tropsch synthesis process, mechanism, surface chemistry and catalyst formulation, Biofuels Eng. 2 (2018) 11–31. https://doi.org/10.1515/bfuel-2017-0002.

[9] B. Todic, Kinetic Modeling and Optimization of Fixed-Bed Reactor for Fischer- Tropsch Synthesis Pakovanim Slojem Za Fischer-, Belgr. Univ. (2015) 219.

[10] G.P. Van Der Laan, A.A.C.M. Beenackers, Kinetics and Selectivity of the Fischer-Tropsch Synthesis: A Literature Review, Catal. Rev. - Sci. Eng. 41 (1999) 255–318. https://doi.org/10.1081/CR-100101170.

[11] M. Luo, S. Bao, R.S. Keogh, A. Sarkar, G. Jacobs, B.H. Davis, Fischer Tropsch synthesis: A comparison of iron and cobalt catalysts, AIChE Annu. Meet. Conf. Proc. (2006) 8938–8945.

[12] A. De Klerk, Fischer-Tropsch Refining, University of Pretoria, (2008).

[13] S. Chambreya, P. Fongarlanda, H. Karacaa, S. Pichéa, A. Griboval-Constanta, D. Schweichb, F. Luckc, S. Savinc, A.Y. Khodakov, Fischer-Tropsch synthesis in milli-fixed bed reactor: Comparison with centimetric fixed bed and slurry stirred tank reactors, Catal. Today. 171 (2011) 201–206. https://doi.org/10.1016/j.cattod.2011.04.046.

[14] A. Tonkovich, T. Mazanec, K. Jarosch, Improved fischer-tropsch economics enabled by microchannel technology, Oxford Catal. (2008) 1–7.

[15] M.P. Rohde, D. Unruh, G. Schaub, Membrane application in Fischer-Tropsch synthesis reactors - Overview of concepts, Catal. Today. 106 (2005) 143–148. https://doi.org/10.1016/j.cattod.2005.07.124.

[16] Pierre Trambouze, Chemical Reactors, Editions Technip, 1 st edition, (2004).

[17] M. Pondini, M. Ebert, Process synthesis and design of low temperature Fischer-Tropsch crude production from biomass derived syngas, Dep. Energy Environ. (2013).

[18] H.S. Song, D. Ramkrishn, S. Trinh, H. Wright, Operating strategies for Fischer-Tropsch reactors: A model-directed study, Korean J. Chem. Eng. 21 (2004) 308–317. https://doi.org/10.1007/BF02705414.

[19] D. Förtsch, K. Pabst, E. Groß-Hardt, The product distribution in Fischer-Tropsch synthesis: An extension of the ASF model to describe common deviations, Chem. Eng. Sci. 138 (2015) 333–346. https://doi.org/10.1016/j.ces.2015.07.005.

[20] M. Marchese, N. Heikkinen, E. Giglio, A. Lanzini, J. Lehtonen, M. Reinikainen, Kinetic study based on the carbide mechanism of a Co-pt/γ-Al_2O_3 fischer–tropsch catalyst tested in a laboratory-scale tubular reactor, Catalysts. 9 (2019). https://doi.org/10.3390/catal9090717.

[21] B. Todic, T. Bhatelia, G.F. Froment, W. Ma, G. Jacobs, B.H. Davis, D.B. Bukur, Kinetic model of Fischer-Tropsch synthesis in a slurry reactor on Co-Re/Al_2O_3 catalyst, Ind. Eng. Chem. Res. 52 (2013) 669–679. https://doi.org/10.1021/ie3028312.

[22] Hazel C. Anderson, Bibliography of the Fischer-Tropsch Synthesis and Related Processes: Review and compilation of the literature on the production of synthetic liquid fuels and chemicals by the hydrogenation of carbon monoxide, U.S. Government Printing Office, 1 st edition, (1954).

[23] Shell (Pearl GTL overview). https://www.shell.com/about-us/major-projects/pearl-gtl/pearl-gtl-an-overview.html.

[24] Y. Zhang, A.H. Sahir, E.C.D. Tan, M.S. Talmadge, R. Davis, M.J. Biddy, L. Tao, Economic and environmental potentials for natural gas to enhance biomass-to-liquid fuels technologies, Green Chem. 20 (2018) 5358–5373. https://doi.org/10.1039/c8gc01257a.

[25] J.E.A. Graciano, B. Chachuat, R.M.B. Alves, Conversion of CO_2-Rich Natural Gas to Liquid Transportation Fuels via Trireforming and Fischer-Tropsch Synthesis: Model-Based Assessment, Ind. Eng. Chem. Res. 57 (2018) 9964–9976. https://doi.org/10.1021/acs.iecr.8b00135.

[26] J. Na, K.S. Kshetrimayum, I. Jung, S. Park, Y. Lee, O. Kwon, Y. Mo, J. Chung, J. Yi, U. Lee, C. Han, Optimal design and operation of Fischer-Tropsch microchannel reactor for pilot-scale compact Gas-to-Liquid process, Chem. Eng. Process. - Process Intensif. 128 (2018) 63–76. https://doi.org/10.1016/j.cep.2018.04.013.

[27] B. Hernandez, M. Martin, Optimization for biogas to chemicals via tri-reforming. Analysis of Fischer-Tropsch fuels from biogas, Energy Convers. Manag. 174 (2018) 998–1013. https://doi.org/10.1016/j.enconman.2018.08.074.

[28] Z. Arab Aboosadi, A.H. Jahanmiri, M.R. Rahimpour, Optimization of tri-reformer reactor to produce synthesis gas for methanol production using differential evolution (DE) method, Appl. Energy. 88 (2011) 2691–2701. https://doi.org/10.1016/j.apenergy.2011.02.017.

[29] C. Zhang, K.W. Jun, R. Gao, G. Kwak, S.C. Kang, Efficient utilization of associated natural gas in a modular gas-to-liquids process: Technical and economic analysis, Fuel. 176 (2016) 32–39. https://doi.org/10.1016/j.fuel.2016.02.060.

[30] S. Adelung, S. Maier, R.U. Dietrich, Impact of the reverse water-gas shift operating conditions on the Power-to-Liquid process efficiency, Sustain. Energy Technol. Assessments. 43 (2021) 100897. https://doi.org/10.1016/j.seta.2020.100897.

[31] R. Gao, C. Zhang, K.W. Jun, S.K. Kim, H.G. Park, T. Zhao, L. Wang, H. Wan, G. Guan, Transformation of CO_2 into liquid fuels and synthetic natural gas using green hydrogen: A comparative analysis, Fuel. 291 (2021) 120111. https://doi.org/10.1016/j.fuel.2020.120111.

[32] D.H. König, N. Baucks, R.U. Dietrich, A. Wörner, Simulation and evaluation of a process concept for the generation of synthetic fuel from CO_2 and H_2, Energy. 91 (2015) 833–841. https://doi.org/10.1016/j.energy.2015.08.099.

[33] G. Zang, P. Sun, A.A. Elgowainy, A. Bafana, M. Wang, Performance and cost analysis of liquid fuel production from H2and CO_2 based on the Fischer-Tropsch process, J. CO_2 Util. 46 (2021) 101459. https://doi.org/10.1016/j.jcou.2021.101459.

[34] D.H. Kim, J.L. Park, E.J. Park, Y.D. Kim, S. Uhm, Dopant Effect of Barium Zirconate-Based Perovskite-Type Catalysts for the Intermediate-Temperature Reverse Water Gas Shift Reaction, ACS Catal. 4 (2014) 3117–3122. https://doi.org/10.1021/cs500476e.

[35] C.M. Liu, N.K. Sandhu, S.T. McCoy, J.A. Bergerson, A life cycle assessment of greenhouse gas emissions from direct air capture and Fischer-Tropsch fuel production, Sustain. Energy Fuels. 4 (2020) 3129–3142. https://doi.org/10.1039/c9se00479c.

[36] M. Fasihi, D. Bogdanov, C. Breyer, Techno-Economic Assessment of Power-to-Liquids (PtL) Fuels Production and Global Trading Based on Hybrid PV-Wind Power Plants, Energy Procedia. 99 (2016) 243–268. https://doi.org/10.1016/j.egypro.2016.10.115.

[37] M. Marchese, G. Buffo, M. Santarelli, A. Lanzini, CO_2 from direct air capture as carbon feedstock for Fischer-Tropsch chemicals and fuels: Energy and economic analysis, J. CO_2 Util. 46 (2021) 101487. https://doi.org/10.1016/j.jcou.2021.101487.

[38] S. Brynolf, M. Taljegard, M. Grahn, J. Hansson, Electrofuels for the transport sector: A review of production costs, Renew. Sustain. Energy Rev. 81 (2018) 1887–1905. https://doi.org/10.1016/j.rser.2017.05.288.

[39] M. Marchese, E. Giglio, M. Santarelli, A. Lanzini, Energy performance of Power-to-Liquid applications integrating biogas upgrading, reverse water gas shift, solid oxide electrolysis and Fischer-Tropsch technologies, Energy Convers. Manag. X. 6 (2020) 100041. https://doi.org/10.1016/j.ecmx.2020.100041.

[40] C. Graves, S.D. Ebbesen, M. Mogensen, K.S. Lackner, Sustainable hydrocarbon fuels by

recycling CO_2 and H 2O with renewable or nuclear energy, Renew. Sustain. Energy Rev. 15 (2011) 1–23. https://doi.org/10.1016/j.rser.2010.07.014.

[41] C. Zhang, R. Gao, K.W. Jun, S.K. Kim, S.M. Hwang, H.G. Park, G. Guan, Direct conversion of carbon dioxide to liquid fuels and synthetic natural gas using renewable power: Techno-economic analysis, J. CO_2 Util. 34 (2019) 293–302. https://doi.org/10.1016/j.jcou.2019.07.005.

[42] T.N. Do, J. Kim, Green C_2-C_4 hydrocarbon production through direct CO_2 hydrogenation with renewable hydrogen: Process development and techno-economic analysis, Energy Convers. Manag. 214 (2020) 112866. https://doi.org/10.1016/j.enconman.2020.112866.

[43] C. Panzone, R. Philippe, A. Chappaz, P. Fongarland, A. Bengaouer, Power-to-Liquid catalytic CO_2 valorization into fuels and chemicals: Focus on the Fischer-Tropsch route, J. CO_2 Util. 38 (2020) 314–347. https://doi.org/10.1016/j.jcou.2020.02.009.

[44] L.J.J. Catalan, E. Rezaei, ScienceDirect Modelling the hydrodynamics and kinetics of methane decomposition in catalytic liquid metal bubble reactors for hydrogen production, Int. J. Hydrogen Energy. (2021). https://doi.org/10.1016/j.ijhydene.2021.12.089.

[45] Rajabhau Bajirao Unde, Kinetics and reaction engineering aspects of syngas production by the heterogeneously catalysed RWGS, University of Bayreuth, (2012).

[46] T.A. Adams, P.I. Barton, A dynamic two-dimensional heterogeneous model for water gas shift reactors, Int. J. Hydrogen Energy. 34 (2009) 8877–8891. https://doi.org/10.1016/j.ijhydene.2009.08.045.

[47] F. Ghodoosi, M.R. Khosravi-Nikou, A. Shariati, Mathematical Modeling of Reverse Water-Gas Shift Reaction in a Fixed-Bed Reactor, Chem. Eng. Technol. 40 (2017) 598–607. https://doi.org/10.1002/ceat.201600220.

[48] S. Dzuryk, E. Rezaei, Intensification of the Reverse Water Gas Shift Reaction by Water-Permeable Packed-Bed Membrane Reactors, Ind. Eng. Chem. Res. 59 (2020) 18907–18920. https://doi.org/10.1021/acs.iecr.0c02213.

[49] Carl Yaws, Thermophysical properties of chemicals and hydrocarbons, Gulf Professional, 2nd edition, (2014).

[50] I.C. Yates, C.N. Satterfield, Intrinsic Kinetics of the Fischer-Tropsch Synthesis on a Cobalt Catalyst, Energy and Fuels. 5 (1991) 168–173. https://doi.org/10.1021/ef00025a029.

[51] W. Ma, G. Jacobs, T. K.Das, C. M. Masuku, J. Kang,V. Ramana Rao Pendyala, B. H. Davis, J. Klettlinger, and C.H. Yen, Fischer-Tropsch Synthesis: kinetics and Water effect on Methane Formation over Co-Al2O3 Catalyst, I& EC research, Volume 53, 2157–2166, (2014).

[52] B. Todic, M. Mandic, N. Nikacevic, D.B. Bukur, Effects of process and design parameters on heat management in fixed bed Fischer-Tropsch synthesis reactor, Korean J. Chem. Eng. 35 (2018) 875–889. https://doi.org/10.1007/s11814-017-0335-3.

[53] M. Mandić, B. Todić, L. Živanić, N. Nikačević, D.B. Bukur, Effects of Catalyst Activity,

Particle Size and Shape, and Process Conditions on Catalyst Effectiveness and Methane Selectivity for Fischer-Tropsch Reaction: A Modeling Study, Ind. Eng. Chem. Res. 56 (2017) 2733–2745. https://doi.org/10.1021/acs.iecr.7b00053.

[54] J.J. Marano, G.D. Holder, Characterization of Fischer-Tropsch liquids for vapor-liquid equilibria calculations, Fluid Phase Equilib. 138 (1997) 1–21. https://doi.org/10.1016/s0378-3812(97)00166-0.

[55] E. Rezaei, L.J.J. Catalan, Evaluation of CO_2 utilization for methanol production via tri-reforming of methane, J. CO_2 Util. 42 (2020) 101272. https://doi.org/10.1016/j.jcou.2020.101272.

[56] R. Smith, Chemical process design and integration, Wiley & Sons, 2nd edition, 2016.

[57] R. Turton, J.A. Shaeiwitz, D. Bhattacharyya, Analysis, Synthesis, and Design of Chemical processes, Pennwell Corp, Volume 2, 1 st edition, 1995, Pearson education. 5th edition, 2018.

[58] M. Luberti, Design of a H_2 Pressure Swing Adsorption process at an advanced IGCC plant for cogenerating hydrogen and power with CO_2 capture, University of Edinburgh, (2015).

[59] K.M.N. Warren D. Seider, Daniel R. Lewin, J. D. Seader, Soemantri Widagdo, Rafiqul Gani, Product and Process Design Principles: Synthesis, Analysis and Evaluation, Wiley, 4th edition, (2016).

[60] B.J. Leal Pérez, J.A. Medrano Jiménez, R. Bhardwaj, E. Goetheer, M. van Sint Annaland, F. Gallucci, Methane pyrolysis in a molten gallium bubble column reactor for sustainable hydrogen production: Proof of concept & techno-economic assessment, Int. J. Hydrogen Energy. 46 (2021) 4917–4935. https://doi.org/10.1016/j.ijhydene.2020.11.079.

[61] R.M. Swanson, A. Platon, J.A. Satrio, R.C. Brown, Techno-economic analysis of biomass-to-liquids production based on gasification scenarios, ACS Natl. Meet. B. Abstr, 32-33, (2009).

[62] G.A. Von Wald, M.S. Masnadi, D.C. Upham, A.R. Brandt, Optimization-based technoeconomic analysis of molten-media methane pyrolysis for reducing industrial sector CO_2 emissions, Sustain. Energy Fuels. 4 (2020) 4598–4613. https://doi.org/10.1039/d0se00427h.

[63] Natural Resources Canada Government Department. https://www.nrcan.gc.ca/our-natural-resources/minerals-mining/minerals-metals-facts/copper-facts/20506.

[64] Made-In-China. https://paizhe.en.made-in-china.com/product/zdyaLNbcMUVC/China-Hot-Sale-Sodium-Bromide-with-Best-Price.html.

[65] Natural Resources Canada, Oil Pricing. https://www.nrcan.gc.ca/our-natural-resources/energy-sources-distribution/clean-fossil-fuels/crude-oil/oil-pricing/18087.

[66] E.E. Ludwing, Applied process design for chemical and petrochemical plants, Gulf

Professional, Volume 1, 3th edition, 1999.

[67] N. Rahimi, D. Kang, J. Gelinas, A. Menon, M.J. Gordon, H. Metiu, E.W. McFarland, Solid carbon production and recovery from high temperature methane pyrolysis in bubble columns containing molten metals and molten salts, Carbon N. Y. 151 (2019) 181–191. https://doi.org/10.1016/j.carbon.2019.05.041.

[68] R.A. Dagle, V. Dagle, M.D. Bearden, J.D. Holladay, T.R. Krause, S. Ahmed, An Overview of Natural Gas Conversion Technologies for Co-Production of Hydrogen and Value-Added Solid Carbon Products, (No. PNNL-26726; ANL-17/11). Pacific Northwest Natl. Lab.(PNNL), Richland, WA (United States); Argonne Natl. Lab.(ANL), Argonne, (United States). (2017) 65. http://www.osti.gov/servlets/purl/1411934/.

[69] N. Von Der Assen, L.J. Müller, A. Steingrube, P. Voll, A. Bardow, Selecting CO_2 Sources for CO_2 Utilization by Environmental-Merit-Order Curves, Environ. Sci. Technol. 50 (2016) 1093–1101. https://doi.org/10.1021/acs.est.5b03474.

[70] A.P. Steynberg, H.G. Nel, Clean coal conversion options using Fischer-Tropsch technology, Fuel. 83 (2004) 765–770. https://doi.org/10.1016/j.fuel.2003.09.023.

[71] R.E.T. Francis S. Manning, Oilfield Processing: Crude Oil, Pennwell Corp, 1 st edition, (1995).

[72] A. Rafiee, M. Panahi, K.R. Khalilpour, CO2 utilization through integration of post-combustion carbon capture process with Fischer-Tropsch gas-to-liquid (GTL) processes, J. CO2 Util. 18 (2017) 98–106. https://doi.org/10.1016/j.jcou.2017.01.016.

Appendix A. Validation of the kinetics of the FT reaction

The FT kinetics is validated for an experimental slurry-bed reactor and a theoretical packed-bed reactor, explained in Sections A.1 and A.2, respectively.

A.1. Validation using experimental data of a slurry-bed reactor

The FT kinetic equations, which are presented in section 3.5.2, are used to validate the kinetics of the Re-Co/Al_2O_3 catalyst against the experimental data of a slurry-bed reactor reported by Todic [9]. The formation rate of alkanes, alkenes, and total hydrocarbons as well as alkenes to alkanes ratios are simulated in MATLAB and the results are depicted in Figs. A1 and A2. The product distributions are modelled at different temperatures, pressures, H_2/CO ratios, and weight hourly space velocities (WHSVs). As seen in Figs. A1 and A2, the results from the MATLAB simulation are in good agreement with the experimental data reported by Todic.

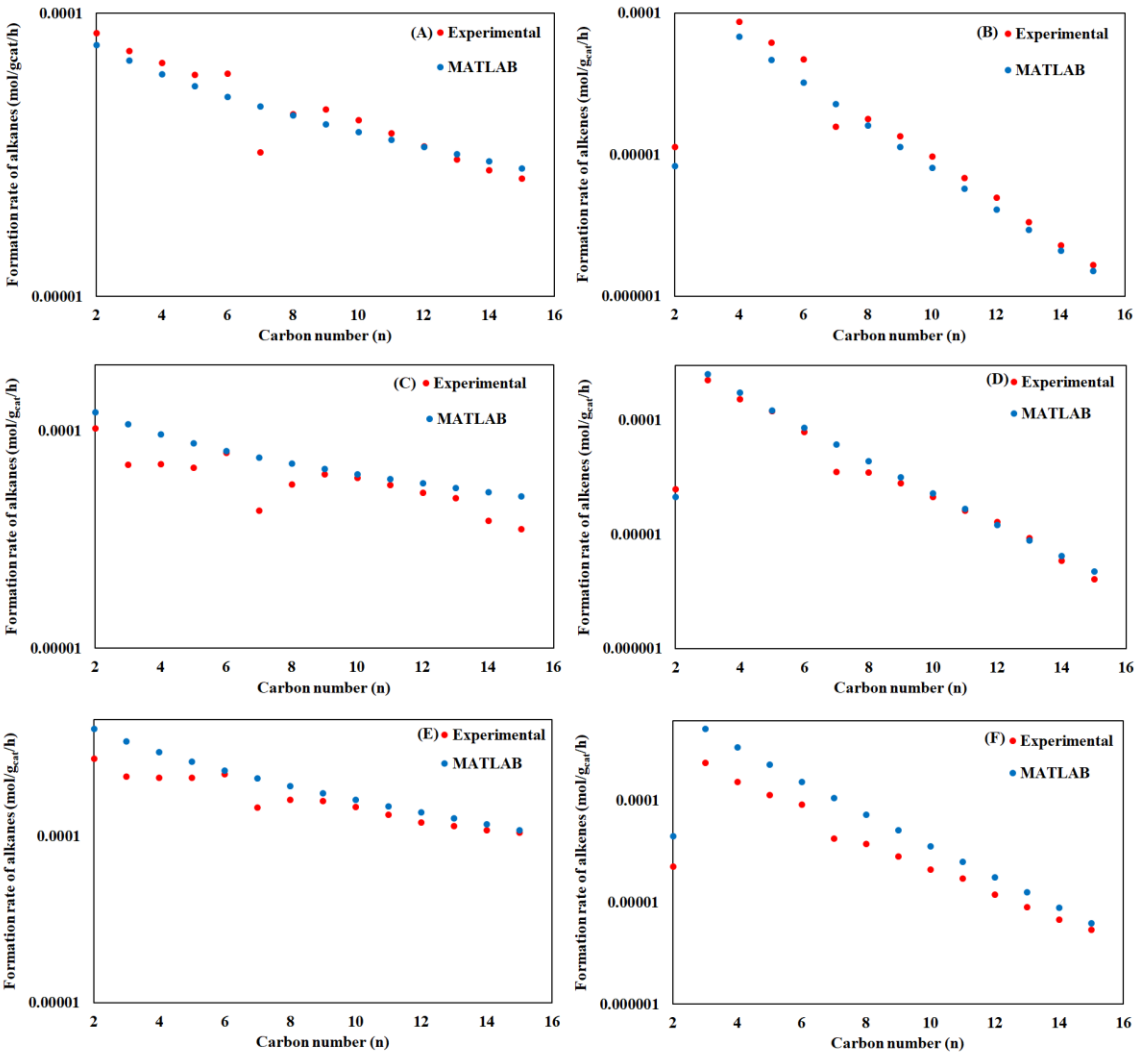

Fig. A.1. Formation rate of alkanes (left panel) and alkenes (right panel) for the Re-Co/Al_2O_3 catalyst, (A) and (B) T=478 K, P=1.5 MPa, H_2/CO=2.1, WHSV= 3.7 NL $g_{cat}^{-1}h^{-1}$, (C) and (D) T=493 K, P=2.5 MPa, H_2/CO=2.1, WHSV= 6.1 NL $g_{cat}^{-1}h^{-1}$, (E) and (F) T=503 K, P=2.5 MPa, H_2/CO=2.1, WHSV= 11.5 NL $g_{cat}^{-1}h^{-1}$ [9].

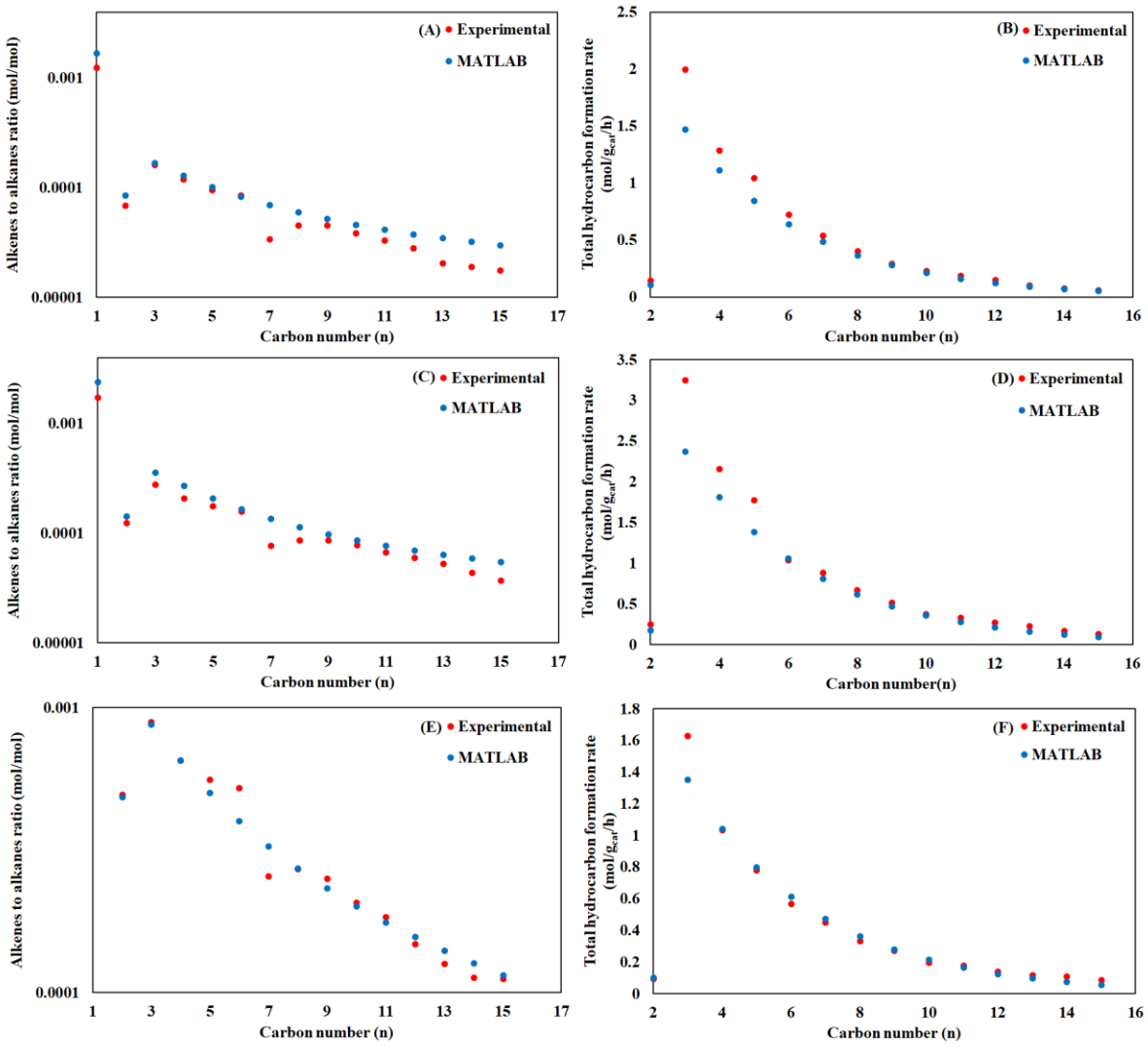

Fig. A.2. Alkenes to alkanes ratios (left panel) and total hydrocarbon formation rate (right panel) for the Re-Co/Al_2O_3 catalyst, (A) and (B) T=478 K, P=1.5 MPa, H_2/CO=2.1, WHSV= 3.7 NL $g_{cat}^{-1}h^{-1}$, (C) and (D) T=493 K, P=2.5 MPa, H_2/CO=2.1, WHSV= 6.1 NL $g_{cat}^{-1}h^{-1}$, (E) and (F) T=503 K, P=2.5 MPa, H_2/CO=2.1, WHSV= 11.5 NL $g_{cat}^{-1}h^{-1}$[9].

A.2. Validation using simulation results of a packed-bad reactor

A one-dimensional FT reactor with one tube is simulated according to the data from Todic et al. [52]. A syngas with an H_2/CO ratio of 2.1 enters the FT reactor at 478 K and 2.5 MPa with a molar flowrate of 1.5 mol s^{-1}. The catalyst is the same Re-Co/Al_2O_3 catalyst used in Appendix A.1 with particle diameter and catalyst density of 0.002 m and 1200 kg m^{-3}, respectively. The FT reactor is modelled as a packed-bed reactor with a diameter and length of 0.026 m and 10 m, respectively. The simulation is limited to the production of 57 normal paraffines and 56 alpha olefines. The reactor is modelled based on the governing differential equations explained in Sections 3.5.3. Table A.1 shows that the predicted CO conversion, C5 plus selectivity, C5 plus molar flow rate, and pressure drop of the reactor are very close to the simulation results reported by Todic et al. Figure A.3 shows that the temperature profile of the reactor obtained by MATALB is also in good agreement with the temperature profile reported by Todic et al. with a maximum of 2 ^oC difference.

Table A1. Comparison between the simulation results of this work and those of Todic et al. [52]

Results	**CO conversion (%)**	**Pressure drop (bar)**	**S_{5+} selectivity (%)**	**C_{5+} molar flow rate (mol s^{-1})**
MATLAB	28	1.8	87	6.13×10^{-4}
Todic et al	29.12	2.033	86.84	6.278×10^{-4}

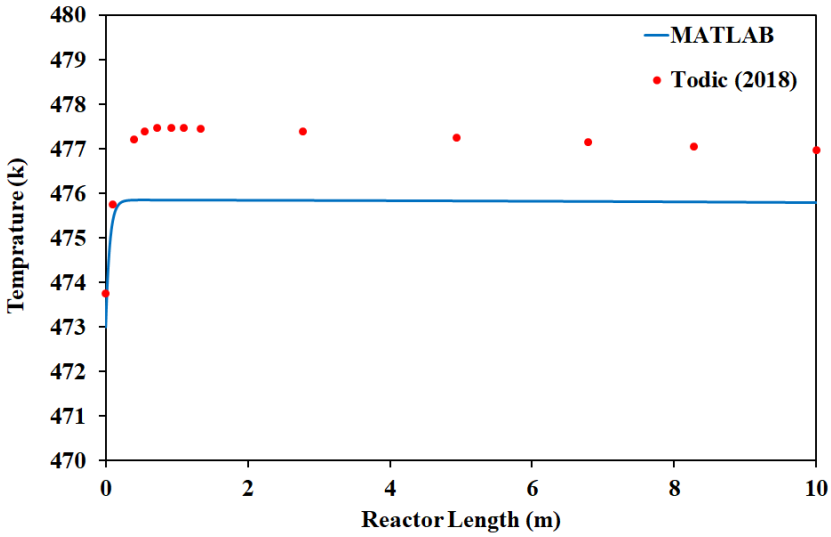

Fig. A.3. Comparison of the temperature profile of the FT reactor with that of Todic et al. [52]

Appendix B: Validation of the kinetics of the RWGS reaction

The validation of the kinetics of the RWGS reaction is done under adiabatic condition using the simulation results reported by Unde [45].

B.1. Validation under adiabatic conditions

An adiabatic RWGS reactor is simulated to reproduce the results of a packed-bed reactor reported by Unde for the Ni-$Al_{12}O_{19}$ catalyst [45]. The simulation is based on the governing differential equations of the RWGS reactor explained Section 3.4.2. The reactor temperature and CO_2 conversion profiles are depicted for three inlet superficial velocities at 0.5, 5, and 15 m s^{-1} to validate the kinetics of the catalyst. The RWGS reactor has a diameter of 0.02 m and a length of 0.5 m. The catalyst particle diameter and bulk density is equal to 0.006 m 1200 kg m^{-3}, respectively. The feed enters the reactor with H_2/CO_2 ratio of 3 at 1200 °C and 100 kPa. Fig. A4 presents the comparison of the simulation results of this work and those of Unde. The simulation results from MATLAB are close to the data reported by Unde.

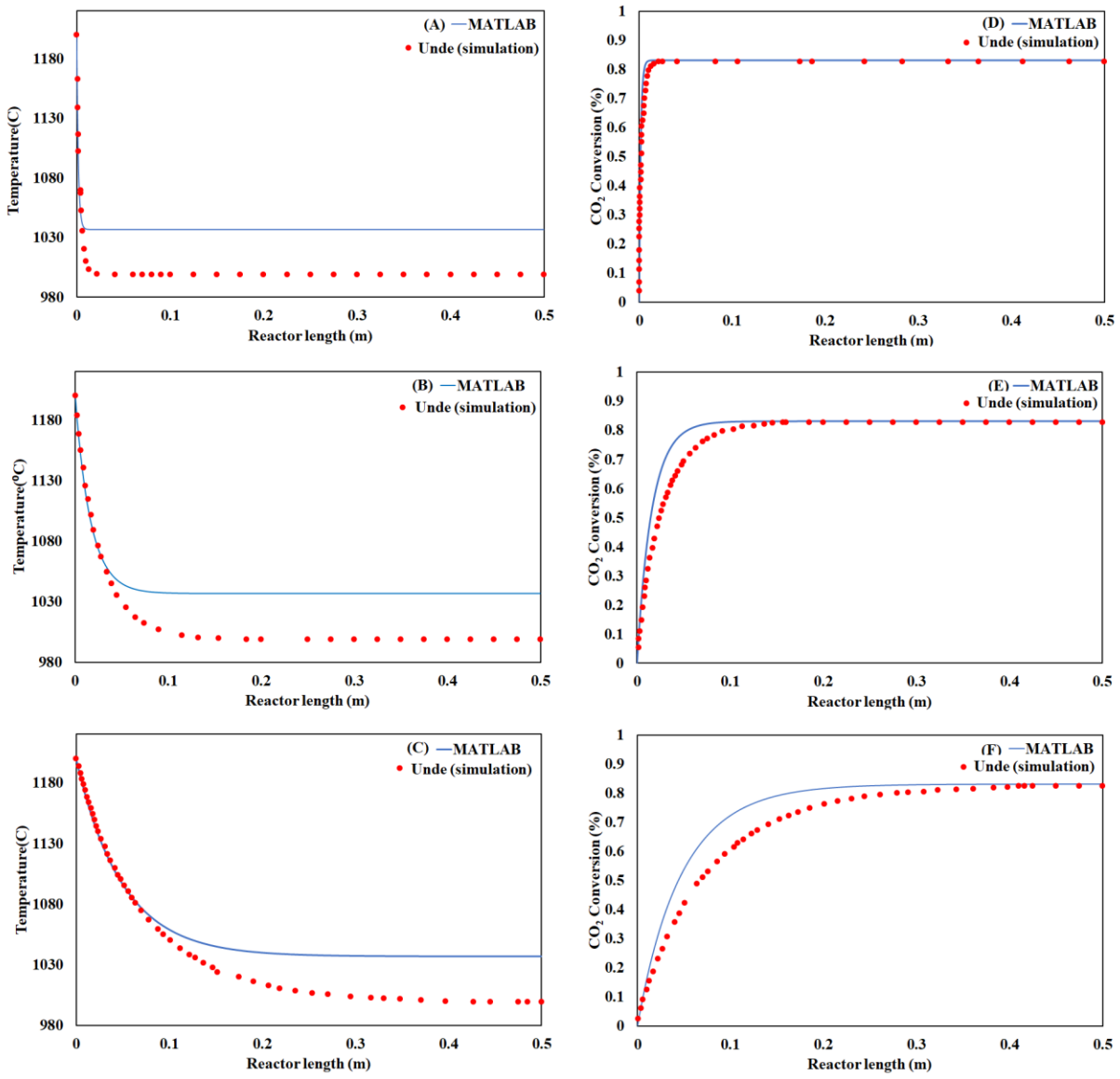

Fig. B.1. Temperature (left panel) and CO_2 conversion (right panel) profiles of the Ni-$Al_{12}O_{19}$ catalyst under adiabatic conditions, (A) and (D) inlet superficial velocity = 0.5 m s^{-1}, (B) and (E) inlet superficial velocity = 1 m s^{-1}, and (C) and (F) inlet superficial velocity = 1.5 m s^{-1}.

Appendix C: Sizing of two- and three-phase separators

C.1. Two-phase separators

The calculations related to the sizing of the two-phase separators are based on Turton et al. [57]. The separators are considered as vertical vapor-liquid vane type vessels containing a mist eliminator to minimize the diameter of the vessels. The equations to size the vessels are expressed by Eqs. (C-1) to (C-5):

$$U_{Max} = K_{SB}\sqrt{\frac{\rho_l - \rho_V}{\rho_V}} \qquad (C-1)$$

$$U_g = 0.8 \times U_{Max} \qquad (C-2)$$

$$D_{ves} = \sqrt{\frac{4 \times Q_g}{\pi \times U_g}} \qquad (C-3)$$

$$Q_g \times t_r = \frac{\pi}{4} \times D_{ves}^2 \times L_L \qquad (C-4)$$

$$L_{ves} = LLAL + L_L + 0.3 \times D_{ves} + 0.45 \times D_{ves} + L_{Pad} + 0.15 \times D_{ves} \qquad (C-5)$$

in which K_{SB} (m s^{-1}) is Souders-Brown parameter, which is assumed to be 0.35 for a vertical flow vane type (style 350) mist eliminator [57], U_{max} (m s^{-1}) is the maximum allowable vapor velocity, ρ_l (kg m^{-3}) is the liquid density, ρ_V (kg m^{-3}) is the vapor density, Q_g (m^3 s^{-1}) is the vapor flow rate, D_{ves} (m) is the diameter of the vessel, t_r (s) is the liquid retention time in the vessel, which is assumed to be 20 min, L_L (m) is the height of the liquid in the vessel, which is calculated based on the retention time of liquid, L_{ves} (m) is the height of the vessel, LLAL is the low-low alarm level,

which is equal to 0.2 m, and L_{Pad} (m) is the thickness of the demister pad which is assumed to be 0.1.

C.2. Three-phase separators

Three-phase separators are designed as horizontal vapor-liquid separators with a vane type demister to allow higher gas flow rates in the vessels while keeping the diameter of the entrained oil and water droplets smaller than 100 microns. The sizing of the three-phase separators is based on Souders-Brown equations from Manning and Turton which are expressed by Eqs. (C-6) to (C-14) [57,71]. It is assumed that the length to diameter (L/D) of the vessels is equal to 3 and the liquid height in the vessels is 0.8 of their diameter (H_L=0.8× D_{ves}).

$$U_{Max} = K_{SB}\sqrt{\frac{\rho_o - \rho_V}{\rho_V}} \qquad (C-6)$$

$$U_g = 0.8 \times U_{Max} \qquad (C-7)$$

$$A_Z = Q_g \times U_g \qquad (C-8)$$

$$H_L = \frac{D_{ves}}{2}\left[1 - \cos\left(\frac{\theta}{2}\right)\right] \qquad (C-9)$$

$$A_Z = \frac{D_{ves}^2}{8}\left[2\pi - \theta - \sin\theta\right] \qquad (C-10)$$

$$A_L = A_{Oil} + A_{water} = \frac{\pi D_{ves}^2}{4} - A_Z \qquad (C-11)$$

$$(Q_W + Q_O) \times t_r = A_L \times L \qquad (C-12)$$

$$Q_O \times t_r = A_O \times L \qquad (C-13)$$

$$Q_W \times t_r = A_W \times L \qquad (C-14)$$

in which K_{SB} (m s^{-1}) is Souders-Brown parameter, which is assumed to be 0.35 for a horizontal flow vane type (style 250) mist eliminator [57], A_Z (m^2) is the cross-sectional area through which gases flows, H_L (m) is the liquid height in the vessel, A_L (m^2) is the cross section area through which liquid phases (oil and water) flow, A_W (m^2) is the cross section area through which water flows, A_{Oil} (m^2) is the cross section area through which oil flows, Q_W (m^3 s^{-1}) is the volumetric flow rate of water, Q_O (m^3 s^{-1}) is the volumetric flow rate of oil, and t_r (s) is the liquid retention time.

The droplet sizes of water in oil and oil in water are calculated by Eqs. (C-15) to (C-18) [65].

$$V_{wd} = \frac{H_L - H_{o/w}}{t_r} \qquad (C-15)$$

$$V_{od} = \frac{H_{o/w}}{t_r} \qquad (C-16)$$

$$D_{wd} = \sqrt{\frac{18 \times V_{wd} \times \mu_o}{(\rho_w - \rho_o) \times g}} \qquad (C-17)$$

$$D_{od} = \sqrt{\frac{18 \times V_{od} \times \mu_w}{(\rho_w - \rho_o) \times g}} \qquad (C-18)$$

where $H_{O/W}$ (m) is the height of water in the vessel, which is calculated from data provided in Manning for $\frac{H_{O/W}}{D_{ves}}$ as a function of $\frac{A_W}{A_L}$. V_{wd} (m s^{-1}) is the dynamic velocity of water droplet, V_{od} (m s^{-1}) is the dynamic velocity of oil droplet, g (9.81 m s^{-2}) is the gravitational acceleration, D_{wd} (micron) is the diameter of water droplets in oil, D_{od} (micron) is the diameter of oil droplets in water, μ_w (Pa.s) is the water viscosity, μ_o (Pa.s) is the oil viscosity, ρ_w (kg m^{-3}) is the density of water, and ρ_o (kg m^{-3}) is the oil density. It should be noted that Eqs. (C-17) and (C-18) are valid

when the oil and water droplet Reynolds numbers are between 0 and 2 [32]. The water and oil droplet Reynolds numbers are given by Eqs. (C-19) and (C-20), respectively.

$$\mathrm{Re}_{wd} = \frac{\mathrm{D_{wd}} \times \mathrm{V_{wd}} \times \rho_{\mathrm{o}}}{\mu_{\mathrm{o}}} \qquad (\mathrm{C}-19)$$

$$\mathrm{Re}_{od} = \frac{\mathrm{D_{od}} \times \mathrm{V_{od}} \times \rho_{\mathrm{w}}}{\mu_{\mathrm{w}}} \qquad (\mathrm{C}-20)$$

The physical properties of gas, water, and oil phases are taken from Aspen HYSYS. To avoid excessive gas flow rates and large vessel diameters, instead of one vessel, parallel three- and two-phase separators are used in this work. It is worth mentioning that the oil and water retention times in three-phase separators are greater than 30 min.

Appendix D: Stream summary tables

List of tables:

Table D.1. Process stream summary table (CH_4 decomposition unit)

Stream Number	1	2	3	4	5	6	7	8	9	10	11	12
Vapour Fraction	1	0.9611	1	1	1	0	0.8618	1	1	1	1	1
Temperature (°C)	5	-73.64	-3.271	`800	677.4	677.4	677.4	1100	366.6	48	132	40
Pressure (kPa)	8000	1928	1921	1900	1900	1900	1900	1844	1833	1824	3390	3381
Molar Flow (kmol/h)	23560	23560	23560	23560	28060	4500	32560	44780	44780	44780	44780	44780
Mole Fraction												
CH_4	0.8871	0.8871	0.8871	0.8871	0.7448	0.0000	0.6419	0.0933	0.0933	0.0933	0.0933	0.0933
C_2H_6	0.0693	0.0693	0.0693	0.0693	0.0000	0.0000	0.0000	0.0000	0.0000	0.0000	0.0000	0.0000
C_3H_8	0.0125	0.0125	0.0125	0.0125	0.0000	0.0000	0.0000	0.0000	0.0000	0.0000	0.0000	0.0000
n-C_4H_{10}	0.0028	0.0028	0.0028	0.0028	0.0000	0.0000	0.0000	0.0000	0.0000	0.0000	0.0000	0.0000
n-C_5H_{12}	0.0005	0.0005	0.0005	0.0005	0.0000	0.0000	0.0000	0.0000	0.0000	0.0000	0.0000	0.0000
n-C_6H_{14}	0.0002	0.0002	0.0002	0.0002	0.0000	0.0000	0.0000	0.0000	0.0000	0.0000	0.0000	0.0000
N_2	0.0082	0.0082	0.0082	0.0082	0.0069	0.0000	0.0059	0.0043	0.0043	0.0043	0.0043	0.0043
O_2	0.0000	0.0000	0.0000	0.0000	0.0000	0.0000	0.0000	0.0000	0.0000	0.0000	0.0000	0.0000
H_2O	0.0000	0.0000	0.0000	0.0000	1.0000	0.9998	0.0000	0.0000	0.0000	0.0000	0.0000	0.0000
CO_2	0.0194	0.0194	0.0194	0.0194	0.0163	0.0002	0.0140	0.0102	0.0102	0.0102	0.0102	0.0102
CO	0.0000	0.0000	0.0000	0.0000	0.0000	0.0000	0.0000	0.0000	0.0000	0.0000	0.0000	0.0000
MEA	0.0000	0.0000	0.0000	0.0000	0.0000	0.0000	0.0000	0.0000	0.0000	0.0000	0.0000	0.0000
H_2	0.0000	0.0000	0.0000	0.0000	0.2320	0.0000	0.1999	0.8921	0.8921	0.8921	0.8921	0.8921
C	0.0000	0.0000	0.0000	0.0000	0.0000	1.0000	0.1382	0.0000	0.0000	0.0000	0.0000	0.0000

Continued…

Table D.1. Process stream summary table (CH_4 decomposition unit)

Stream Number	13	13(a)	13(b)	13(c)	13(d)	14	15	16	17	18	19	20	ToRWGS
Vapour Fraction	1	1	1	1	1	1	0.0359	0.9711	1	1	1	1	1
Temperature (°C)	39.34	39.34	39.34	39.37	200	5	0.936	-50.96	30	155.6	155	870	1023
Pressure (kPa)	3361	3361	3361	2521	2500	8000	3361	3361	3339	3319	3319	3303	3303
Molar Flow (kmol/h)	37170	37020	144	144	144	12250	12250	49270	49270	49270	52310	52310	52310
Mole Fraction													
CH_4	0.0000	0.0000	0.0000	0.0000	0.0000	0.0000	0.0000	0.0000	0.0000	0.0000	0.0000	0.0000	0.0000
C_2H_6	0.0000	0.0000	0.0000	0.0000	0.0000	0.0000	0.0000	0.0000	0.0000	0.0000	0.0000	0.0000	0.0000
C_3H_8	0.0000	0.0000	0.0000	0.0000	0.0000	0.0000	0.0000	0.0000	0.0000	0.0000	0.0000	0.0000	0.0000
n-C_4H_{10}	0.0000	0.0000	0.0000	0.0000	0.0000	0.0000	0.0000	0.0000	0.0000	0.0000	0.0000	0.0000	0.0000
n-C_5H_{12}	0.0000	0.0000	0.0000	0.0000	0.0000	0.0000	0.0000	0.0000	0.0000	0.0000	0.0000	0.0000	0.0000
n-C_6H_{14}	0.0000	0.0000	0.0000	0.0000	0.0000	0.0000	0.0000	0.0000	0.0000	0.0000	0.0000	0.0000	0.0000
N_2	0.0003	0.0003	0.0003	0.0003	0.0003	0.0000	0.0000	0.0002	0.0002	0.0002	0.0002	0.0002	0.0002
O_2	0.0000	0.0000	0.0000	0.0000	0.0000	0.0000	0.0000	0.0000	0.0000	0.0000	0.0000	0.0000	0.0000
H_2O	0.0000	0.0000	0.0000	0.0000	0.0000	0.0000	0.0000	0.0000	0.0000	0.0000	0.0007	0.0007	0.0007
CO_2	0.9997	0.9997	0.9997	0.9997	0.9997	1.0000	1.0000	0.2486	0.2486	0.2486	0.2901	0.2901	0.2901
CO	0.0000	0.0000	0.0000	0.0000	0.0000	0.0000	0.0000	0.0000	0.0000	0.0000	0.0004	0.0004	0.0004
MEA	0.0000	0.0000	0.0000	0.0000	0.0000	0.0000	0.0000	0.0000	0.0000	0.0000	0.0000	0.0000	0.0000
H_2	0.0000	0.0000	0.0000	0.0000	0.0000	0.0000	0.0000	0.7512	0.7512	0.7512	0.7085	0.7085	0.7085
C	0.0000	0.0000	0.0000	0.0000	0.0000	0.0000	0.0000	0.0000	0.0000	0.0000	0.0000	0.0000	0.0000

Table D.2. Process stream summary table (RWGS unit)

Stream Number	21	22	23	24	25	26	27	28	29	30	31
Vapour Fraction	1	1	0.9414	0.9010	0.7734	1	1	0	0	0.0034	1
Temperature (°C)	1022	285.1	154.1	145.1	50.63	50.63	50.34	62.14	95.50	93.97	51.28
Pressure (kPa)	3242	3222	3212	3175	3147	3147	3000	3200	3194	200	200
Molar Flow (kmol/h)	52310	52310	52310	52310	52310	40460	37420	227600	227600	227600	3159
Mole Fraction											
CH_4	0.0000	0.0000	0.0000	0.0000	0.0000	0.0000	0.0000	0.0000	0.0000	0.0000	0.0000
C_2H_6	0.0000	0.0000	0.0000	0.0000	0.0000	0.0000	0.0000	0.0000	0.0000	0.0000	0.0000
C_3H_8	0.0000	0.0000	0.0000	0.0000	0.0000	0.0000	0.0000	0.0000	0.0000	0.0000	0.0000
n-C_4H_{10}	0.0000	0.0000	0.0000	0.0000	0.0000	0.0000	0.0000	0.0000	0.0000	0.0000	0.0000
n-C_5H_{12}	0.0000	0.0000	0.0000	0.0000	0.0000	0.0000	0.0000	0.0000	0.0000	0.0000	0.0000
n-C_6H_{14}	0.0000	0.0000	0.0000	0.0000	0.0000	0.0000	0.0000	0.0000	0.0000	0.0000	0.0000
N_2	0.0002	0.0002	0.0002	0.0002	0.0002	0.0003	0.0003	0.0000	0.0000	0.0000	0.0000
O_2	0.0000	0.0000	0.0000	0.0000	0.0000	0.0000	0.0000	0.0000	0.0000	0.0000	0.0000
H_2O	0.2302	0.2302	0.2302	0.2302	0.2302	0.0049	0.0043	0.8743	0.8743	0.8743	0.0488
CO_2	0.0605	0.0605	0.0605	0.0605	0.0605	1.0000	0.0062	0.0430	0.0430	0.0430	0.9266
CO	0.0000	0.0000	0.0000	0.0000	0.0000	0.2973	0.3209	0.0000	0.0000	0.0000	0.0074
MEA	0.0000	0.0000	0.0000	0.0000	0.0000	0.0781	0.0000	0.0824	0.0824	0.0824	0.0000
H_2	0.4791	0.4791	0.4791	0.4791	0.4791	0.6194	0.6683	0.0002	0.0002	0.0002	0.0171
C	0.0000	0.0000	0.0000	0.0000	0.0000	0.0000	0.0000	0.0000	0.0000	0.0000	0.0000

Continued…

Table D.2. Process stream summary table (RWGS unit)

Stream Number	32	33	34	35	36	37	38	39	40	41	42
Vapour Fraction	0	0	0	0	0	1	0.9793	1	1	0.9829	1
Temperature (°C)	113	80.49	80.49	80.99	50	149.1	51.30	51.30	158.4	51.30	51.30
Pressure (kPa)	210	177.6	177.6	3035	3015	510.1	480.7	480.7	1301	1287	1287
Molar Flow (kmol/h)	224500	224500	224600	224600	224600	3159	3159	3094	3094	3094	3041
Mole Fraction											
CH_4	0.0000	0.0000	0.0000	0.0000	0.0000	0.0000	0.0000	0.0000	0.0000	0.0000	0.0000
C_2H_6	0.0000	0.0000	0.0000	0.0000	0.0000	0.0000	0.0000	0.0000	0.0000	0.0000	0.0000
C_3H_8	0.0000	0.0000	0.0000	0.0000	0.0000	0.0000	0.0000	0.0000	0.0000	0.0000	0.0000
n-C_4H_{10}	0.0000	0.0000	0.0000	0.0000	0.0000	0.0000	0.0000	0.0000	0.0000	0.0000	0.0000
n-C_5H_{12}	0.0000	0.0000	0.0000	0.0000	0.0000	0.0000	0.0000	0.0000	0.0000	0.0000	0.0000
n-C_6H_{14}	0.0000	0.0000	0.0000	0.0000	0.0000	0.0000	0.0000	0.0000	0.0000	0.0000	0.0000
N_2	0.0000	0.0000	0.0000	0.0000	0.0000	0.0000	0.0000	0.0000	0.0000	0.0000	0.0000
O_2	0.0000	0.0000	0.0000	0.0000	0.0000	0.0000	0.0000	0.0000	0.0000	0.0000	0.0000
H_2O	0.8859	0.8859	0.8860	0.8860	0.8860	0.0488	0.0488	0.0288	0.0288	0.0288	0.0119
CO_2	0.0305	0.0305	0.0305	0.0305	0.0305	0.9266	0.9266	0.9461	0.9461	0.9461	0.9625
CO	0.0000	0.0000	0.0000	0.0000	0.0000	0.0074	0.0074	0.0076	0.0076	0.0076	0.0077
MEA	0.0836	0.0836	0.0835	0.0835	0.0835	0.0000	0.0000	0.0000	0.0000	0.0000	0.0000
H_2	0.0000	0.0000	0.0000	0.0000	0.0000	0.0171	0.0171	0.0175	0.0175	0.0175	0.0178
C	0.0000	0.0000	0.0000	0.0000	0.0000	0.0000	0.0000	0.0000	0.0000	0.0000	0.0000

Continued…

Table D.2. Process stream summary table (RWGS unit)

Stream Number	43	44	45	46	W-makeup	MEA-makeup
Vapour Fraction	1	1	1	1	0	0
Temperature (°C)	155.6	137	200	200	80.49	80.49
Pressure (kPa)	3319	2994	2973	2500	177.6	177.6
Molar Flow (kmol/h)	3041	37420	37420	37420	115.9	0.0452
Mole Fraction						
CH_4	0.0000	0.0000	0.0000	0.0000	0.0000	0.0000
C_2H_6	0.0000	0.0000	0.0000	0.0000	0.0000	0.0000
C_3H_8	0.0000	0.0000	0.0000	0.0000	0.0000	0.0000
n-C_4H_{10}	0.0000	0.0000	0.0000	0.0000	0.0000	0.0000
n-C_5H_{12}	0.0000	0.0000	0.0000	0.0000	0.0000	0.0000
n-C_6H_{14}	0.0000	0.0000	0.0000	0.0000	0.0000	0.0000
N_2	0.0000	0.0003	0.0003	0.0003	0.0000	0.0000
O_2	0.0000	0.0000	0.0000	0.0000	0.0000	0.0000
H_2O	0.0119	0.0043	0.0043	0.0043	1.0000	0.0000
CO_2	0.9625	0.0062	0.0062	0.0062	0.0000	0.0000
CO	0.0077	0.3209	0.3209	0.3209	0.0000	0.0000
MEA	0.0000	0.0000	0.0000	0.0000	0.0000	1.0000
H_2	0.0178	0.6683	0.6683	0.6683	0.0000	0.0000
C	0.0000	0.0000	0.0000	0.0000	0.0000	0.0000

Table D.3. Process stream summary table (FT unit)

Stream Number	47	48	49(a)	49(b)	50	51	52(a)	52(b)	53	54	55(a)	55(b)
Vapour Fraction	1	0.998	1	1	0.9999	0.9280	1	1	0.970	0.9954	1	0
Temperature (oC)	199.69	203.22	203.22	203.22	176.1	40	40	40	17.48	5	5	5
Pressure (kPa)	2500	2222	2222	2222	2205	2163	2163	2163	2135	2095	2095	2095
Molar Flow (kmol/h)	186200	162700	162500	203.8	162500	162500	150800	269	150800	150800	150100	174.3
Mole Fraction												
CO	0.1755	0.1284	0.1285	0.0097	0.1285	0.1285	0.1385	0.0063	0.1385	0.1385	0.1391	0.0059
H_2	0.3515	0.2502	0.2504	0.0145	0.2504	0.2504	0.2699	0.0053	0.2699	0.2699	0.2711	0.0042
CH_4	0.3006	0.3476	0.3480	0.0348	0.3480	0.3480	0.3749	0.0362	0.3749	0.3749	0.3766	0.0453
C_2H_6	0.0164	0.0190	0.0190	0.0033	0.0190	0.0190	0.0205	0.0086	0.0205	0.0205	0.0205	0.0158
C_3H_8	0.0106	0.0123	0.0123	0.0034	0.0123	0.0123	0.0132	0.0170	0.0132	0.0132	0.0133	0.0400
C_4H_{10}	0.0049	0.0058	0.0058	0.0025	0.0058	0.0058	0.0062	0.0245	0.0062	0.0062	0.0062	0.0724
C_5H_{12}	0.0017	0.0021	0.0021	0.0014	0.0021	0.0021	0.0022	0.0261	0.0022	0.0022	0.0021	0.0917
C_6H_{14}	0.0005	0.0007	0.0007	0.0008	0.0007	0.0007	0.0007	0.0250	0.0007	0.0007	0.0006	0.0948
C_7H_{16}	0.0001	0.0003	0.0003	0.0005	0.0003	0.0003	0.0003	0.0259	0.0003	0.0003	0.0002	0.0871
C_8H_{18}	0.0000	0.0002	0.0002	0.0004	0.0002	0.0002	0.0001	0.0323	0.0001	0.0001	0.0000	0.0693
C_9H_{20}	0.0000	0.0001	0.0001	0.0005	0.0001	0.0001	0.0001	0.0431	0.0001	0.0001	0.0000	0.0450
$C_{10}H_{22}$	0.0000	0.0001	0.0001	0.0007	0.0001	0.0001	0.0000	0.0527	0.0000	0.0000	0.0000	0.0228
C_2H_4	0.0019	0.0022	0.0022	0.0003	0.0022	0.0022	0.0024	0.0007	0.0024	0.0024	0.0024	0.0012
C_3H_6	0.0167	0.0194	0.0194	0.0049	0.0194	0.0194	0.0209	0.0227	0.0209	0.0209	0.0209	0.0529
C_4H_8	0.0062	0.0073	0.0073	0.0029	0.0073	0.0073	0.0079	0.0259	0.0079	0.0079	0.0078	0.0752
C_5H_{10}	0.0017	0.0021	0.0021	0.0014	0.0021	0.0021	0.0023	0.0217	0.0023	0.0023	0.0022	0.0746
C_6H_{12}	0.0004	0.0006	0.0006	0.0006	0.0006	0.0006	0.0006	0.0157	0.0006	0.0006	0.0005	0.0601
C_7H_{14}	0.0001	0.0002	0.0002	0.0002	0.0002	0.0002	0.0001	0.0124	0.0001	0.0001	0.0001	0.0426
C_8H_{16}	0.0000	0.0001	0.0001	0.0002	0.0001	0.0001	0.0001	0.0111	0.0001	0.0001	0.0000	0.0268
C_9H_{18}	0.0000	0.0000	0.0000	0.0001	0.0000	0.0000	0.0000	0.0114	0.0000	0.0000	0.0000	0.0134
$C_{10}H_{20}$	0.0000	0.0000	0.0000	0.0001	0.0000	0.0000	0.0000	0.0109	0.0000	0.0000	0.0000	0.0052
$C_{13}H_{28}$	0.0000	0.0005	0.0005	0.0118	0.0005	0.0005	0.0000	0.2997	0.0000	0.0000	0.0000	0.0071
$C_{18}H_{38}$	0.0000	0.0004	0.0003	0.0593	0.0003	0.0003	0.0000	0.1738	0.0000	0.0000	0.0000	0.0001
$C_{23}H_{48}$	0.0000	0.0003	0.0001	0.1471	0.0001	0.0001	0.0000	0.0513	0.0000	0.0000	0.0000	0.0000

$C_{28}H_{58}$	0.0000	0.0002	0.0000	0.1538	0.0000	0.0000	0.0000	0.0066	0.0000	0.0000	0.0000	0.0000
$C_{33}H_{68}$	0.0000	0.0002	0.0000	0.1233	0.0000	0.0000	0.0000	0.0001	0.0000	0.0000	0.0000	0.0000
$C_{38}H_{78}$	0.0000	0.0001	0.0000	0.0933	0.0000	0.0000	0.0000	0.0005	0.0000	0.0000	0.0000	0.0000
$C_{65}H_{132}$	0.0000	0.0004	0.0000	0.2998	0.0000	0.0000	0.0000	0.0000	0.0000	0.0000	0.0000	0.0000
H_2O	0.0013	0.0738	0.0739	0.0109	0.0739	0.0739	0.0039	0.0010	0.0039	0.0039	0.0005	0.0002
CO_2	0.1041	0.1190	0.1192	0.0168	0.1192	0.1192	0.1283	0.0315	0.1283	0.1283	0.1288	0.0462
O_2	0.0000	0.0000	0.0000	0.0000	0.0000	0.0000	0.0000	0.0000	0.0000	0.0000	0.0000	0.0000
N_2	0.0056	0.0064	0.0064	0.0005	0.0064	0.0064	0.0069	0.0003	0.0069	0.0069	0.0069	0.0002

Continued…

Table D.3. Process stream summary table (FT unit)

Stream Number	56	57	58	59	60	61	A-1	A-2	A-3	A-1	Syn-1	Syn-2
Vapour Fraction	1	1	1	1	1	1	1	1	1	1	0.0596	0
Temperature (oC)	5	25.95	33.06	108.18	163.36	200	25	137	195	25	148.9	40
	2095	265	2599.33	2556.85	2545.39	2545	101.3	81.47	120	101.3	2095	2092
Pressure (kPa)		1										
Molar Flow (kmol/h)	148600	148600	148600	148600	148600	148600	57490	57490	57490	57490	647.1	647.1
Mole Fraction												
CO	0.1391	0.1391	0.1391	0.1391	0.1391	0.1391	0.0000	0.0000	0.0000	0.0000	0.0073	0.0073
H_2	0.2711	0.2711	0.2711	0.2711	0.2711	0.2711	0.0000	0.0000	0.0000	0.0000	0.0079	0.0079
CH_4	0.3766	0.3766	0.3766	0.3766	0.3766	0.3766	0.0000	0.0000	0.0000	0.0000	0.0382	0.0382
C_2H_6	0.0205	0.0205	0.0205	0.0205	0.0205	0.0205	0.0000	0.0000	0.0000	0.0000	0.0088	0.0088
C_3H_8	0.0133	0.0133	0.0133	0.0133	0.0133	0.0133	0.0000	0.0000	0.0000	0.0000	0.0189	0.0189
C_4H_{10}	0.0062	0.0062	0.0062	0.0062	0.0062	0.0062	0.0000	0.0000	0.0000	0.0000	0.0305	0.0305
C_5H_{12}	0.0021	0.0021	0.0021	0.0021	0.0021	0.0021	0.0000	0.0000	0.0000	0.0000	0.0360	0.0360
C_6H_{14}	0.0006	0.0006	0.0006	0.0006	0.0006	0.0006	0.0000	0.0000	0.0000	0.0000	0.0362	0.0362
C_7H_{16}	0.0002	0.0002	0.0002	0.0002	0.0002	0.0002	0.0000	0.0000	0.0000	0.0000	0.0344	0.0344
C_8H_{18}	0.0000	0.0000	0.0000	0.0000	0.0000	0.0000	0.0000	0.0000	0.0000	0.0000	0.0323	0.0323
C_9H_{20}	0.0000	0.0000	0.0000	0.0000	0.0000	0.0000	0.0000	0.0000	0.0000	0.0000	0.0302	0.0302
$C_{10}H_{22}$	0.0000	0.0000	0.0000	0.0000	0.0000	0.0000	0.0000	0.0000	0.0000	0.0000	0.0283	0.0283
C_2H_4	0.0024	0.0024	0.0024	0.0024	0.0024	0.0024	0.0000	0.0000	0.0000	0.0000	0.0007	0.0007
C_3H_6	0.0209	0.0209	0.0209	0.0209	0.0209	0.0209	0.0000	0.0000	0.0000	0.0000	0.0252	0.0252
C_4H_8	0.0078	0.0078	0.0078	0.0078	0.0078	0.0078	0.0000	0.0000	0.0000	0.0000	0.0319	0.0319
C_5H_{10}	0.0022	0.0022	0.0022	0.0022	0.0022	0.0022	0.0000	0.0000	0.0000	0.0000	0.0296	0.0296
C_6H_{12}	0.0005	0.0005	0.0005	0.0005	0.0005	0.0005	0.0000	0.0000	0.0000	0.0000	0.0229	0.0229
C_7H_{14}	0.0001	0.0001	0.0001	0.0001	0.0001	0.0001	0.0000	0.0000	0.0000	0.0000	0.0167	0.0167
C_8H_{16}	0.0000	0.0000	0.0000	0.0000	0.0000	0.0000	0.0000	0.0000	0.0000	0.0000	0.0119	0.0119
C_9H_{18}	0.0000	0.0000	0.0000	0.0000	0.0000	0.0000	0.0000	0.0000	0.0000	0.0000	0.0084	0.0084
$C_{10}H_{20}$	0.0000	0.0000	0.0000	0.0000	0.0000	0.0000	0.0000	0.0000	0.0000	0.0000	0.0060	0.0060

$C_{13}H_{28}$	0.0000	0.0000	0.0000	0.0000	0.0000	0.0000	0.0000	0.0000	0.0000	0.0000	0.1302	0.1302
$C_{18}H_{38}$	0.0000	0.0000	0.0000	0.0000	0.0000	0.0000	0.0000	0.0000	0.0000	0.0000	0.0909	0.0909
$C_{23}H_{48}$	0.0000	0.0000	0.0000	0.0000	0.0000	0.0000	0.0000	0.0000	0.0000	0.0000	0.0677	0.0677
$C_{28}H_{58}$	0.0000	0.0000	0.0000	0.0000	0.0000	0.0000	0.0000	0.0000	0.0000	0.0000	0.0512	0.0512
$C_{33}H_{68}$	0.0000	0.0000	0.0000	0.0000	0.0000	0.0000	0.0000	0.0000	0.0000	0.0000	0.0389	0.0389
$C_{38}H_{78}$	0.0000	0.0000	0.0000	0.0000	0.0000	0.0000	0.0000	0.0000	0.0000	0.0000	0.0296	0.0296
$C_{65}H_{132}$	0.0000	0.0000	0.0000	0.0000	0.0000	0.0000	0.0000	0.0000	0.0000	0.0000	0.0944	0.0944
H_2O	0.0005	0.0005	0.0005	0.0005	0.0005	0.0005	0.0000	0.0000	0.0000	0.0000	0.0039	0.0039
CO_2	0.1288	0.1288	0.1288	0.1288	0.1288	0.1288	0.0000	0.0000	0.0000	0.0000	0.0308	0.0308
O_2	0.0000	0.0000	0.0000	0.0000	0.0000	0.0000	0.2100	0.2100	0.2100	0.2100	0.0000	0.0000
N_2	0.0069	0.0069	0.0069	0.0069	0.0069	0.0069	0.7900	0.0000	0.0000	0.7900	0.0003	0.0003

Table D.4. Solid carbon summary table

Stream Number	SC-1	SC-2	SC-3	SC-4	SC-5	SC-6
Vapour Fraction	0	0	0	0	0	0
Temperature (ºC)	1100	639.3	472.2	470.6	86	40
Pressure (kPa)	1844	1844	1844	1844	1844	1844
Molar Flow (kmol/h)	21220	21220	21220	21220	21220	21220
Mole Fraction						
Carbon (C)	1.000	1.000	1.000	1.000	1.000	1.000

Table D.5. Purge gas and flue gas summary table

Stream Number	P-1	P-2	P-3	P-4	P-5	P-4	Fg-1	Fg-2	Fg-3	Fg-4	Fg-5
Vapour Fraction	1	1	1	1	1	1	1	1	1	1	1
Temperature (oC)	39.36	58.12	5	-3.99	47.41	-3.99	772.4	674.2	626.8	251.5	150
Pressure (kPa)	100	120	2095	120	120	120	120	120	120	120	120
Molar Flow (kmol/h)	7615	7615	1501	1501	9119	1501	64990	64990	64990	64990	64990
Mole Fraction											
CO	0.0000	0.0000	0.1391	0.1391	0.0229	0.1391	0.0000	0.0000	0.0000	0.0000	0.0000
H_2	0.3673	0.3673	0.2711	0.2711	0.3514	0.2711	0.0000	0.0000	0.0000	0.0000	0.0000
CH_4	0.5490	0.5490	0.3766	0.3766	0.5206	0.3766	0.0000	0.0000	0.0000	0.0000	0.0000
C_2H_6	0.0000	0.0000	0.0205	0.0205	0.0034	0.0205	0.0000	0.0000	0.0000	0.0000	0.0000
C_3H_8	0.0000	0.0000	0.0133	0.0133	0.0022	0.0133	0.0000	0.0000	0.0000	0.0000	0.0000
C_4H_{10}	0.0000	0.0000	0.0062	0.0062	0.0010	0.0062	0.0000	0.0000	0.0000	0.0000	0.0000
C_5H_{12}	0.0000	0.0000	0.0021	0.0021	0.0004	0.0021	0.0000	0.0000	0.0000	0.0000	0.0000
C_6H_{14}	0.0000	0.0000	0.0006	0.0006	0.0001	0.0006	0.0000	0.0000	0.0000	0.0000	0.0000
C_7H_{16}	0.0000	0.0000	0.0002	0.0002	0.0000	0.0002	0.0000	0.0000	0.0000	0.0000	0.0000
C_8H_{18}	0.0000	0.0000	0.0000	0.0000	0.0000	0.0000	0.0000	0.0000	0.0000	0.0000	0.0000
C_9H_{20}	0.0000	0.0000	0.0000	0.0000	0.0000	0.0000	0.0000	0.0000	0.0000	0.0000	0.0000
$C_{10}H_{22}$	0.0000	0.0000	0.0000	0.0000	0.0000	0.0000	0.0000	0.0000	0.0000	0.0000	0.0000
C_2H_4	0.0000	0.0000	0.0024	0.0024	0.0004	0.0024	0.0000	0.0000	0.0000	0.0000	0.0000
C_3H_6	0.0000	0.0000	0.0209	0.0209	0.0034	0.0209	0.0000	0.0000	0.0000	0.0000	0.0000
C_4H_8	0.0000	0.0000	0.0078	0.0078	0.0013	0.0078	0.0000	0.0000	0.0000	0.0000	0.0000
C_5H_{10}	0.0000	0.0000	0.0022	0.0022	0.0004	0.0022	0.0000	0.0000	0.0000	0.0000	0.0000
C_6H_{12}	0.0000	0.0000	0.0005	0.0005	0.0001	0.0005	0.0000	0.0000	0.0000	0.0000	0.0000
C_7H_{14}	0.0000	0.0000	0.0001	0.0001	0.0000	0.0001	0.0000	0.0000	0.0000	0.0000	0.0000
C_8H_{16}	0.0000	0.0000	0.0000	0.0000	0.0000	0.0000	0.0000	0.0000	0.0000	0.0000	0.0000
C_9H_{18}	0.0000	0.0000	0.0000	0.0000	0.0000	0.0000	0.0000	0.0000	0.0000	0.0000	0.0000
$C_{10}H_{20}$	0.0000	0.0000	0.0000	0.0000	0.0000	0.0000	0.0000	0.0000	0.0000	0.0000	0.0000
$C_{13}H_{28}$	0.0000	0.0000	0.0000	0.0000	0.0000	0.0000	0.0000	0.0000	0.0000	0.0000	0.0000
$C_{18}H_{38}$	0.0000	0.0000	0.0000	0.0000	0.0000	0.0000	0.0000	0.0000	0.0000	0.0000	0.0000
$C_{23}H_{48}$	0.0000	0.0000	0.0000	0.0000	0.0000	0.0000	0.0000	0.0000	0.0000	0.0000	0.0000

$C_{28}H_{58}$	0.0000	0.0000	0.0000	0.0000	0.0000	0.0000	0.0000	0.0000	0.0000	0.0000	0.0000
$C_{33}H_{68}$	0.0000	0.0000	0.0000	0.0000	0.0000	0.0000	0.0000	0.0000	0.0000	0.0000	0.0000
$C_{38}H_{78}$	0.0000	0.0000	0.0000	0.0000	0.0000	0.0000	0.0000	0.0000	0.0000	0.0000	0.0000
$C_{65}H_{132}$	0.0000	0.0000	0.0000	0.0000	0.0000	0.0000	0.0000	0.0000	0.0000	0.0000	0.0000
H_2O	0.0000	0.0000	0.0005	0.0005	0.0001	0.0005	0.2018	0.2018	0.2018	0.2018	0.2018
CO_2	0.0600	0.0600	0.1288	0.1288	0.0714	0.1288	0.0917	0.0917	0.0917	0.0917	0.0917
O_2	0.0000	0.0000	0.0000	0.0000	0.0000	0.0000	0.0048	0.0048	0.0048	0.0048	0.0048
N_2	0.0238	0.0238	0.0069	0.0069	0.0210	0.0069	0.7017	0.7017	0.7017	0.7017	0.7017

Table D.6 Steam and condensed steam summary table

Stream Number	S-1(a)	S-1(b)	S-1	S-2(a)	S-2(b)	S-2	S-3	S-4	S-5	S-6	S-7
Vapour Fraction	0	0	0	1	1	1	1	1	0.9110	0	0
Temperature (°C)	200	200	200	200	200	200	270	270	75.89	71.11	71.32
Pressure (kPa)	1555	1555	1555	1555	1555	1555	1555	1555	40	28.85	1555
Molar Flow (kmol/h)	34440	18620	53060	34440	18620	53060	34440	51800	51800	51800	51800
Mole Fraction											
H_2O	1.0000	1.0000	1.0000	1.0000	1.0000	1.0000	1.0000	1.0000	1.0000	1.0000	1.0000

Continued…

Table D.6 Steam and condensed steam summary table

Stream Number	S-8	S-9	S-10	S-11
Vapour Fraction	0	0	0	1
Temperature (°C)	68.42	120.9	71.32	270
Pressure (kPa)	1555	1555	1555	1555
Molar Flow (kmol/h)	34440	34440	17350	17350
Mole Fraction				
H_2O	1.0000	1.0000	1.0000	1.0000

Table D.7. Cooling water summary table

Stream Number	CW-1	CW-1’	CW-2	CW-2’	CW-3	CW-3’	CW-4	CW-4’	CW-5	CW-5
Vapour Fraction	0	0	0	0	0	0	0	0	0	0
Temperature (°C)	30	40	30	40.0	30	40	30	40	30	40
Pressure (kPa)	200.0	173.1	200	192.5	200	186.7	200	190.1	200	187.7
Molar Flow (kmol/h)	163600	163600	20370	20370	21460	21460	588400	588400	755700	755700
Mole Fraction										
H_2O	1.000	1.000	1.000	1.000	1.000	1.000	1.000	1.000	1.000	1.000

Continued…

Table D.7. Cooling water summary table

Stream Number	CW-6	CW-6’	CW-7	CW-7’	CW-8	CW-8’	CW-9	CW-9’
Vapour Fraction	0	0	0	0	0	0	0	0
Temperature (°C)	30	40	30	40	30	40.0	30	40
Pressure (kPa)	200	192.2	200.0	188.8	200	162.9	200	165.5
Molar Flow (kmol/h)	107200	107200	1851000	1851000	2634000	2634000	12850	12850
Mole Fraction								
H_2O	1.000	1.000	1.000	1.000	1.000	1.000	1.000	1.000

Table D.8. Produced process water summary table

Stream Number	W-1	W-2	W-3	W-4	W-5
Vapour Fraction	0	0	0	0	0
Temperature (°C)	51.30	51.30	50.63	40	5
Pressure (kPa)	480.7	1287	3147	2163	2095
Molar Flow (kmol/h)	65.32	53.01	11850	11430	516.4
Mole Fraction					
H_2O	1.000	1.000	1.000	1.000	1.000

Appendix E: Equipment purchase and bare module cost (CAPCOST)

Table E.1. Equipment purchase and bare module cost details

Compressors	Type	Power (kW)	# Spares	MOC [a]	CP [b]	C_{BM} [c]	CP^{o} [d]	C_{BM}^{o} [e]
C-1	Centrifugal	1570	0	SS	$20400000	$55900000	$9730000	$26700000
C-2	Centrifugal	1340	0	SS	$1110000	$3050000	$530000	$1450000
C-3	Centrifugal	3390	0	SS	$2630000	$7200000	$1250000	$3430000
C-4	Centrifugal	3610	0	SS	$2740000	$7510000	$1310000	$3580000
C-5	Centrifugal	3330	0	SS	$2600000	$7110000	$1240000	$3390000
C-6	Centrifugal	29300	0	SS	$19000000	$52000000	$9040000	$24800000
C-7	Centrifugal	27800	0	CS	$8740000	$23900000	$8740000	$23900000

Continued…

Drives	Type	Power (kW)	# Spares	CP	C_{BM}	CP^o	C^o_{BM}
D-1	Electric - Explosion Proof	32165	0	$3200000	$4790000	$3200000	$4790000
D-2	Electric - Explosion Proof	1382	0	$213000	$320000	$213000	$320000
D-3	Electric - Explosion Proof	3495	0	$455000	$682000	$455000	$682000
D-4	Electric - Explosion Proof	3722	0	$462000	$693000	$462000	$693000
D-5	Electric - Explosion Proof	3433	0	$452000	$679000	$452000	$679000
D-6	Electric - Explosion Proof	30206	0	$2960000	$4440000	2960000	$4440000
D-7	Electric - Explosion Proof	28660	0	$2930000	$4390000	$2930000	$4390000
D-P-1	Electric - Explosion Proof	5289	0	$683000	$1020000	$683000	$1020000
D-P-2	Electric - Explosion Proof	509	0	$148000	$222000	$148000	$222000

Continued…

Exchangers	Exchanger Type	Shell P (barg)	Tube P (barg)	MOC Tube/Shell	Area (m^2)	CP	C_{BM}	CP^o	C^o_{BM}
E-1	Floating Head	20.4	18.3	SS/CS	1520	$316000	$1580000	$324000	$533000
E-2	Floating Head	18.2	17.4	Nickel/Nickel	2320	$652000	$4050000	$493000	$541000
E-3	Floating Head	25	17.3	SS/SS	2810	$601000	$3980000	$601000	$659000
E-4	Floating Head	1	32.9	SS/CS	1020	$210000	$1060000	$223000	$367000
E-5	Floating Head	32.6	20.6	SS/SS	2190	$483000	$3160000	$467000	$512000
E-6	Floating Head	1	4.1	SS/CS	170	$91400	$234000	$50500	$166000
E-7	Floating Head	1	12	SS/CS	176	$94500	$241000	$51500	$170000
E-8	Floating Head	31.4	32.2	Nickel/Nickel	6550	$847000	$12100000	$1400000	$658000
E-9	Floating Head	24.6	31.2	SS/SS	4570	$601000	$6580000	$975000	$641000
E-11	Floating Head	29	31.1	SS/SS	1033	$348000	$1530000	$226000	$372000
E-12	Floating Head	1	30.8	SS/CS	2300	$307000	$2330000	$490000	$537000
E-16	Floating Head	2.1	31	SS/SS	13700	$595000	$18600000	$2940000	$691000
E-17	Floating Head	1	29.4	SS/CS	6300	$361000	$6380000	$1350000	$632000
E-18	Floating Head	0.013	21.2	SS/CS	3950	$393000	$3990000	$846000	$696000
E-19	Floating Head	1	21.1	SS/CS	13300	$5270000	$13400000	$2830000	$9330000
E-20	Floating Head	25.5	20	SS/SS	3574	$2290000	$5050000	$762000	$2510000
E-22	Floating Head	0.3	1	CS/CS	8080	$1720000	$5670000	$1720000	$5670000
E-27	Floating Head	1	1	SS/CS	230	$110000	$282000	$60800	$200000
E-28	Kettle Boiler	1.1	14.6	CS/CS	1400	$2130000	$6960000	$2100000	$6900000
FT-tubes (14 FT reactors)	Floating Head	14.5	24	SS/CS	10700	$4550000×14	$11300000×14	$2300000×14	$7560000×14

Continued…

Heater	Type	Duty (MJ/h)	MOC	CP	C_{BM}	CP^o	C_{BM}^o
RWGS	Reformer	715000	Alloy steel	$21600000	$57800000	$17200000	$46100000
MDR	Pyrolysis	345000	Alloy steel	$113880000	$242400000	$96600000	$206400000

Pump	Type	Power (kW)	# Spares	MOC	Discharge P (barg)	CP	C_{BM}	CP^o	C_{BM}^o
P-1	Centrifugal	494	0	CS	14.6	$68800	$331000	$76600	$124000
P-2	Centrifugal	5130	0	CS	29.4	$101200	$3920000	$773000	$139000

Towers	Trays	Height (m)	Diameter (m)	MOC	P (barg)	CP	C_{BM}	CP^o	C_{BM}^o
T-1 (5 columns)	22 SS-Valve	22	3.16	SS	31	$5800000×5	$10400000×5	$536000×5	$1050000×5
T-2 (5 columns)	10 SS-Valve	10	3.24	SS	1.1	$799000×5	$1210000×5	$263000×5	$528000×5

Turbines	Type	Power (kW)	# Spares	MOC	CP	C_{BM}	CP^o	C_{BM}^o
Ex-1	Axial	3400	4	CS	$2870000	$10040000	$2870000	$10040000
Ex-2	Axial	4000	32	CS	$19500000	$68300000	$19500000	$68300000

Continued…

Vessels	Orientation	Height (meters)	Diameter (meters)	MOC	P (barg)	CP	C_{BM}	CP^o	C_{BM}^o
V-1 (1 vessel)	Vertical	4.14	1.38	SS	3.81	$39600×1	$100800×1	$12700×1	$51900×1
V-2 (1 vessel)	Vertical	3.2	1.07	SS	11.9	$42800×1	$96100×1	$8120×1	$33100×1
V-3 (1 vessel)	Vertical	7.03	2.35	SS	30.5	$872000×1	$1670000×1	$38300×1	$156000×1
V-4 (5 vessels)	Vertical	9.1	3.03	SS	21.2	$1460000×5	$2830000×5	$71300×5	$290000×5
V-5 (7 vessels)	Horizontal	9.92	3.31	SS	20.6	$1390000×7	$2210000×7	$64100×7	$193000×7
V-6 (7 vessels)	Horizontal	9.85	3.28	SS	20	$1320000×7	$2100000×7	$63200×7	$190000×7
FT-shell (14 shells)	Vertical	10.1	6.07	CS	14.5	$2430000×14	$5050000×14	$276000×14	$1120000×14

User defined	Description	CP	C_{BM}
1	RWGS initial catalyst fill	$125100	$125100
2	FT initial catalyst fill	$48875185	$48875185
3	Solid carbon HEX (Solex)	$4587530	$4587530
4	PSA	$60029540	$60029540
5	Bi cost	$33817360	$33817360
6	Cu cost	$7116430	$7116430

[a] MOC: Material of construction, [b] CP: Purchased equipment cost, [c] CBM: Bare module cost, [d] CP^o: Purchased equipment cost at base condition, [e] C_{BM}^o: Bare module cost at base condition

Appendix F: Shell-and-tube heat exchanger design and rating (EDR) summary tables

Table F.1. Specifications of the shell-and-tube heat exchangers

	Heat Exchanger							
	E-1	E-2	E-3	E-4	E-5	E-6	E-7	E-8
TEMA type	BXM	BEM	BEM	BEM	BEM	BEM	BEM	BEM
Tube OD (in)	0.63	0.76	0.6	0.6	1.08	0.73	0.63	0.59
Shell ID (in)	35	45	52	31	43.5	22	20	56.8
Tube length (in)	198	265	265	185	227.5	154	148	323
Baffle spacing (in)	-	31	32	32	32	20	21	25
Tube passes	1	1	1	1	1	1	1	1
Number of tubes/shell	1205	1135	1459	908	880	374	466	1884
Shell passes	1	1	1	1	1	1	1	1
Shells in series	1	1	1	1	1	1	1	1
Shells in parallel	5	5	6	5	5	2	2	9
Shell pressure drop (kPa)	39.68	21.34	42.48	20.94	21.17	7.51	13.3	19.42
Tube pressure drop (kPa)	6.96	11.43	8.14	8.75	28.46	29.47	14.63	15.85
Total heat exchanged (MW)	21.17	315.5	121.3	34.05	40.96	4.236	4.538	372.2
Overall U (dirty) ($W\ m^{-2}\ K^{-1}$)	311	475.3	492.2	915.5	565.3	561.9	533.4	418.7
Effective Surface (m^2) (including all shells)	1522.32	2314.9	2812.30	1018.20	2187.50	170	176	6552.1

Continued…

	Heat Exchanger							
	E-9	E-11	E-12	E-16	E-17	E-18	E-19	E-20
TEMA type	BXM	BIM	BXM	BEM	BXM	BXM	BXM	BIM
Tube OD (in)	0.78	0.75	0.68	0.51	0.75	1.38	0.51	0.75
Shell ID (in)	58	36	46.5	67	53	60.5	65	45
Tube length (in)	325	190	301	350	310	320	325	260
Baffle spacing (in)	-	30	-	30	-	-	-	-
Tube passes	1	1	1	1	1	1	1	1
Number of tubes/shell	2224	897	1846	7565	2684	735	6557	1512
Shell passes	1	1	1	1	1	1	1	1
Shells in series	1	1	1	1	2	1	1	1
Shells in parallel	4	4	3	5	5	6	6	6
Shell pressure drop (kPa)	11.46	5.96	9.92	32.43	12.32	19.83	11.16	51.67
Tube pressure drop (kPa)	9.97	36.87	28.59	5.88	20.14	17.22	41.55	3.24
Total heat exchanged (MW)	92.2	26.64	130.5	166.5	158.2	52.38	389.5	12.06
Overall U (dirty) ($W\ m^{-2}\ K^{-1}$)	458	624.4	952.3	682.7	888.8	136.6	683.5	69.5
Effective Surface (m^2) (including all shells)	4565.69	1033.1	2300	13726.3	6304.2	3950.56	13257	3574.3

Continued…

	Heat Exchanger		
	E-22	E-27 (MEA condenser)	E-28 (MEA reboiler)
TEMA type	BXM	BIM	BKM
Tube OD (in)	1.12	0.63	0.98
Shell ID (in)	60	28	40
Tube length (in)	320	177	200
Baffle spacing (in)	-	21	-
Tube passes	1	1	2
Number of tubes/shell	1239	509	882
Shell passes	1	1	1
Shells in series	1	1	1
Shells in parallel	9	2	4
Shell pressure drop (kPa)	7.30	9.5	20.67
Tube pressure drop (kPa)	27.69	7.77	14.21
Total heat exchanged (MW)	552.73	23.1	177.2
Overall U (dirty) ($W\ m^{-2}\ K^{-1}$)	1866	1366.1	1468.4
Effective Surface (m^2) (including all shells)	8082.50	229.93	1401.3